Kapteyn Institute

RuG

Rijksuniversiteit Groningen
Department of Astronomy

University of Groningen
MSc. Research Project

August 26, 2016

Radial variations of the initial mass function and other stellar population parameters within early-type galaxies

Author:
Gerjon Mensinga

Supervisors:
Prof. Dr. Scott C. Trager
Dr. Chiara Spiniello

Abstract

We investigate the radial behaviour of the low-mass slope of the Initial Mass Function (IMF) and other stellar population parameters (metallicity, α-abundance, stellar age, and sodium abundance) in 17 Early-Type Galaxies (ETGs) provided by the CALIFA survey. For each system we construct four elliptical annuli with different apertures and distance from the centre, to determine radial gradients. The stellar population parameters are extracted by comparing several Lick/IDS indices with single stellar population models using χ^2 statistics. Our main results are: 1) an IMF-σ relation and relations with σ in general are only loosely present or absent in our data. This is in disagreement with previously published results, most likely because we use spatially-resolved data and the σ relations are all reported in unresolved data; 2) a tight relation exists between IMF and metallicity, where to a higher metallicity corresponds a larger dwarf-to-giant ratio; 3) a tight relation exists between the gradients of the IMF and metallicity. The metallicity gradient is influenced by the merging history of ETGs, where shallower metallicity gradients imply a history of major merging events. The IMF slope is equally dependent on the merging history; 4) steep IMF slopes in the centres coincide with young stellar populations in the centre. These results fit in a two-phase IMF scenario. During the first star-forming phase a top-heavy IMF produces giant stars which die quickly and inject the interstellar medium with metals. The rise in metallicity causes later star-formation events to follow a more bottom-heavy IMF. Furthermore, we determine the mean radial trends of the stellar population parameters for the galaxies in our sample. We find that a) galaxies are more bottom-heavy in the centre and shallows to sub-Salpeter at 1 R_{eff}, b) the metallicity declines radially with an average of -0.21 dex, and c) galaxies with young centres grow radially older whereas galaxies with old centres show no radial age gradients. We conclude that the IMF varies within ETGs and depends mainly on metallicity and the merging history of the system. Metallicity might be a promising new parameter by which we can infer the IMF of a galaxy.

Contents

1

Introduction

In this thesis we study the amount and distribution of low-mass stars in galaxies. Specifically we try to find a relation between the lower mass-end slope of the Initial Mass Function (IMF) in Early-Type Galaxies (ETGs) and other stellar population parameters (being metallicity, α-abundance, stellar age, and sodium abundance) and aim to find what physical processes cause these relations. The IMF is a function that describes a distribution of stellar masses that form in one star-formation event in a given volume of space. Since most of the stellar evolutionary path is decided by its mass, all the observable properties of a galaxy which depend on stars (e.g. magnitude, luminosity, metallicity, etc.) are highly influenced by the IMF.

To give the reader a better understanding of the subject, we provide within this chapter a short overview on the formation of early-type galaxies, describe their basic properties and formation histories, provide a short description of the IMF, and show some methods used to study stellar populations within galaxies. We conclude by describing recent developments in this field and give an outline of this thesis.

1.1 Early-Type Galaxies

Early-type galaxies comprise elliptical (E) and lenticular (S0) galaxies. They are called 'early-type' because they sit on the left side of the Hubble sequence, which for many years has been interpreted as an evolution diagram. The Hubble sequence is shown in Figure 1.1. These galaxies differ morphologically from the 'late-type' spiral galaxies which are present on the right side of the sequence. Elliptical galaxies contain little dust and consist primarily of old and red stellar populations (e.g. Clemens et al. 2006). They are generally more massive than spirals and, in fact, more than half of the total stellar mass in the universe resides in ETGs (Gallazzi et al., 2008).

One characteristic of ETGs is that they have a smooth brightness profile which falls off with radius and can be described by a de Vaucouleurs brightness profile, or, more general, a Sérsic Law (de Vaucouleurs, 1948; Sérsic, 1963), which is given by

$$I(R) = I_{\rm eff} \times \exp\left(-b(n)[(R/R_{\rm eff})^{1/n} - 1]\right) \tag{1.1}$$

Here $R_{\rm eff}$ is the effective radius, which is the radius of the isophote in which half the total galaxy-luminosity is contained, and $I_{\rm eff}$ is the intensity at that radius. $b(n)$ is a polynomial that has been numerically determined to be $b(n) = 2.0n - 0.33$ (Ciotti & Bertin, 1999). n is a free parameter (for n

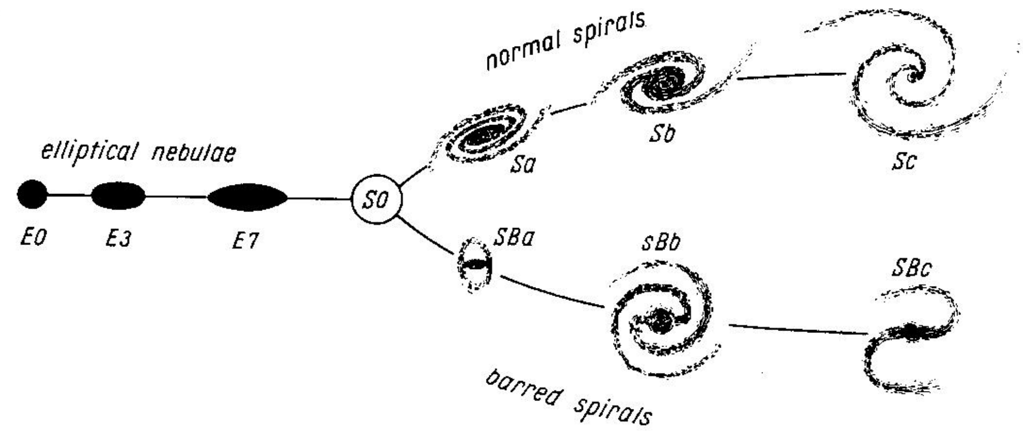

Figure 1.1: Visualization of the Hubble sequence (Hubble, 1936). On the left side are the early-type galaxies, which are elliptical (E) in shape. On the right are the late-type spiral galaxies. Late-types are divided into the classes regular spiral (S) and barred spiral (SB). The lenticular galaxies (S0) were assumed to be an evolutionary transition between the elliptical and spiral galaxies. The number added to the E-types defines the ellipticity of the galaxy, whereas the small letter added to the spirals defines how tightly wound the galaxy is.

= 4 the Sérsic law reduces to a de Vaucouleurs brightness profile).

A striking feature of ETGs is that many observable parameters hold a tight relation with the stellar velocity dispersion (σ) of the galaxy. Faber & Jackson (1976) found two relations for elliptical galaxies, including the luminosity-σ relation: $L \propto \sigma^4$. They concluded from the Virial Theorem that, if a galaxy is in virial equilibrium, σ correlates with the total mass (M) of the galaxy as:

$$\sigma^2 \propto \frac{GM}{R} \tag{1.2}$$

where R is the distance from the galactic centre and G is the gravitational constant.

Dressler et al. (1987) and Djorgovski & Davis (1987) proposed that elliptical galaxies inhabit a Fundamental Plane (FP). The FP provides a relation between the effective radius, the surface brightness, and the velocity dispersion. The FP relation allows us to estimate any of these three parameters $\{\log I_{\text{eff}}, \log R_{\text{eff}}, \log\sigma\}$ based on the values of the other two. The FP relation is

$$R_{\text{eff}} \propto \sigma_c^a \langle I_{\text{eff}} \rangle^b \tag{1.3}$$

where the set [a, b] are the fundamental plane parameters and σ_c is the central velocity dispersion.

Using the relation between luminosity, the mean surface brightness, and effective radius $L = 2\pi\langle I_{\text{eff}}\rangle R_{\text{eff}}^2$ we can define the mass-to-light ratio (Υ) of ETGs:

$$\Upsilon = \frac{M}{2\pi\langle I_{\text{eff}}\rangle R_{\text{eff}}^2} \tag{1.4}$$

which results in a formula that estimates the total mass of a galaxy, given the integrated light over the complete wavelength range of the spectra: $M = 2\pi\langle I_{eff}\rangle R_{eff}^2 \Upsilon$. Combining this with Equation (1.3) we get

$$R_{\text{eff}} \propto \sigma_c^2 \langle I_{\text{eff}} \rangle^{-1} \tag{1.5}$$

giving us the fundamental plane parameters, for a virial system, as [a = 2, b = -1]. In reality observed values differ from their 'ideal' virial values. For example, Bender, Burstein & Faber (1992) reported [a=1.4, b=-0.85] for the elliptical galaxies in the Virgo cluster. Therefore it is often said that the FP of a galaxy is 'tilted' (Prugniel & Simien, 1996; Bernardi et al., 2003; Trujillo, Burkert & Bell, 2004).

The tilt in the FP is assumed to be due to the dependence of Υ (Equation 1.4) on the different FP parameters. In particular, tilts in the FP can be attributed to: (i) variation in the dynamical structure of ETGs, (ii) variations of the baryonic to dark matter ratio, (iii) variations of the IMF and its accompanied star formation history, and/or (iv) variations in the galaxy's stellar populations.

For a given IMF the stellar mass-to-light ratio Υ_* (which as opposed to Υ excludes other galaxy energy components like kinematics and dark matter) depends on age, metallicity, stellar population and wavelength (Worthey, 1994). There exist correlations between the velocity dispersion and metallicity at fixed age (Faber & Jackson, 1976; Dressler et al., 1987; Trager et al., 2000b) and the velocity dispersion and age (Bernardi et al., 2005; Nelan et al., 2005). From these, stellar population models predict that Υ_* depends luminosity and mass (given that mass correlates positively with σ), and therefore can cause a tilt of the FP which depends on the observed wavelength (Pahre, Djorgovski & de Carvalho, 1998). This dependence, however, is weak and not enough to fully explain the FP tilt (Bernardi et al., 2003). Bender, Burstein & Faber (1993) extended the search by linking dynamically hot galaxies in the FP to their age and metallicity of the stellar populations. They concluded that only the central velocity dispersion has a large influence in determining stellar populations, where size, luminosity, and mass have a relatively low effect.

1.2 Galaxy formation theories

Here we briefly review how galaxies (in particular ETGs) are assumed to form. The discussion on the formation history of galaxies was dominated by two different hypotheses for structure formation. The first proposed idea is the monolithic collapse, the assumption that galaxies form from one giant collapsing gas cloud from one single burst of star formation (Eggen, Lynden-Bell & Sandage, 1962). Progress in both theory and observations have later favoured a second formation theory: the so-called 'hierarchical formation model'. In accord to this model, it is assumed that a lot of small baryonic structures are formed within Cold Dark Matter (CDM) haloes which, over time, merge together to form the bigger structures we see today (White & Rees, 1978; Blumenthal et al., 1984).

Evidence for the hierarchical structure formation is reported by observing that massive quiescent galaxies are much more compact (effective radius 3-5 times smaller) at redshift z ~ 2 as compared to ETGs in the local universe, suggesting that local galaxies grow in size through multiple minor mergers (Daddi et al., 2005; van de Sande et al., 2013). In fact, whereas major mergers lead to growth in both size and stellar mass, minor mergers will result in size-only growth (Naab, Johansson & Ostriker, 2009). The observation of varying stellar ages of different components within the same galaxy, thereby implying star formation at different epochs, and predicted size-growth of ETGs (Loeb & Peebles, 2003) furthermore suggests that hierarchical structure formation is the favoured theory for the formation history of ETGs.

Thus we assume that ETGs form through multiple merging events. Major and minor mergers have different effects on the internal stellar populations, population parameters, and kinematics of the galaxy. Where major mergers will perturb the galaxies completely, the minor objects will not penetrate into the inner regions of the galaxy and instead will accrete onto the galaxy and affect the outer regions only. Therefore it is possible to interpret the interaction history of galaxies based on the internal distribution of stellar populations and size-growth of the galaxies (e.g. Kobayashi 2004; Kuntschner et al. 2010; Greene et al. 2015).

Numerical simulations of dissipative collapsing galaxies including star formation show strong radial gradients in chemical enrichment in the higher-mass systems (Carlberg, 1984), where dissipationless systems predict no radial gradient in chemical enrichment (Gott, 1975). During collapse the gas is chemically enriched, flows inwards, and forms new stars; this creates the radial metallicity gradient. This means that in the monolithic collapse model the metallicity gradient is steep with the highest values near the centre. In the hierarchical model this initial gradient can be shallowed by merging events due to dilution of line-strengths in the pre-merger systems (Kobayashi, 2004).

Kobayashi & Arimoto (1999) used line-strengths to study metallicity gradients and reported that the gradients do not correlate with any physical properties of galaxies including central and mean metallicity, central velocity dispersion, absolute effective radius, and dynamical mass. In fact, ETGs can have different metallicity gradients even if they have nearly identical initial physical properties as mass, luminosity, and metallicity. As it stands, metallicity gradients are reported to depend mainly on the formation history of galaxies, hence making them a good probe for past merging events.

In current formation theories two types of (minor) mergers have been defined: (i) wet mergers, which are gas-rich mergers of spiral galaxies (Toomre & Toomre, 1972), and (ii) dry mergers, which are gas-poor mergers of red non-star forming galaxies (Strateva et al., 2001). The main result of a wet merger will be a system dominated by rotation, since the gas tends to form a disk (Naab, Jesseit & Burkert, 2006), while dry mergers will result in massive red galaxies dominated by random motion (Barnes, 1992; Burkert & Naab, 2003). Therefore, stellar kinematics can be used to unravel the merging histories of galaxies.

By analysing spatially-resolved kinematics of 260 galaxies, the ATLAS^{3D} collaboration reported that ETGs can be divided into two kinematic families: slow rotators, which show only mild signs of rotation, and fast rotators, which have a more regular velocity field (Emsellem et al., 2007). They reported that 85% of the ETGs are fast rotators. It is assumed that the fast rotators form with both wet and dry mergers, whereas slow rotators form mainly via dry mergers (Naab et al., 2014).

Now that we have a better understanding on the possible formation histories of ETGs as well as their effects on internal physical parameters, we begin looking at the effects the kinematics have on the stellar populations.

1.3 Population studies in ETGs

Galactic and stellar spectra are by far the main source of information to infer formation histories and stellar populations. With the exception of very nearby galaxies, where individual stars can be observed and resolved individually, most extragalactic spectra are unresolved and stellar population studies are done by looking at the integrated light, the full Spectral Energy Distribution (SED), from all the stars in a galaxy.

It is proposed that the galaxy spectra can be broken down into one or more Single Stellar Populations (SSPs). SSPs are stars born at the same time which have the same initial elemental composition with fixed stellar population parameters (e.g. metallicity and temperature). By comparing the SSP spectra with the observed spectra it is possible to determine which stellar types has a major influence on the galaxy SED and is therefore assumed to be present in the galaxy. Tinsley (1972) introduced this method to determine stellar populations in globular clusters. Adopting this method, we use the empirical SSPs from the MILES stellar library (Sánchez-Blázquez et al., 2006). MILES is an empirical stellar library, providing us with stellar spectra of ~1000 stars over a wide range of stellar population parameters (see Section 3.3.1).

In this thesis we perform a spectroscopic study of the unresolved stellar population of galaxies based on line-index measurements. This means that we use the measurements of absorption line-strengths representing spectral features which are sensitive to certain stellar population properties like IMF-shape, metallicity, and stellar age. The absorption-line measurements are done in a narrow region of the spectrum; the absorption line of interest and two pseudo-continua on the red and the blue side of the line. The pseudo-continua are used to estimate the continuum *at* the absorption line, which is necessary to determine the absorption-line flux. The intensity of an absorption line (in Å) is given by

$$I(\text{Å}) = \int_{\lambda_1}^{\lambda_2} \left(1 - \frac{F_{I,\lambda}}{F_{C,\lambda}}\right) d\lambda \tag{1.6}$$

where $F_{I,\lambda}$ is the flux of the absorption-line between λ_1 and λ_2, and $F_{C,\lambda}$ represents the flux as if the spectrum is a straight line connecting the red and blue pseudo-continua (Burstein et al., 1984; Worthey et al., 1992). The result from this integral is also called the Equivalent Width (EW). The index magnitude is defined as

$$I(\text{mag}) = -2.5 \log \left[\left(\frac{1}{\lambda_2 - \lambda_1} \right) \int_{\lambda_1}^{\lambda_2} \frac{F_{I,\lambda}}{F_{C,\lambda}} d\lambda \right] \tag{1.7}$$

In this thesis the calculation of the absorption line strengths (referred to as line-indices) is done using the SPINDEX algorithm as reported in Trager, Faber & Dressler (2008) (see Figure 1.2).

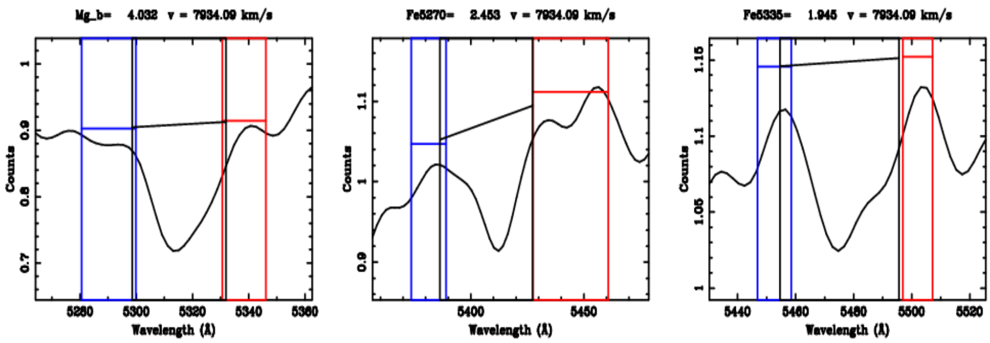

Figure 1.2: Example of three line-index measurements of standard Lick/IDS indices from a galaxy broadened to a resolution of 350 km s^{-1} as done by the SPINDEX code (Trager, Faber & Dressler, 2008). The black line represents the bandpass of the measured index. The blue and the red lines represent the red and blue pseudo-continua used to estimate the continuum in the black bandpass.

In the 1980s a system of standard absorption line indices, the Lick/IDS system, was introduced. This system consists of several indices, including their aforementioned pseudo-continuum ranges, which are used as standard indices in stellar population studies (Burstein et al., 1984; Worthey, 1994; Worthey & Ottaviani, 1997). These Lick/IDS indices include, among others, the Balmer hydrogen lines (Hα, Hβ, Hγ, ...) which are mainly sensitive to the temperature of the main-sequence turn-off stars and are therefore a good indicator of the age of the stellar population. Others, like Fe and Mg lines, are indicators of the metallicity content of the galaxy. Extended systems of indices and new definition of classical Lick-/IDS have been used and are still used as good measurements for stellar population properties (e.g. Spiniello et al. 2014). For the full set of indices used in this thesis, including their influence of stellar population properties, I forward the reader to Chapter 3.6.

1.4 The Initial Mass Function

The Initial Mass Function (IMF) is the functional form that describes the mass distribution of formed stars in a single star-forming phase. In 1955 Edwin Salpeter determined the IMF analytical form in our own galaxy. He found that the IMF (generally denoted with the greek letter ξ) as a function of mass (m) of the Milky Way follows a power-law relation with an index (x) of -2.35 (Salpeter, 1955):

$$\xi_{\text{Salpeter}}(m) = m^{-2.35} \tag{1.8}$$

This powerlaw, however, is based on the Milky Way alone and can therefore not be called a universal relation. Yet this relation has been used as a basis for IMF studies ever since. More recently alternative "shapes" of the IMF have been proposed. In Miller & Scalo (1979) it was suggested that the IMF would flatten towards the lower-mass end of the IMF. These kind of IMFs (with a dominant giant-component) are called "top-heavy" IMFs. People extended their search for the IMF-shape and in the last decade two IMF models are generally used as favourable relations for IMF studies, the Kroupa IMF and the Chabrier IMF (see Figure 1.3).

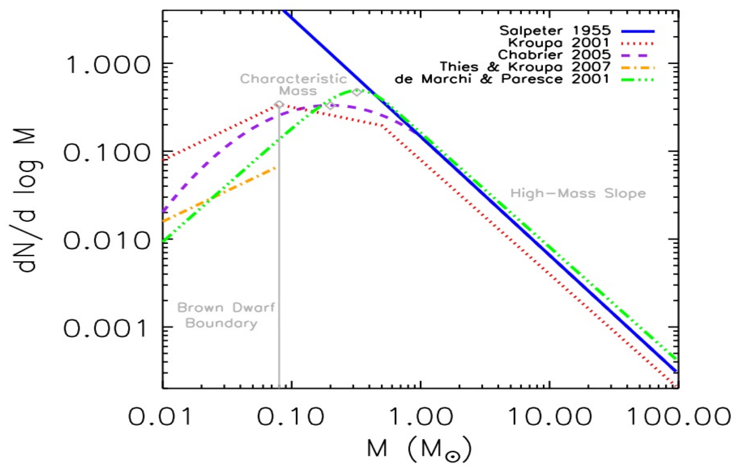

Figure 1.3: Visualization of different proposed IMF functions. The image includes the described models of Salpeter (1955), Kroupa (2002), and Chabrier (2005) [Equations (1.8), (1.9), and (1.10) respectively]. Where Salpeter predicts a continuisly rising amount of stars when you go to lower mass regions, the Chabrier and Kroupa models are top-heavy, flattening below $\sim 1M_\odot$. The image is taken from Offner et al. (2014).

Kroupa proposed a broken power-law IMF for galaxies. The idea behind this is that galaxies have different stellar populations and different populations of stars have a different IMF shape. By looking at populations from brown dwarfs ($\leq 0.072M_\odot$) to massive stars ($8M_\odot$) he defined an IMF consisting of three different powerlaws (Kroupa, 2002):

$$\xi_{\text{Kroupa}}(m) = m^{-x}, \text{where } x = \begin{cases} 0.3 & \text{for } m < 0.08M_\odot \\ 1.3 & \text{for } 0.08M_\odot < m < 0.5M_\odot \\ 2.3 & \text{for } 0.5M_\odot < m \end{cases} \tag{1.9}$$

In Chabrier (2003, 2005) a log-normal IMF is proposed, which is a smoother function than the broken power-law IMF. The Chabrier IMF also falls off at lower mass ranges and is split in two parts (formulae from Chabrier 2005 are used):

$$\xi_{\text{Chabrier}}(\log(m)) = \begin{cases} 0.093 \times \exp\left(-\frac{\log m - \log 0.2^2}{2\times 0.55^2}\right) & \text{for } m \leq 1M_\odot \\ 0.041 m^{-1.35\pm 0.3} & \text{for } m \geq 1M_\odot \end{cases} \tag{1.10}$$

These turnover (top-heavy) models are still the best fit for the Milky Way but, as we will discuss in the next paragraph, are less favoured for ETGs.

As shown in equations (1.2) and (1.4), the kinematics and stellar mass of galaxies are crucial in understanding their formation and evolution. Since stellar mass and light are produced solely from baryonic matter, but the dark matter fraction has a big influence on the galaxies kinematics, it is vital to disentangle the baryonic and dark matter fractions of the galaxy, as well as knowing how the stellar mass-to-light ratio scales with the luminous mass of the system. Having knowledge of the IMF of ETGs will tell us more about the star formation history and (if the IMF *is* dependent on velocity dispersion) the internal kinematics.

1.5 Recent studies of the IMF and stellar populations in ETGs

Recently the debate about the shape of the IMF has been very active (e.g. Cappellari et al. 2012; Conroy & van Dokkum 2012b; La Barbera et al. 2013; Spiniello et al. 2014; Martín-Navarro et al. 2015a). The simplest and most direct way to constrain the precise slope of the low-mass end of the IMF is to resolve and count stars with low masses. However, low-mass stars only give a few % contribution on the optical integrated light of a galaxy, despite accounting for more than 60-80% of the mass for a system with an old population (Worthey, 1994; Conroy & van Dokkum, 2012b).

Several approaches have been proposed to indirectly infer the low-mass IMF slope. One option is to use strong gravitational lensing to probe the IMF. In a gravitational lensing system light from a (bright) source behind the galaxy will be bent due to the mass of the lensing galaxy. By determining the degree of lensing one can get an estimate of the total mass of the galaxy. Given that most of the stellar mass is present in low-luminous dwarf stars, the discrepancy between the lensing weighted mass with the luminosity weighted mass returns and estimation on the amount of low-luminous matter of a system. A problem with this method, however, is that although it allows us to precisely determine the total projected mass within an aperture, it does not permit us to separate the mass of he dark matter fraction from luminous matter. Auger et al. (2010) explored this problem by assuming three different density profiles for the CDM haloes in ETG systems. All their models point towards a Salpeter-like IMF which, furthermore, only remains universal among different galaxies if the dark matter haloes remain universal between galaxies. Treu et al. (2010) combined strong gravitational lensing with dynamical modeling to probe the IMF. They compared the stellar mass as gained from the dynamical (lensing) models together with the stellar population models. The discrepancy between the two tends to get bigger with an increase in the galaxy's velocity dispersion. This could imply a non-universal IMF (or a non-universality in the dark matter haloes), meaning the IMF would depend on, for example, the velocity dispersion.

Van Dokkum & Conroy (2010) proposed that the amount of M dwarfs ($\leq 0.3 M_{\odot}$) is larger in ETGs than previously thought, based on dwarf-sensitive absorption features that are strong in M-dwarfs and almost absent in main sequence and giant stars. This would imply an increase in Υ_* due to a steeper low-mass end in the IMF. Other indications for a non-universality in the IMF are reported in Spiniello et al. (2012, 2014); La Barbera et al. (2013); Conroy et al. (2013); Martín-Navarro et al. (2015b). All of these studies use spectroscopic stellar population indicators. It appears from these studies that the IMF-shape is influenced by the central velocity dispersion of the galaxy, varying from a Kroupa/Chabrier IMF at $\sigma \sim 100$ km s^{-1} to an increasingly more bottom-heavy IMF for increasing σ.

The XLENS survey (Spiniello et al., 2011, 2015) combines strong gravitational lensing, dynamics, and stellar populations analysis to disentangle between dark and luminous matter and to infer the IMF slope and the internal dark matter fractions in massive lens galaxies. They link the IMF slope with the galaxy mass with the aim to investigate the relation between baryonic and non-baryonic matter during the structure formation process. Since the radial profiles of the IMF depend on the formation history of the galaxy, XLENS will shed new light on link between IMF, structure formation, and the role of dark matter.

Finally, time-evolving IMFs have also been proposed. For instance, Davé (2008) investigated the stellar mass-star formation relationship (M_*-SFR) to look at the stellar mass assembly histories of galaxies. He defined the star formation activity parameter ($\alpha_{\rm sf}$), which represents the fraction of the Hubble time that a galaxy needs to have formed stars at its current rate in order to produce its current stellar mass. He reported that his models predict a constant $\alpha_{\rm sf} \sim 1$ out to redshift z = 4, while observations indicate that $\alpha_{\rm sf}$ roughly triples between z = 2 and z = 0. As a solution he proposed an IMF that evolves to become more bottom-light with increasing redshift, where the turn-over mass of the IMF evolves with $\hat{M} = 0.5(1+z)^2\ M_\odot$ out to z ~ 2. Such a time-evolving IMF works well with objects at z=0 and manages to relieve some of the tension between the IMFs reported in fossil-light measurements (where a bottom-light tri-model IMF is the best fit, Fardal et al. 2007) and the observed cosmic star formation histories.

1.5.1 IMF studies in non-ETG objects

Salpeter (1955) originally derived his relation from nearby structures within the Milky Way. Since then, IMF studies began with nearby star-forming regions and globular clusters and from there evolved to study other galaxies. For various structures within the Milky Way the IMF is reported to be remarkably consistent. The general trend is that the IMF agrees well with the Salpeter IMF in super-solar mass range, whereas in the sub-solar mass range the slope tend to shift towards a Kroupa/Chabrier IMF. This is seen in populations of field stars, nearby open clusters, star-burst regions, and the galactic centre. Nearby galaxies like M33 and the Magellanic Clouds follow Salpeter in the super-solar mass range as well. For an overview of IMF-studies regarding these objects I refer the reader to Bastian, Covey & Meyer (2010).

The IMF in late-type galaxies (LTGs) requires a different approach than the ones used for ETGs since these galaxies have a complex morphology. Spiral galaxies tend to have younger populations, have active star-forming regions in the spiral arms and are yet to undergo a major-merger event. Since the stellar population of LTGs is younger, a different mass range of the IMF is constrained. In ETGs all stars above 1.5 $M_\odot$ are dead, enabling us to focus on the low-mass IMF slope, a feature that is much more difficult in LTGs since here stars with M > 1.5 $M_\odot$ dominate the spectrum. As with the IMF in ETGs, over the last few years, evidence has emerged in favour of a time-dependent IMF for LTGs. Hoversten & Glazebrook (2008) reported that fainter galaxies have a steeper IMF slope as compared to brighter ones. In general, in LTGs the steepness of the high-mass end of the IMF appears to be sub-Salpeter, and becomes even shallower with an increasing star-formation rate (SFR) (Gunawardhana et al., 2011). Defining a global IMF within LTGs remains difficult, since the star-formation events are local (few pc) and happen in a short timescale (about 10 Myr). The size of the events makes it impossible to apply the Milky Way IMF results directly to extra-galactic objects.

Since extra-galactic objects are unresolved most of the time, substructures do not play a significant role in IMF determination in these objects and instead it is common to determine the Integrated Galactic stellar Initial Mass Function (IGIMF). The IGIMF is the sum of the galaxy's constituent stellar populations (Weidner & Kroupa, 2005; Weidner et al., 2013b). The assumption here is that the IMF locally follows the 'standard' IMF-relation, but galaxy-wide it must be weighted with the mass-distribution function of stellar clusters within which star formation takes place. Heavier clusters tend to fill up heavier stellar mass-ranges, whilst smaller star-forming regions will have a lower high-mass cutoff, thereby causing a variation of the IMF-slope between high-mass and low-mass star-forming regions. Weidner et al. (2013b) list seven axioms which describe extensively which parameter values are assumed to describe potential star-forming regions as well as the mass-distribution function of a galaxy. These axioms make it possible to calculate the IGIMF as a function of galaxy-wide SFR and metallicity. The IGIMF is succesful when it comes to describing the Milky Way and its surrounding tidal dwarf satellites (Recchi, Kroupa & Ploeckinger, 2015) as well as nearby dwarf galaxies as the Sagittarius dSph (Vincenzo et al., 2015) and Fornax dSph (Li, Cui & Zhang, 2013). In recent work, Fontanot et al. (2016) applied the IGIMF theory to the GAEA semi-analytic models with the aim to study the effects a universal IMF and the IGIMF have on galaxy mass assembly and on chemical abundances. They reported that the IMF models manage to predict local scalings of luminosity-weighted age, metallicity, and stellar mass, but that only the IGIMF predicts the observed [α/Fe]-M_*. In addition, only the IGIMF model is able to recreate the bottom-heavy IMFs that are expected in ETGs. Yet, these models still have difficulty predicting the star-formation histories, because the IGIMF is only able to predict the highest star formation event of a galaxy and not overal star formation timescales. Although promising, the IGIMF theory is not yet complete since it must be able to explain and reconcile all the observational results on different scale and different systems, in order to be considered successful.

1.6 This thesis

In the previous paragraphs we mention a lot of debate regarding both the shape of the IMF and its consistency over time. In this thesis we analyse the IMF and other stellar population properties of nearby ETGs ($z < 0.03$) *within* the galaxies itself. We want to see if the IMF is varying within single systems as well as study how dependent the IMF is on the galactic environment, stellar kinematics, and formation history.

In this project we focus on spectral analysis aimed at finding dwarf/low-mass stars in ETGs. Spectra of dwarf stars show some distinct features that the bigger stars lack. Low-mass stars have a larger gravity component as opposed to their bigger counterparts. Van Dokkum & Conroy (2010) and Spiniello et al. (2012, 2014) showed that there are absorption lines which are gravity-sensitive, making them good tracers for the low-mass star populations. By analysing the gravity sensitive absorption lines we can determine, via the abundance levels of these lines, how prominent dwarf stars are present in a spectrum. Conroy & van Dokkum (2012b) focused their attention on gravity-sensitive lines arising from iron, sodium, carbon, calcium, and magnesium. They reported that the IMF is more bottom-heavy than a Salpeter IMF ($x > 2.35$) for very massive galaxies. Other regions of the spectra are discovered to be gravity sensitive as well; for example the TiO and CaH lines used by Spiniello et al. (2014). These lines show different strengths for stars with different gravity, being strongly present in cool dwarf stars, more weakly present in cool giant stars, and are almost completely absent in other main sequence stars. They can therefore be used to estimate the giant-to-dwarf ratio and to compare this to the total stellar mass.

In this research we use data from the Calar Alto Legacy Integral Field Area survey (CALIFA, Sánchez et al. 2012). CALIFA is observing 600 nearby galaxies with an integral field spectrograph. The latter means that the data contains the spectra of an extended object on the sky as a function of position. We can split these galaxy's spectra into multiple regions, giving us the opportunity to check for variations in different parts of the system. The MILES empirical stellar library is used to fit the line-of-sight velocity distribution. Absorption line-indices are then measured in the spatially-resolves spectra of each galaxy and compared with same indices in stellar population models from Conroy & van Dokkum (2012a) to determine which set of stellar population parameters best describe the stellar population within the system.

During the writing of the thesis the Martín-Navarro et al. (2015c) paper was published. They used the CALIFA data of 24 ETGs and investigated radial variations in the IMF. They reported that the IMF varies over radius and that the IMF has a tight correlation with metallicity. This work is similar to our work here, but differs in a few points. First, in fitting the stellar populations models we vary the low-mass end of the IMF whereas Martín-Navarro et al. (2015c) varies the high-mass end ($> 0.6\,M_\odot$). Second, we focus more on the radial variations in stellar population parameters and on the gradients themselves with the goal of finding similarities in radial trends of the various parameters and linking these values with the galaxy's formation history. We compare this thesis with the work of Martin-Navarro and collaborators extensively in Section 4.3.

This thesis is structured as follows. In Chapter 2 we describe the CALIFA data: how the data is observed, reduced, and how we select our samples from the survey. In Chapter 3 we describe the algorithms and methods used to calculate the indices including a description of the binning procedures, the pPXF algorithm for calculating stellar kinematics, the GANDALF routine for removing emission lines, and the SPINDEX code which is used to determine absorption-line indices. In Chapter 4 we present the main results. Here we show which indices relate best to which parameters, and how the parameters vary within different radii of the galaxies. We also speculate about the possible formation histories of the galaxies based on the radial gradients. In Chapter 5 we discuss the corrections to the data we made and the encountered limitations present within the data. We compare the results with other recent works which graze the topic of this thesis and present some ideas for future research. In Chapter 6 we present the main conclusions we draw from the research.

2

The CALIFA survey

In this project we use data as provided by the Calar Alto Legacy Integral Field Area survey (CALIFA)[1]. The term *legacy* is significant in CALIFA's philosophy, meaning that the survey data should become public at a regular basis after data reduction and thorough quality control. CALIFA combines imaging and spectroscopy of galaxies through Integral Field Spectroscopy (IFS), a technique that allows us to gather spectra of an object on the sky over a two-dimensional field-of-view. This technique is nowadays the most used and most efficient way to obtain spatially resolved spectra.

The goal of CALIFA is to gain a better understanding of baryonic physics in the Local Universe by addressing fundamental issues in galaxy evolution and will allow us to address questions about internal galaxy dynamics, star formation histories, and stellar population studies[2].

CALIFA uses the PMAS/PPAK spectrograph (Kelz et al., 2006) mounted on the Calar Alto 3.5 m telescope, which has one of the largest Field of View (FoV) for this kind of instrument in existence (FoV > 1 arcmin^2). Once complete, the survey will encompass ~600 galaxies in the Local Universe in two overlapping grating setups: the V500 in the red (3750-7000 Å, spectral resolution of 6.0 Å FWHM), which will allow for studies on ionized gas and stellar populations, and the V1200 in the blue (3700-4700 Å, spectral resolution of 2.3 Å FWHM) which will allow for detailed stellar kinematics studies (Sánchez et al., 2012).

In this thesis we make use of data obtained with the V500 grating. For this reason, in this chapter and in the following ones, we will limit our discussion to the pipeline process used for this configuration.

2.1 CALIFA data sample

Since CALIFA wants to produce high-quality, resolved galaxy spectra the survey is interested in nearby and bright galaxies only. The selection procedure of the survey galaxies is described in Walcher et al. (2014). The CALIFA 'mother sample' is taken from the Sloan Digital Sky Survey (SDSS, York et al. 2000) DR7 catalogue[3]. The mother sample is selected by adopting some initial prerequisites: (A) an r-band isophotal major axis between 45" and 79.2" at the R25 radius[4], (B) redshift $0.005 < z < 0.03$, (C) position in the sky; herein excluding the galactic plane by cutting the latitude between $-20° < b < 20°$, and limiting the location on the sky by constraining the hour angle and declination to $-2h < HA < 2h$

[1] `http://www.caha.es/CALIFA/`
[2] For a complete list of CALIFAs scientific goals and characteristics I refer the reader to Sánchez et al. (2012)
[3] `classic.sdss.org/dr7/`
[4] The isophote at which the surface brightness = 25 mag.

and $\delta > 7°$ respectively to make sure to take into account the range of the instrument, (D) airmass below X < 1.5 to avoid too much atmospheric refraction. These selection criteria generate a mother sample of 939 galaxies from which 600 are (almost) randomly selected to be observed by CALIFA.

In this research we use data from the first two data releases of CALIFA (Husemann et al. 2013; García-Benito et al. 2015; for DR1 and DR2 respectively), in which the data of 200 galaxies have been made available. The observations up until DR2 have been made between June 2010 and December 2013. Since starting this thesis CALIFA has released DR3 (Sánchez et al., 2016), but these have not been included in this work.

2.1.1 The CALIFA pipeline

In the following section we describe briefly how the CALIFA data cubes are reduced. For a full and detailed description of the pipeline process I refer the reader to Sections 5 and 6 of Sánchez et al. (2012) and Section 3 of García-Benito et al. (2015) for the latest pipeline updates concerning the data used here.

The PMAS/PPAK spectrograph has a total FoV of 74" × 64". The Integral Field Unit (IFU) consists of 331 fibers in a hexagonal grid where each fiber projects to 2.7" in diameter on the sky. The fiber-to-fiber distance is 3.2", yielding a filling factor of 0.6 (Kelz et al., 2006). In order to reach a filling factor of unity, a three-pointing dithering scheme is used for each object. V500 observations take 900 s per pointing.

From every observation, the sky is subtracted and the flux is calibrated. The latter is done by comparing spectrophotometric standard stars from the Oke catalogue (Oke, 1990) with PPAK observations of those stars on every night, creating a response curve to apply to the observations thereby ensuring there is consistent calibration on the entire survey region.

After reduction, the dithered exposures are combined to a single frame of 993 spectra which are rescaled to a common intensity and response function. Then the data is resampled to a data cube with a regular grid using Shepard's Interpolation Method to assure flux conservation (Shepard, 1968). With this method, the intensity of each interpolated point is the sum of the weighted average of the intensities corresponding to n adjacent points within boundary distance r_{lim}, and can be used to assign values to unknown points based on their surrounding spaxels[5]. The flux (F) of an unknown spaxel is calculated with the equation

$$F(i,j,\lambda) = \sum_{k=1}^{k=n} w_{i,j}^{k} f_{k,\lambda} \quad r_{1...n} < r_{lim} \tag{2.1}$$

where $F(i,j,\lambda)$ is the reconstructed intensity in pixel (i,j) at wavelength λ, $w_{i,j}^{k}$ is the weight of the pixel at adjacent spectrum k, and $f_{k,\lambda}$ is the intensity of the adjacent spectrum at that same wavelength. The weights of the pixel originate from the Gaussian function:

$$w = N \exp\left[-0.5\,(r/\sigma)^2\right] \tag{2.2}$$

with r the distance between pixel (i,j) and spectrum k, σ the width of the Gaussian, and N being a normalization parameter, which is derived for every interpolated pixel using

$$N(i,j) = \frac{1}{\sum_{k=1}^{k=n} w_{i,j}^{k}} \quad r_{1...n} < r_{lim} \tag{2.3}$$

This interpolation guarantees the preservation of integrated flux. The limits used in CALIFA are r_{lim} = 5" and σ = 1", creating a final data-cube with a pixel scale of 1"/pixel.

[5]A spaxel is a spectrum of one pixel

The data is then absolute flux-calibrated after the spatial rearranging with SDSS photometry. Absolute flux calibration is applied for continuum flux densities at a given wavelength at any spaxel and transforms the prior calibrations into physical fluxes (Padmanabhan et al., 2008). Since the bandpasses of the SDSS g band (λ_{eff} = 4770 Å) and r band (λ_{eff} = 6231 Å) are fully covered in the V500 wavelength range, these two are used for recalibration. The absolute flux level of each V500 data cube is rescaled to match the SDSS DR7 broad-band photometry within an aperture of 30" diameter.

The accuracy of the wavelength calibration in the V500 data cube is 10-15% of the pixel scale, i.e. the root mean square (rms) of the spectrum is in the order of 0.2-0.3 Å. This value is obtained by comparing the nominal and recovered wavelengths of prominent night-sky emission lines, derived from the median offset and the rms of each data set. As the night-sky lines are unresolved, they also give the best estimate in determining the resolution of the data sets. For V500 the spectral resolution is homogenised to reach a target FWHM of 6 Å, which corresponds to an instrumental velocity dispersion of $\sigma_{V500} \sim 150$ $\mathrm{km\,s^{-1}}$.

The pipeline gives a rough estimation of the Signal-to-Noise ratio (S/N) in each spectrum within the reduced data cube. The median and standard deviation of the intensity is computed in the 4480-4520 Å wavelength range. This region is chosen since this part lacks strong spectral features and is present in both the V500 and V1200 gratings. Assuming the scatter is entirely due to noise, the S/N per spaxel is determined to be

$$\frac{S}{N} = \frac{\sigma_{i,j}}{\langle F_{i,j} \rangle} \tag{2.4}$$

where $\sigma_{i,j}$ is the standard deviation in spaxel (i,j) and $\langle F_{i,j} \rangle$ is the median flux at that spaxel. A S/N is obtained by applying Equation 2.4 to all the spaxels in the data cube from which it is possible to determine detection limits of the data. Spaxels with a low-enough S/N will not only contain little information about the source, but this information will also be hard to distinguish from the observed background flux. The lower limit is set to S/N $\sim$ 3-4, when the 3σ detection limit of the instrument is approached. The flux that corresponds to this level is, for the V500 data, ~23.0 mag/arcsec.

2.2 Data selection

In this work we only select ETG galaxies from the mother sample of the survey. Furthermore, we prefer to have isolated galaxies, whose internal kinematics is not influenced by near-by interacting galaxies and which are not undergoing active merging with other objects. The galaxies used in this study, along with some of their basic properties, are listed in Table 2.1. The half-light radius (R_{eff}) is taken directly from the CALIFA website (in arcsec) and converted to parsec using the cosmological parameters H_0 = 70 km s^{-1}, Ω_m = 0.3, and Ω_Λ = 0.7.

Table 2.1: List of sampled CALIFA galaxies

Name	Redshift(z)[6]	R_{eff} (arcsec)	R_{eff} (kpc)	Hubble Type
NGC0499	0.015	21.4	6.39	E5
NGC1349	0.022	17.0	7.58	E6
NGC5966	0.015	18.6	5.66	E4
NGC6020	0.014	19.0	5.57	E4
NGC6125	0.016	21.8	7.14	E1
NGC6146	0.029	15.0	8.86	E5
NGC6150	0.029	11.9	6.93	E7
NGC6173	0.029	38.0	22.32	E6
NGC6338	0.027	28.1	15.49	E5
NGC6411	0.013	34.1	8.86	E4
NGC6515	0.023	19.0	8.78	E3
NGC7194	0.027	17.8	9.61	E3
NGC7562	0.012	21.0	5.16	E4
UGC05771	0.025	12.7	6.31	E6
UGC10693	0.028	23.0	12.89	E7
UGC10695	0.028	24.6	13.70	E5
UGC12127	0.028	36.4	20.18	E1

[6]Retrieved from NED. `https://ned.ipac.caltech.edu/`

3

Method and software

In this chapter we present the methods and algorithms we apply to get from the CALIFA data cube to the absorption-line indices we need to infer stellar population parameters on a step-by-step basis. First we show what is included in the CALIFA cube and how we extract the data. From the data we filter out unwanted information (e.g. background objects and bad pixel regions) and rebin the data in three different ways: Voronoi bins, radial bins, and elliptical bins. The method of rebinning and its purposes will be described. Then, we also describe which stellar templates we use to constrain the line-of-sight velocity distribution (LOSVD) and why these are chosen. What follows is the determination of the kinematics of the individual bins with pPXF, removing emission lines with GANDALF, and retrieving absorption line indices with SPINDEX. To conclude we show how we determine the best-fitting stellar population parameters using index-comparisons of Single Stellar Populations (SSPs) and χ^2-statistics.

3.1 The CALIFA cube

Our sample consists of 17 ETGs in which we analyse the stellar population properties. From the CALIFA website[1] we retrieve the raw data cubes of the galaxies which fit our preliminary constraints as described in Section 2.2. We refer to the CALIFA data as a cube as the data encompasses two spatial dimensions and a wavelength dimension: (x, y, λ)[2]. The initial CALIFA cube is a structure consisting of five layers (García-Benito et al., 2015).

Signal
: The amount of input flux per pixel, calculated using Equation (2.1), in units of 10^{-6} erg s^{-1} cm^{-2} Å^{-1}.

Noise
: The noise is determined with the standard deviation and intensity as given in Equation (2.4).

Weight
: The weights are included due to CALIFA's spatial re-arranging of the data as given in Equation (2.2). The weights represents the fraction of the data from a fibre to be present in a certain spaxel.

Good Pixel
: A boolean layer which is CALIFA's way of showing which pixels might have to be excluded from the analysis. This can be because of cosmic rays, bad CCD columns, or vignetting effects. The uncovered corners of the FoV are also flagged as bad pixel regions.

[1] `http://califa.caha.es`

[2] The dimensions of a CALIFA data cube are $(x, y, \lambda) = (78, 73, 1877)$

Fibre Cover
Layer that shows the number of fibres used to fill each spaxel to a filling factor of unity.

To extract the galaxy in a proper way we first need to decide which of our pixels actually contain information about the galaxy, i.e. we need to define the edges of the system. This is done by setting a lower limit to the S/N ratio as a cut-off to whether or not a pixel contains (galaxy) signal or mainly (background) noise. We define a spaxel as part of the galaxy data if S/N > 3 is achieved. This is similar to Sánchez et al. (2012), where a lower limit of (3 < S/N < 4) is defined because the average flux of these spaxels is considered to be a rough estimation of the 3σ detection limit of the instrument (See Chapter 2).

After masking spaxels below the S/N cut-off limit we need to include the possibility of other fore- and background objects that might be present is the data-cube that, if remained unnoticed, will pollute the galaxy data. Some of these can be easily seen by eye, but for a more thorough check we put the cubes through two algorithms to filter out these regions.

First we put the data through a median filter algorithm. The median filter tends to 'smooth out' the image by assigning to each spaxel the median value of its surrounding spaxels. This way more fainter objects and small (pixel-sized) anomalies can be traced and masked. Second, we fit the intensity-profile of the galaxy with a de Vaucouleurs-type light profile (Equation 1.1). Potential foreground objects near the line-of-sight of the galaxy can be detected from the galaxy's brightness profile as they cause deviation of the data when fitted with the de Vaucouleursesque type of brightness profile which is expected for these type of galaxies. The latter step is necessary since objects near the galactic centre will blur in with the galaxy data and can therefore be missed in the median filter algortihm.

3.2 Binning the data

After proper extraction of the data we rebin them. Binning is necessary because a) many individual spaxels have a low S/N, which makes it difficult to extract information without generating huge uncertainties and b) the software packages we use require a minimum of S/N ~ 80. We use three different methods of binning. First, we divide the data into Voronoi bins of equal S/N. By combining multiple spaxels into a single spectrum, we create multiple spectra per galaxy with a similar S/N level. We will also bin the data in radial and elliptical bins. Radial and elliptical binning allows us to analyse stellar population properties as a function of radius. Both of these binning procedures allow us to determine radial variations in stellar population properties, whereas elliptical binning also follows more the contour of the galaxy, thereby binning regions into chunks with a more similar physical background.

We use the Voronoi binning scheme as presented by Cappellari & Copin (2003). This is an adaptive binning scheme, where the size of the bin is adjusted to the local S/N level of the data[3]. With this method, near the centre of the galaxy the bins consist of one or a few spaxels, whereas near the edges (where the S/N is ~ 3) the bins are bigger, since we need more spaxels to create a spectrum with a high enough S/N.

We Voronoi-bin the galaxies in such a way that the S/N ~ 135 for every bin. We pick this values because (A) the software we use needs at least a S/N ~ 80-100 to work properly (see Section 3.3), (B) we want a limited number (~10) of single-pixel bins and (C) we want a total number of between 50 and 150 bins for most galaxies. The total number of Voronoi bins extracted from the galaxies are listed in Table 3.1. The Voronoi binning returns a list of pixels wherein each pixel is assigned a bin number. We combine the pixel-spectra with similar bin numbers to form one (binned) spectrum. The signal (S) and

[3] The code is retrieved from Cappellari's website: `http://www-astro.physics.ox.ac.uk/~mxc/software/`

noise of the new bins are calculated with

$$\langle S\rangle_\lambda = \sum_i \frac{S_i}{\sigma_i^2} \Big/ \sum_i \frac{1}{\sigma_i^2} \tag{3.1}$$

$$\sigma_\lambda^2 = 1 \Big/ \sum_i \frac{1}{\sigma_i^2} \tag{3.2}$$

where σ^2 is the variance of the spectrum ($\sigma \equiv \varepsilon$, where ε is the noise as given by the CALIFA data cube), i represents all spaxels in the bin, and the subscript λ means this is done for every wavelength element.

We add one small operation to the binning procedure, because in CALIFA the noise in adjacent spaxels is correlated and this results in an underestimation of the noise in stacked spectra. To circumvent this underestimation García-Benito et al. (2015) suggests to calculate the noise spectrum with the noise correlation ratio, β, which is defined for CALIFA as

$$\beta(N) = 1 + 1.07 \log N \tag{3.3}$$

where N is the number of stacked spaxels. Normally the error spectrum for a bin is given by

$$\varepsilon_B^2 = \sum_{k=1}^{N} \varepsilon_k^2 \tag{3.4}$$

where the subscript k are the individual spaxels within the bin, assigned with subscript B. The 'real' noise is than given by

$$\varepsilon_{real,B}^2 = \beta(N)^2 \times \varepsilon_B^2 \tag{3.5}$$

This correction is done for bins with fewer than 80 spaxels. For details I forward the reader to subsection 3.2 and Appendix A in García-Benito et al. (2015).

To analyse the data not locally but as a function of radius, we bin the data in radial and elliptical annuli. Radial binning is commonly used to examine radial variations in galaxy properties and stellar populations. We determine the annuli of the bins to be fractions of the effective radius (R_{eff}). Specifically, we define four annuli to have an outer radius of [1, 1/2, 1/4, 1/8]$\times R_{eff}$. The signal and noise of these spectra are calculated, like the Voronoi bins, with Equations 3.1 through 3.5.

Elliptical binning follows more the contour of the galaxy, thereby binning regions into chunks with more similar physical background. As discussed in Section 1.2, an ETG's kinematics might be dominated by rotation or random motions. In the former case we assume that ETGs are deformed by rotation, and therefore the radial gradient of the galaxy's kinematics are also elliptical. In the latter case this is not necessarily the case, but by binning elliptical instead of radial we prevent bins in which parts of the bin is part densely populated with the galaxy's stars and part solely consisting of the outer halo.

To deform a radial bin to an elliptical bin we take into account two things. First we need to determine the eccentricity, which is the elongation of the projected image of the galaxy, and orientation of the galaxy along the line-of-sight. The former is necessary to determine the ratio between the major- and minor-axis, and the latter determines the angle in which we need to fit our ellipse. Second, we want to conserve the area of the radial bins. This is done by determining the size of the semi-major axis (SMA) of the ellipse, which is half the ellipse's major axis, to be related to the original radius as

$$\mathrm{SMA} = \frac{\mathrm{R_{eff}}}{\sqrt{1-\varepsilon}} \tag{3.6}$$

where ε is the eccentricity of the ellipse. ε also describes the ratio between the SMA and the semi-minor axis, allowing us to fit an ellipse. The orientation and eccentricity of the galaxy are determined using

Cappellari's **find_galaxy** routine[4]. In Table 3.1 are shown both ε and R_{eff} of our galaxy sample.

After properly rebinning and stacking our spectra we can now extract stellar kinematics and stellar population parameters from the data.

3.3 The MILES stellar templates and the CvD12 SSP models

To investigate physical properties of stellar populations we compare the data with models which have clearly defined stellar population parameters. This way we can deduce from the best-fit population models what the underlying stellar population of a spectrum is. We use stellar templates as models to fit to the galaxy spectra.

In this project we use the Medium-resolution Isaac Newton telescope Library of Empirical Spectra (MILES)[5] as stellar templates. MILES, as the name implies, is a collection of empirical stellar spectra with well defined stellar population parameters. The library consists of 985 single stars in the 3525-7500 Å wavelength range with a mean spectral resolution of 2.5 Å FWHM. It contains a medium resolution spectral library over a large portion of the Hertzsprung-Russell diagram and gives a high dynamic range over several parameters in stellar population like temperature, gravity, and chemical abundances (Sánchez-Blázquez et al., 2006; Falcón-Barroso et al., 2011).

The MILES library is used by Conroy & van Dokkum (2012a) to create Single Stellar Population (SSP) models. These models, henceforth referred to as CvD12, are spectra composed of various stellar spectra selected based on a certain set of environmental variables; IMF-slope, stellar age, metallicity, temperature, [α/Fe], and [Na/Fe]. The CvD12 models are built to span a wavelength interval of 0.35 μm < λ < 2.4 μm with a resolving power R ~ 2000, and are composed from two empirical stellar libraries, MILES and IRTF (Cushing, Rayner & Vacca, 2005). In Section 3.7 we use CvD12 as a stellar template library to determine stellar population properties of the spectra. CvD12 models have clearly defined stellar population parameters and, when used to fit a spectrum, enables us to extract stellar population parameters from the spectrum.

3.4 Estimating kinematics: pPXF

Stellar kinematics have a significant influence on the observed spectra. The emitted light is undergoing Doppler shifts due to stellar motion, causing a distribution of velocities along the line-of-sight, the Line-Of-Sight Velocity Distribution (LOSVD). This distribution describes the spread of observed stellar motion around the general velocity (V) of the galaxy, which in its turn is mainly caused by the galaxy's redshift. This spread causes light to be emitted at different Doppler-shifts, causing line-broadening of absorption lines and a general 'smoothing' of the entire spectrum (Sargent et al., 1977).

For our purpose we want to compare the spectra from different galaxies as if they are emitted by sources with similar kinematics. To achieve this we convolve our spectra to a similar resolution. This means we voluntarily increase the velocity dispersion (σ) of a spectrum by *smoothing* it. Smoothing a spectrum means we broaden the galaxy spectra, thereby simulating a fixed LOSVD causing us to sacrifice information in exchange for the ability to compare the spectra in a qualitative way (see Figure 3.1b).

To smooth our spectrum we first need to get an initial estimate of the stellar kinematics of the spectra. For this we use the penalized PiXel Fitting (pPXF) routine by Cappellari[4]. This software allows us to retrieve up to 6 parameters of stellar kinematics: rotation, velocity dispersion, and up to four further

[4] `http://www-astro.physics.ox.ac.uk/~mxc/software/`
[5] `http://miles.iac.es/pages/stellar-libraries/miles-library.php`

orders in the Gauss-Hermite series ($h_3, \ldots, h_6$) (Cappellari & Emsellem, 2004). pPXF calculates the kinematics in the likely situation that it can be described with a Gauss-Hermite series; this means that the LOSVD is derived from the parameters of a Hermite distribution, which is a higher-order Gaussian-like distribution that is less sensitive to the uncertainties in the dynamics than a standard Gaussian distribution (Gerhard, 1993; van der Marel & Franx, 1993).

pPXF convolves the template spectra of SSP models to an initial guess of the velocity dispersion. By default, the initial guess of the velocity dispersion is set to be 3 × velocity scale, which is the velocity in units of [km s^{-1} px^{-1}]. The algorithm then proceeds to perturb the kinematic parameters around this initial guess and fits it to the galaxy spectrum. The best-fit parameters are determined by minimizing the χ^2 - which is the agreement between convolved model and spectrum (assuming Gaussian uncertainties) - for different kinematic values. The output of the program will be the best-fit estimate of the rotation velocity and velocity dispersion and is used as the initial kinematics of the galaxy's spectra. The σ_{inner} columns in Table 3.1 shows the velocity dispersion of the inner annuli of the Elliptical binning method estimated by pPXF.

Table 3.1: List of galaxy properties

Galaxy	σ_{inner} [km s^{-1}]	Eccentricity (ε)	R_{eff} (arcsec)	Nr. of Voronoi bins
NGC0499	293	0.61	21.384	113
NGC1349	218	0.89	17.028	24
NGC5966	196	0.60	18.612	87
NGC6020	210	0.73	19.008	63
NGC6125	268	0.91	21.780	148
NGC6146	314	0.77	15.048	53
NGC6150	243	0.48	11.880	41
NGC6173	263	0.65	38.016	85
NGC6338	326	0.66	28.116	55
NGC6411	190	0.68	34.056	165
NGC6515	190	0.78	19.008	45
NGC7194	276	0.79	17.820	66
NGC7562	258	0.68	20.988	193
UGC05771	239	0.71	12.672	29
UGC10693	262	0.68	22.968	90
UGC10695	203	0.67	24.552	21
UGC12127	285	0.85	36.432	61

3.5 Removing emission lines: GANDALF

The next step is to clean our spectra by removing emission lines. Besides making sure there is a minimum of pollution in the spectra caused by fore- and background objects, we also need to make sure there is no pollution from emission lines. Emission lines have an effect on the shape of the continuum of the spectra by causing a peak in flux or, in the worst case scenario, overlapping with absorption lines, causing the rise in flux to make an absorption line less deep or even just replacing the absorption line with the emission line.

Emission lines can be telluric, like nitrogen and sulfur, or they can originate from gas (nebular) emission within the galaxy. This emission can ionize oxygen, nitrogen, and sulfur as well as influence hydrogen lines from the Balmer series. The difference between the two types of emission must be made since the gas emission comes from the galaxies themselves and is therefore redshifted along with the galaxy spectrum, whereas telluric lines come from our own atmosphere and thus are emitted in the observer's frame.

To identify and remove emission lines from the spectra we apply the software described in Sarzi et al. (2006): Gas AND Absorption Line Fitting (GANDALF). Like pPXF, GANDALF uses stellar templates to fit to a spectrum. The first step in GANDALF is masking wavelengths of the spectrum that have potential emission lines. Then the remaining unmasked regions of the spectra are used to fit to the stellar templates. Based on the best-fitted templates, GANDALF looks at the flux those templates inhabit in the masked region of the original spectrum. The difference between this flux and the original spectrum at the assigned wavelength range is taken to be the intensity of the emission line, which GANDALF then substracts from the original spectrum, creating an emission-less spectrum of the galaxy. Figure 3.1a shows an example of an emission-rich spectrum (black line) and a clean spectrum corrected by GANDALF (red line).

GANDALF has the freedom to combine multiple MILES stars to the spectrum in order to create a best fit. In general GANDALF stacks between one and five stellar templates with distinct weights per spectrum in order to create a best-fit convolved template spectrum. The difference between the model and the (clean) spectrum is used to create a variance spectrum (σ_{var}) of the GANDALF output.

$$\sigma_{var} = \left(F_{bf} - F_{nt}\right)^2 \tag{3.7}$$

where F_{bf} is the flux of the best-fit model and F_{nt} is the flux of the GANDALF corrected spectrum. σ_{var} is used to estimate errors in the absorption-line indices.

3.6 Calculating indices: SPINDEX

After cleaning the spectrum and getting an estimate of its kinematics, we smooth the observed spectrum based on the results from pPXF. Results from pPXF show that the central velocity dispersions of our sample galaxies vary between 190-330 km s^{-1} (See Table 3.1). Therefore we take a LOSVD of σ = 350 km s^{-1} to be the final resolution of our spectra. After smoothing we assume that each spectrum originates from similar stellar kinematics and can be compared with each other. An example of a convolved spectrum is presented in Figure 3.1b.

We calculate the indices using the SPINDEX algorithm from Trager, Faber & Dressler (2008). As described in Section 1.3, SPINDEX extracts the intensity of absorption lines by integrating the difference of the absorption line with its assumed underlying continuum, which is based on the surrounding continua of the line. $\sigma_{\rm var}$ shows the discrepancy between the best-fit model and the data. Since there is a mismatch between the model and galaxy, there should be an uncertainty in the GANDALF-calculated emission line as well. The variance spectrum is used to calculate the uncertainties in the absorption line indices.

The relevant indices which are measured by SPINDEX are listed in Table 3.2. The first column indactes the index' name, the two following columns show the index bands and the pseudo-continua, respectively. The fourth column highlights the stellar population properties to which that particular index is most sensitive to. bTiO, aTiO, TiO1, TiO2, CaH1, and CaH2 are broad spectral features and are measured in units of magnitude, whereas Hβ, Mg$_{\rm b}$, Fe$_{5270}$, Fe$_{5335}$, and NaD are narrow spectral features and are measured in units of Å (Equations 1.6 and 1.7).

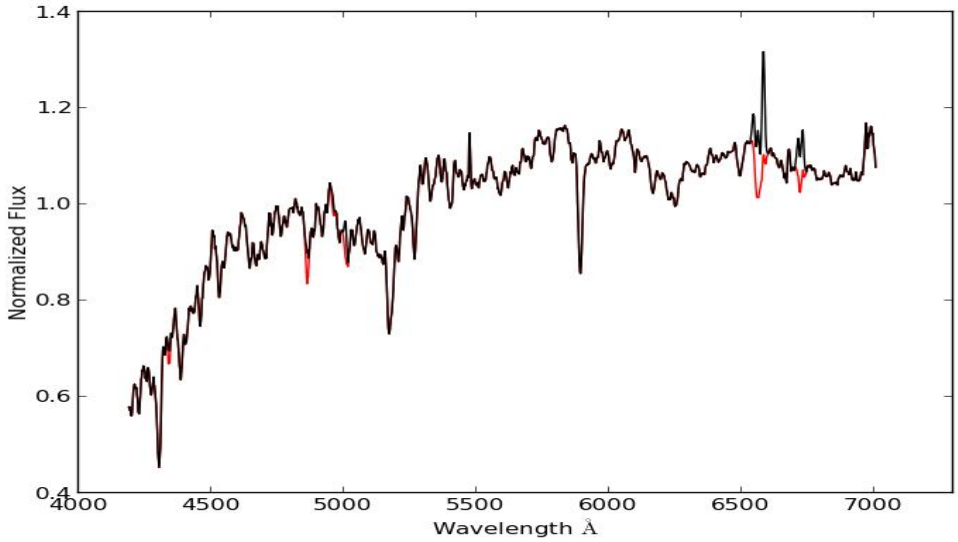

(a) GANDALF output

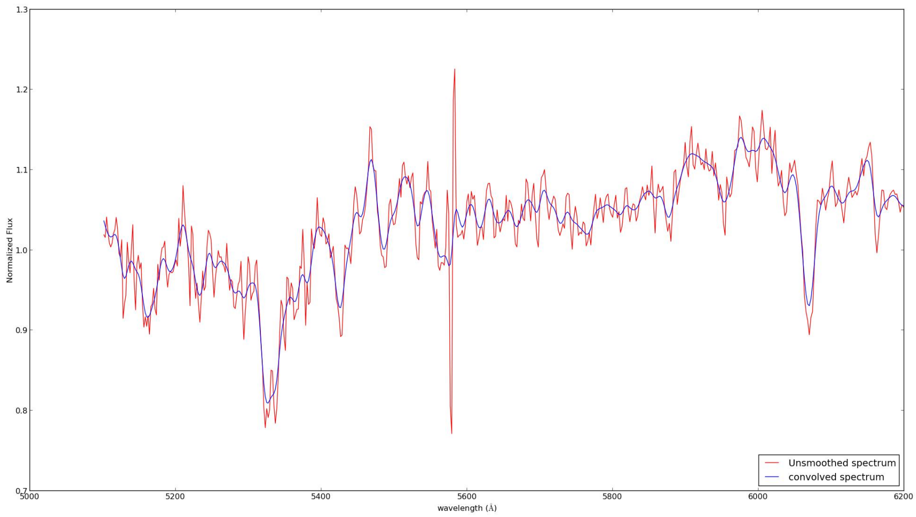

(b) Convolved spectrum

Figure 3.1: (a) Example of a spectrum that is cleaned by the GANDALF software. The plot shows the original spectrum (black line) overplotted with the GANDALF-corrected clean spectrum (red line). The correction on the sulfur and Hα lines around 6500 Å are very prominent. Note that there is also a slight correction at 4850 Å and 4400 Å , which are Hβ and Hγ lines, these are tied to the Hα line since they originate from the same atom as thus this correction originates from Hα. The two corrections around 5000 Å are due to [OIII] emission.
(b) Example of a convolved spectrum. The red line shows the original spectrum with a velocity dispersion, σ, of 238 km s^{-1} and the blue line shows that spectrum convolved to σ = 350 km s^{-1}. Here you can also see an anomaly around λ ~ 5580 Å. This is telluric [OI] emission and coincides with the aTiO absorption line, making aTiO difficult to measure.

Table 3.2: List of used Lick/IDS indices

Index	Central band (Å)	Pseudo-continua (Å)	Main tracer	Note
bTiO	4758.500 - 4800.000	4742.750 - 4756.500 4827.875 - 4847.875	IMF and stellar temperature	[2]
Hβ	4847.875 - 4876.625	4827.875 - 4847.875 4876.625 - 4891.625	Age	[1]
Mg_b	5160.125 - 5192.625	5142.625 - 5161.375 5191.375 - 5206.375	[α/Fe] and Z	[1]
Fe5270	5245.650 - 5285.650	5233.150 - 5248.150 5285.650 - 5318.150	[α/Fe] and Z	[1]
Fe5335	5312.125 - 5352.125	5304.625 - 5315.875 5353.375 - 5363.375	[α/Fe] and Z	[1]
aTiO	5445.000 - 5600.000	5420.000 - 5442.000 5630.000 - 5655.000	IMF and stellar temperature	[2]
NaD	5878.625 - 5911.125	5862.375 - 5877.375 5923.875 - 5949.875	IMF and [Na/Fe]	[1]
TiO1	5938.375 - 5995.875	5818.375 - 5850.875 6040.375 - 6105.375	IMF	[1]
TiO2	6191.375 - 6273.875	6068.375 - 6143.375 6374.375 - 6416.875	IMF	[1]
CaH1	6357.500 - 6401.750	6342.125 - 6356.500 6408.500 - 6429.250	IMF and stellar temperature	[2]
CaH2	6775.000 - 6900.000	6510.000 - 6539.250 7017.000 - 7064.000	IMF	[2]

[1]: Worthey et al. (1994) [2]: Spiniello et al. (2014)

3.7 Stellar population parameters

We fit SSP models to our convolved and cleaned spectra. To investigate which SSPs are present within a spectrum, thereby finding the best-fitting stellar population parameters, we compare the spectra with the CvD12 SSP models. We do this by retrieving, via SPINDEX, the Equivalent Widths (EWs, Equations 1.6 and 1.7) of the indices from both the galaxies and the CvD12 models (convolved to the same 350 km s^{-1} resolution). As CvD12 has well defined stellar population parameters, we can determine the parameters of the galaxy spectrum by comparing its EWs with the EWs from CvD12.

The different stellar population parameters used in the SSP models to fit to our spectrum are[6]

- IMF-slope (x): [1.8, ..., 3.5] in steps of 0.1
- Age (t): [3.0, 5.0, 7.0, 9.0, 11.0, 13.5] Gyr
- metallicity (Z or [M/H]): [-0.6, ... , 0.2] dex in steps of 0.1
- [α/Fe]: [-0.2, ..., 0.4] dex in steps of 0.1
- [Na/Fe]: [-0.2, ..., 0.6] dex in steps of 0.1

[6]CvD12 can have a temperature-sensitive component as well, where the shift in giant-branch temperatures is measured.

CvD12 uses solar-metallicity isochrones when synthesizing models with different abundance patterns, where the total metallicity only varies between models because the abundance variations of single elements are implemented at fixed [Fe/H] (Conroy & van Dokkum, 2012a). In order to extend the CvD12 metallicities to the sub-solar values we describe above, we apply the metallicity-response function described in Spiniello et al. (2015), where they extend the parameter space by multiplying CvD12 models with the ratio of two MIUSCAT models (Vazdekis et al., 2012) with the same age and IMF slope, but with different metallicity.

Metallicity is defined as a fraction of the solar metallicity, $\log(\mathrm{Z}/\mathrm{Z}_{\odot})$, and α is the set of elements present in the α-ladder (atom number is a multiple of four). We compare the SSP EWs with those of the galaxy using χ^2-statistics. χ^2 is the deviation between the indices of the SSPs and those of the galaxy. Thus, the minimum χ^2 is the minimum deviation of the model from the spectrum: the model with χ^2_{min} is the best-fit model. To find the most likely value of an atmospheric parameter, we determine χ^2_{min} for each atmospheric parameter step and plot the [parameter, χ^2_{min}] plot and interpolate this to find the absolute minimum of the line. We also determine an upper and lower limit to this value based on a 1σ confidence interval.

We use a method similar to the one described in Spiniello et al. (2014). Here, for every galaxy spectrum the χ^2 with an SSP model is given by

$$\chi^2_n = \sum_{ind=1}^{m} \chi^2_{ind,n} = \sum_{ind=1}^{m} \frac{\left(EW^{obs}_{ind} - EW^{mod}_{ind,n}\right)^2}{\sigma^2_{EW^{obs}_{ind}}} \tag{3.8}$$

where n is the SSP model of interest and m is the number of indices measured with SPINDEX. Via the likelihood function $\mathrm{L} \propto \left(\exp - \chi^2/2\right)$ the probability density function is obtained, which we can marginalize over the individual stellar population parameters.

In addition to the χ^2 statistics, we can also create index-index plots to compare the sata with the models. Here we plot indices which are sensitive to a certain parameter and compare them with grids created by varying SP parameters of the model. This way we can determine to which parameter an index is sensitive to and if stellar population parameters correlate with each other. We apply this method in Chapter 4.1.

For our analysis we use the indices listed in Table 3.2. We also use the [MgFe] index, defined in González (1993) as

$$[\mathrm{MgFe}] = \left(\mathrm{Mg_b} \times \frac{\mathrm{Fe}_{5270} + \mathrm{Fe}_{5335}}{2}\right)^{1/2} \tag{3.9}$$

which is a tracer sensitive to metallicity and age, not to $[\alpha/\mathrm{Fe}]$, and is depending only weakly on velocity dispersion.

In this chapter we describe all the algorithms and methods used to extract absorption line indices, stellar kinematics, and stellar population parameters from a raw CALIFA data cube. In the following chapters we present our results on galaxies' kinematics, the EWs of the indices, and compare the results with the CvD12 SSP models. From these we try to find relations between indices, stellar population parameters and kinematics, as well as radial gradients of absorption lines and stellar population parameters.

4

Results

In this chapter we present the main results. We discuss what the extracted results of the Lick/IDS indices tell us by looking for relations between the indices as well as determining which indices influence the IMF, and other stellar population parameters, the most. We then discuss the CvD12 model-parameters. We look at how the parameters relate to each other and check for possible trends. We then examine the IMF-σ and IMF-[M/H] relations. We then investigate the radial trends of the parameters and indices within the individual galaxies. By looking at gradient plots, we aim at understanding how the physical parameters behave with respect to each other and with respect to centre distance. Our final purpose is to infer the possible merging history of the systems.

Throughout this chapter we compare results to previous studies before moving to a more general discussion in the next chapter.

4.1 The Lick/IDS indices

The purpose of this thesis is to investigate the slope and behaviour of the low-mass end of the IMF in ETGs. We start by looking at which indices are the most influenced by the IMF slope. We do this by comparing the intensity of different IMF-sensitive indices and check to which best-fit IMF slopes these intensities correspond, i.e. for which values of the stellar population parameters do the CvD12 models return the lowest χ^2 given the observed absorption line intensities.

We look at how the individual indices behave with respect to the velocity dispersion of their respective bins and whether there is evidence for radial trends. Since σ is expected to be radially declining, these two checks should show similar behaviour. We then determine the sensitivity of different stellar population parameters based on index-index plots between indices which are sensitive to different parameters.

4.1.1 Radial and kinematic trends

Both indices and kinematics follow directly from the algorithms explained in Chapter 3. We first check indices for possible radial and kinematic trends. We want to determine the radial gradient of the indices, which shows if indices vary with radius and by how much. After determining to which specific indices the stellar population parameters are sensitive we aim to predict how these parameters behave radially based on the indices.

We determine the trend of absorption line indices by measuring radial variations they show in the individual galaxies. We fit these variations with the **curve_fit** algorithm, as provided in the SciPy package, which returns the slope of the radial gradient. An overview of the radial trends of the indices, as well as σ, is presented in Figure 4.1. Here we show the gradients of the individual indices and σ of all 17 galaxies. A positive gradient implies a radial rise of intensity of the absorption line (or velocity dispersion), whereas negative values imply the opposite.

Most indices decrease over radius with the exception of Hβ, which is equally likely to rise or fall. Since Hβ is our main index for determining the stellar ages we expect the ages to follow the same trends as Hβ and thus to show similar radial ambiguity on a galaxy-by-galaxy basis. With the exception of NaD all IMF-sensitive indices are presented on the right-hand side of the plot. The intensities and gradients in these indices are small, underlining the difficulty of probing radial variations of IMF slopes.

Two galaxies are highlighted in Figure 4.1. First, the yellow points show one galaxy with a positive σ gradient, NGC6150. This gradient is a product of a high σ measurement in the outer radii; the inner three radii show a negative σ gradient. The outer radius in this galaxy is subject to telluric contamination that influences the pPXF output. If we exclude the outer bin in this galaxy the gradient is reduced to $\nabla\sigma/30$ = -0.82.

Second, the green points show the only galaxy with a positive gradient in magnesium, NGC6173. A radially rising magnesium strength in an ETG can imply a recent merger event. More evidence of this is present in the negative Hβ gradient of this galaxy which tells us young stars are dominant in the central region of this galaxy. This is assumed to be due to a recent (wet) merger where the cessation of star-formation occurs in an outside-in manner as the molecular gas is heated and consumed (more on this in Section 4.3). The positive gradient of the Fe 5335 Å line in this galaxy is due to telluric contamination in the outer bin, which also explains the positive gradient in [MgFe]. It does not, however, explain the Mg_b line.

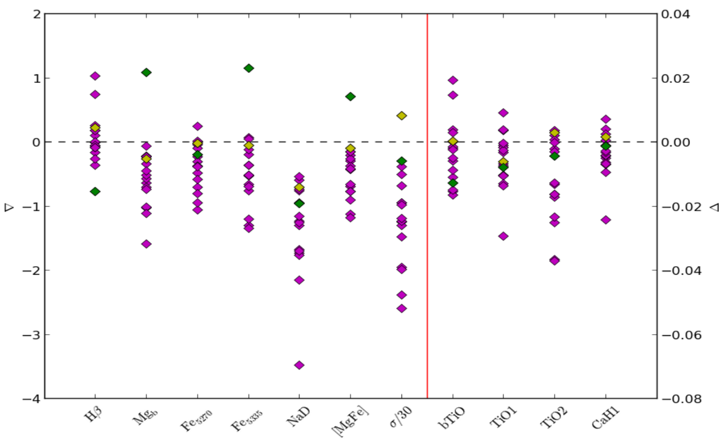

Figure 4.1: Radial gradients of the measured Lick/IDS indices and velocity dispersion. σ has been divided by 30 to fit the points in the plot. The black dashed line represents a flat (no) gradient. The vertical red line separates the IMF-sensitive indices (right side) from other indices and the velocity dispersion (left side). The gradients on the right side use the right-hand y-axis whereas the left side uses the left-hand y-axis. Two peculiar galaxies have been highlighter in yellow ($\nabla\sigma > 0$), which is NGC6150, and green (∇[MgFe] > 0, ∇ $Mg_b > 0$), which is NGC6173. These galaxies are discussed in the text.

4.1.2 Determining parameter-sensitive indices

We now determine the sensitivity of the indices to different stellar population parameters. Based on Table 3.2 we can make a qualitative guess as to what index influences what parameter; however the best-fit parameters are model-dependent. Therefore it is useful to determine to which indices the IMF is most sensitive in this particular set of SSP models. I refer the reader to Spiniello, Trager & Koopmans (2015) for a more detailed review on how the ingredients and underlying assumptions in SSP models influence the fitted parameters. For the purposes of this work it is sufficient to keep in mind that a different set of SSP models can give different results.

Figure 4.2 shows the model variations of CvD12 based on various IMF-sensitive features. After the χ^2 routine we have, for every spectrum, the five best-fit values of our set of stellar population parameters: IMF-slope (x), metallicity (Z or [M/H]), α-element abundance ([α/Fe]), age (t), sodium fraction ([Na/Fe]). Here a darker shade of red corresponds to a higher parameter value. We show that the indices which correlate (or anti-correlate) most strongly with the IMF parameter are the TiO2 and NaD lines, both showing a positive correlation with the slope of the IMF. The bTiO and CaH1 indices show an anti- and a positive correlation respectively with the IMF, although the correlation is weaker in both cases. TiO1 seems not to influence the IMF in the present SSP models.

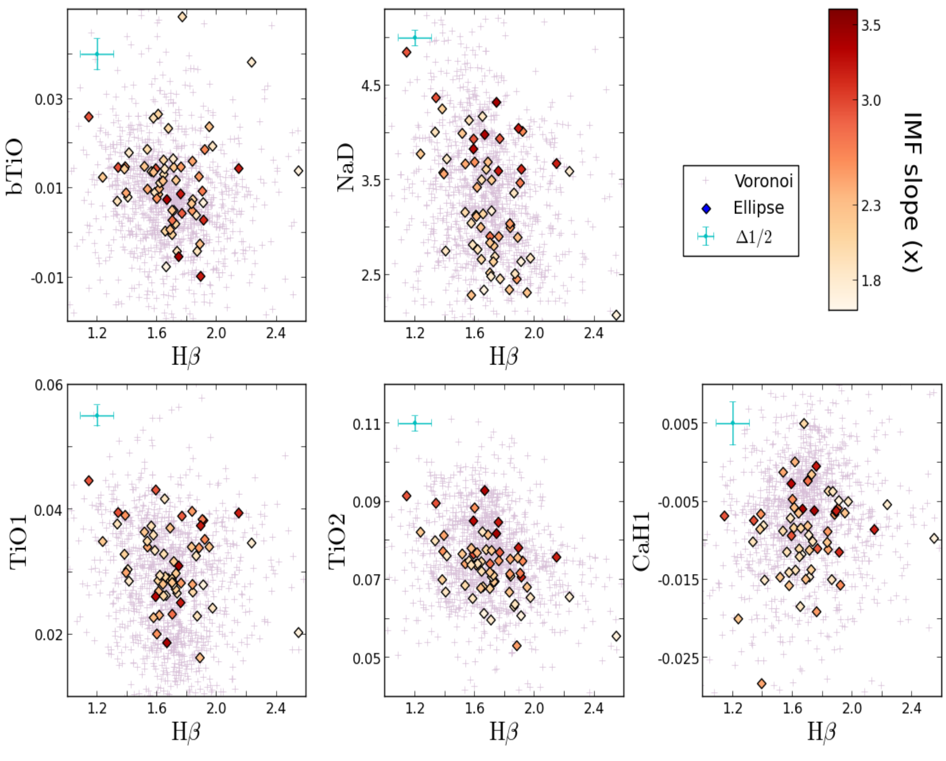

Figure 4.2: Index-index plot of the different IMF-sensitive indices versus the age-sensitive index Hβ. The diamonds show the value of the elliptical bins and the crosses show the values of the Voronoi bins. The colours of the diamonds show the best-fit IMF slope of the bin - where darker red means a more bottom-heavy IMF. The cyan crosses at the top-left show the median errors of the elliptical bins.

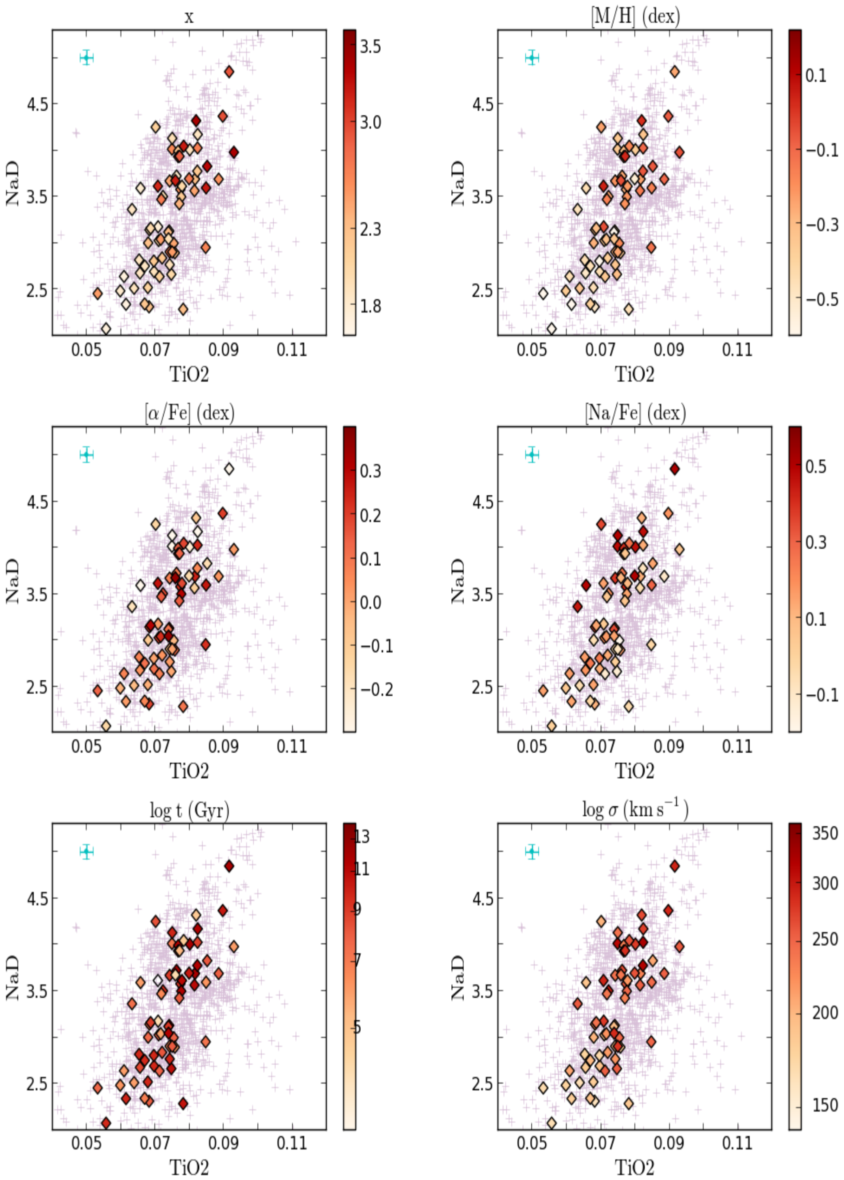

Figure 4.3: [TiO2,NaD] index plots colour-coded by parameters and velocity dispersion. The meaning of the symbols is as in Figure 4.2. The [M/H], σ, and [Na/Fe] have similar patterns as the IMF slope.

We check whether TiO2 and NaD have other correlations with other stellar population parameters and/or σ. Figure 4.3 shows the [TiO2, NaD] plots colour-coded with the other parameters. From Figure 4.3 it appears that metallicity ([M/H]) and σ show similar trends with these indices as the IMF, with these two parameters correlating positively with both these indices. The sodium fraction ([Na/Fe]) also correlates positively, although this is due to an interplay of the positive correlation between TiO2 and NaD, and the fact that [Na/Fe] depends predominantly on NaD alone.

The colour of the age parameter tells us that the stellar ages of the galaxies are relatively old (> 9 Gyr) with only a few younger elliptical bins. The set of younger bins is dominated by the inner radii of the systems, where 75% of bins with t < 6 Gyr are bins with 1/8 R_{eff}. The [α/Fe] parameter is independent of both TiO2 and NaD.

4.2 IMF relations

Figures 4.2 and 4.3 show similar patterns in the IMF slope, metallicity, and σ. This implies a relation between these three parameters. Studies have already reported both the IMF-Z relation (Martín-Navarro et al., 2015c) and the IMF-σ relation (e.g. Conroy & van Dokkum 2012b; Cappellari et al. 2013; La Barbera et al. 2013; Spiniello et al. 2014). We show our findings below and compare them with previous results.

4.2.1 IMF-σ relation

The relation between IMF and velocity dispersion has been intensively studied in the past few years. Among others Treu et al. (2010); La Barbera et al. (2013) and Spiniello et al. (2014) have reported a positive relation between the low-mass IMF slope and σ. A higher velocity dispersion leads to more turbulation and to larger density fluctuations in the ISM which promotes fragmentation over a broader range of masses. Since high-mass stars only form in clouds which are heavy enough to support their formation, this broad fragmentation steepens the IMF as well as lowers the low-mass turnover (Hopkins, 2013).

Multiple IMF-σ relations have been reported. Spiniello et al. (2014), henceforth S14, reported a linear relation between the two parameters by comparing IMF-sensitive indices of the MILES stellar library all convolved to the same velocity dispersion. They reported that, if the NaD absorption line is included in the analysis, a fit between the two parameters yields

$$x = (2.13 \pm 0.15) + (2.3 \pm 0.1) \log \sigma_{200} \tag{4.1}$$

where σ_{200} is the velocity dispersion measured in units of 200 km s^{-1}. This slope becomes shallower if the sodium lines are not included in the analysis.

As presented in Figure 4.4, the S14 relation agrees roughly with our values, but the scatter in the points is too large, especially in the high-σ region, to safely confirm the relation. This leads to the suspicion that metallicity is a more fundamental driver behind the IMF variations and that the IMF-σ relation is only a direct consequence of the well-established [M/H]-σ relation (e.g. Tremonti et al. 2004).

A positive relation between IMF and σ is not only reported in spectroscopic studies, but also in dynamical studies like Treu et al. (2010) and Cappellari et al. (2013). Smith (2014) compared two different IMF studies, one dynamical (Cappellari et al., 2013) and one spectroscopic (Conroy & van Dokkum, 2012b). These two studies have in their sample a set of 34 galaxies in common. Smith compared the conclusions that are reported in these studies and determined how these studies differ on a galaxy-by-galaxy basis. He defined the IMF mismatch parameter as $\alpha = \Upsilon/\Upsilon_{\mathrm{ref}}$, the ratio of mass-to-light ratios, where Υ_{ref} is set to the Milky Way value.

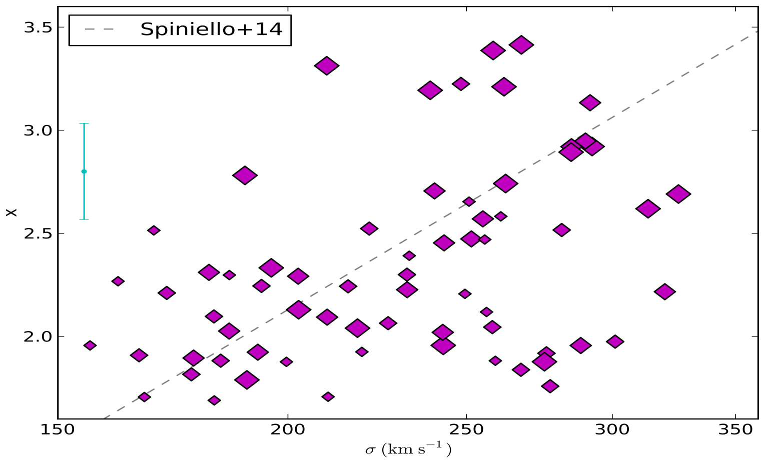

Figure 4.4: IMF-σ relation of the elliptical bins. The size of the diamonds indicates the fraction of the effective radius of the elliptical annuli. The size of the diamonds decreases with radial distance from the centre and thus annotate bins with a higher S/N. The cyan line represents the median uncertainties of the best-fit IMF. The grey dashed line shows the relation of Equation (4.1) as derived in Spiniello et al. (2014).

On a galaxy-by-galaxy basis the two methods show no similarities, but Smith noted that globally the results do show similarities. Both studies report a positive correlation between α and the velocity dispersion, meaning that steeper IMFs are present in high σ galaxies. Furthermore, the spectroscopic method yields a positive correlation between IMF and [Mg/Fe], a feature not reported in the dynamical study. A skeptical view is that some confounding factor has not been properly accounted for and that, depending on either a spectroscopic or dynamical approach, the IMF can depend solely on absorption line abundances or on σ alone respectively. An optimistic view on this discrepancy is that both methods measure different aspects of the IMF, where the spectroscopic method leans on the mass-to-light ratio and the dynamical method leans on total mass.

In recent work Lyubenova et al. (2016) reported that there can be a consistency between the IMF of the dynamical and the spectroscopic method. Using CALIFA data they report that by using a bimodal (broken power-law) IMF, both methods lead to similar results. The single power-law IMF, however, does show a discrepancy. A unimodal power-law produces stellar masses that are larger than the dynamical masses. Being that this result is unphysical they report that the unimodal IMF can be excluded.

La Barbera, Ferreras & Vazdekis (2015) studied the [Mg/Fe]-σ relation using a large sample of SDSS spectra and concluded that the IMF does not show a tight relation with [Mg/Fe]. Furthermore, Martín-Navarro et al. (2015a,b) reported that σ is not the main driver behind the dwarf-to-giant ratio in several resolved galaxy spectra and that the IMF-σ relation is more prominent in unresolved data. They proposed that IMF gradients in resolved ETG spectra can be accounted for by the radial gradient in metallicity.

In Figure 4.5 we show the relations of $\mathrm{Mg_b}/\langle\mathrm{Fe}\rangle$[1] with both IMF-slope and σ. As in the studies above, we find no correlation between either of these parameters as expected in our resolved spectra. Thus we underline that the relation between IMF, $\mathrm{Mg_b}/\langle\mathrm{Fe}\rangle$ and σ in our data are uncorrelated (Figure 4.5) or

[1] We have not determined the [Mg/Fe] parameter, which is a parameter which depends on $\mathrm{Mg_b}$ and $\langle\mathrm{Fe}\rangle$, but also has an age and metallicity dependency. We use $\mathrm{Mg_b}/\langle\mathrm{Fe}\rangle$ as a near estimate for [Mg/Fe]

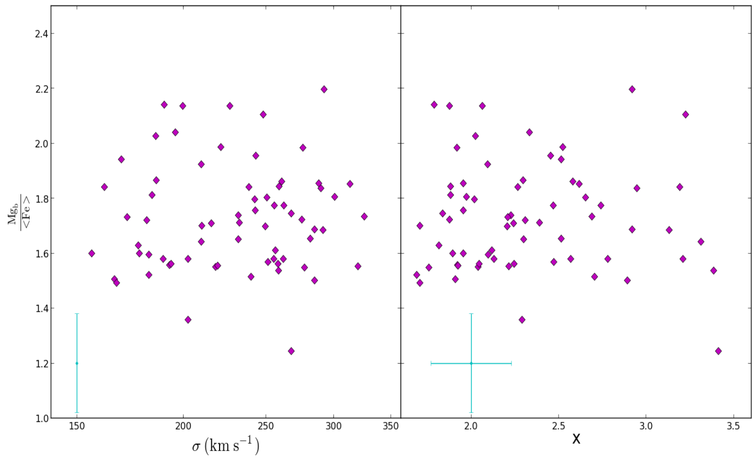

Figure 4.5: The $\mathrm{Mg_b}/\langle\mathrm{Fe}\rangle$ versus both σ (left panel) and IMF slope (right panel). IMF slope is expected to have a positive correlation with σ (Spiniello et al., 2014) and σ to have a positive correlation with [Mg/Fe] (Conroy & van Dokkum, 2012b). We find neither of these relations. In fact, $\mathrm{Mg_b}/\langle\mathrm{Fe}\rangle$ appears to be invariant to these parameters. The IMF-σ relation is reported to be more loose in resolved stellar populations (Martín-Navarro et al., 2015a,b) which explains our loose relation as well. The lack of relation between $\mathrm{Mg_b}/\langle\mathrm{Fe}\rangle$ and both IMF and σ can be explained by the lack of range in σ. We discuss this further in Chapter 5.

loosely (Figure 4.4) at best.

4.2.2 IMF-metallicity relation

The IMF-[M/H] plot is shown in Figure 4.6. The points show a positive linear relation between the parameters. This confirms the earlier study done by Martín-Navarro et al. (2015c), henceforth MN15, which reported a linear trend between IMF and metallicity. Similar to us they use CALIFA data in elliptical bins, albeit with different galaxies and by varying the high-mass end of a broken powerlaw instead of varying the lower-mass end and using a unimodal IMF. MN15 reported a best-fit linear IMF-[M/H] relation of the form

$$x = 3.2(\pm 0.1) + 3.1(\pm 0.5) \times [M/H] \tag{4.2}$$

We find a good agreement between our results and MN15 when we plot this relation over our data points. From this relation MN15 proposed that the previously discussed IMF-σ relation is due to a combination of the σ-[M/H] relation and the IMF-[M/H] relation of Equation (4.2). MN15 reported an IMF which grows more top-heavy with decreasing metallicity, meaning that higher metallicities result in fewer high-mass stars. Based on Figure 4.6 we report that the low-mass IMF slope is steeper with increasing metallicity, meaning that higher metallicities result in more low-mass stars. These two results show a consistent conclusion: the fraction of low-mass to high-mass stars grows with increasing metallicity regardless of which portion of the IMF you choose to investigate.

If metallicity is the main driver behind the IMF-slope, we can shed some new light on both the formation history of galaxies as well as on the Star-Formation Histories (SFHs) of the systems. Since metallicity is mainly regulated through stellar nucleosynthesis (Leitherer, Robert & Drissen, 1992) the SFH and IMF play an important role in this parameter. The SFH, however, heavily depends on the formation history of galaxies. Monolithic collapse and hierarchical growth predict different SFHs. Monolithic collapse predicts star formation at high redshift only. Hierarchical formation has a continuous rate of star

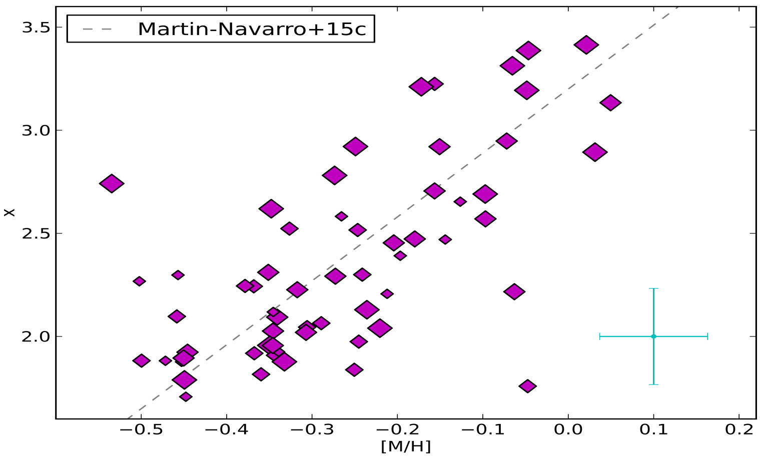

Figure 4.6: IMF-[M/H] relation of the elliptical bins. The size of the diamonds indicates the fraction of the effective radius of the elliptical annuli. The size of the diamonds decreases with radial distance from the centre. The cyan cross represents the median errors of the parameters. The grey dashed line shows the linear-relation of Equation (4.2) as derived in Martín-Navarro et al. (2015c).

formation in lighter systems. The star formation shift towards the earlier epochs for massive ($\geq 10^{12}$ $M_{\odot}$) galaxies, making the SFH similar to the monolithic collapse hypotheses (Trager & Somerville, 2009; Arrigoni et al., 2010). Different formation models predict star formation at different radii of the galaxy and therefore predict different radial variations in metallicity. Here, the merging history of galaxies plays a role, with relative quiescent galaxies showing steeper radial metallicity gradients than galaxies with lots of (major) mergers (Kobayashi, 2004).

4.3 Parameter gradients

Figure 4.6 shows that the top-right corner of the plot is populated with the inner radii of a number of galaxies, meaning that in these galaxies the IMF decreases radially. There are, however, also central points in the lower-IMF regions of the diagram, meaning that a radially declining IMF is not present in all galaxies. Because the IMF is not consistent, the IMF is related with [M/H], and the galaxy formation process plays a prominent role in the [M/H] gradient, we continue to look at the individual gradients that galaxies show in [M/H] and IMF-slope and determine what the parameters tell us about the formation history of these galaxies. We determine the gradient (∇) that a certain parameter shows as a function of radius. Since the individual values of IMF and metallicity follow a positive linear trend, we suspect to find the gradients of these parameters to be either both positive or both negative. A positive gradient means that between the central bin and the outer bin the value of the parameter rises, whereas a negative gradient means the opposite. We find the gradient with the Scipy **curve_fit** routine.

4.3.1 Metallicity gradients

The metallicity gradient is a good place to start not only because of its correlation with the IMF, but also because it is often used to study the formation histories of ETGs. The monolithic collapse model predicts steep metallicity gradients with metal-rich centres (where the metallicity increases through stellar nucleosynthesis) whereas the hierarchical formation models predict shallower gradients due to dilution of line-strength gradients existing in the pre-merger systems. However, adding secondary star-formation via (wet) mergers will lead, again, to enhanced metallicities in the inner regions due to cessation of star-formation in the outer radii, and thereby, again, steepening the gradient (Kobayashi, 2004; Kuntschner et al., 2010).

Kobayashi (2004), hereafter K04, investigated the metallicity gradients in ETGs by comparing the gradients of numerical models with various merging histories versus empirical gradients. She reported that in the case of monolithic collapse the models show a strong radial gradient in metallicity but that these steep gradients can be destroyed by mergers. Major mergers ($M_2 > 0.2\ M_1$) will force metal-rich stars to migrate to the outer regions of the galaxy, flattening the metallicity gradient. The rate of change in the gradient is dependent on the mass-ratio between the pre-merger galaxies and the gas-fraction of the infalling galaxy. Non-major mergers can induce star formation in different parts of the primary galaxy. If the ratio of the (gas) mass is large ($M_{gas,2}/M_{gas,1} \geq 0.5$), star-formation will be induced at the centre of the primary galaxy and the change in the gradient is limited. But sometimes, if the merging event is very wet ($M_{gas,2} > 0.5\ M_{total,2}$), the infalling galaxy behaves like a gas cloud and moderate star formation can be induced in the outer regions, causing the gradient to become shallower.

Our inferred ∇IMF-∇[M/H] relation is presented in Figure 4.7. We show that the IMF-[M/H] relation does not limit itself to local regions within the galaxy alone as the individual radial trends also show a correlation. The IMF gradients and metallicity gradients are either both positive or both negative and the general relation appears linear. This means that the IMF and [M/H] can indeed be a local value which varies depending on where in the galaxy you look but that the radial trends of the two parameters are also not uncorrelated.

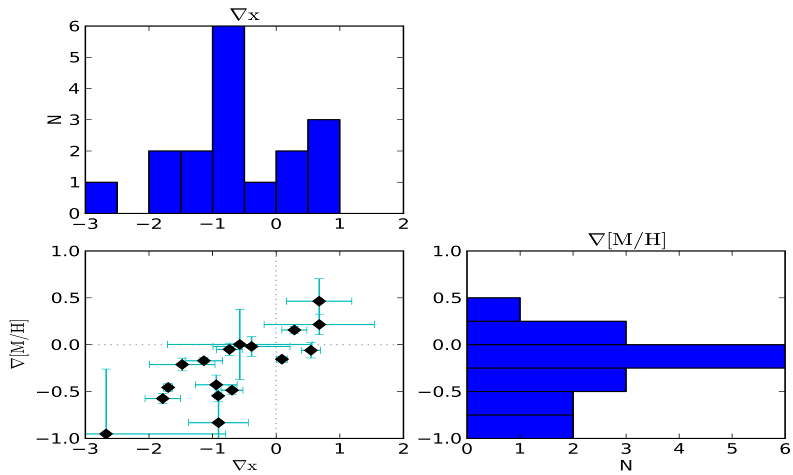

Figure 4.7: The relation between the gradient of the IMF-slope and the gradient of the metallicity. Each diamond represents the gradient of one galaxy. The gradients show a positive trend, meaning the IMF-[M/H] relation exceeds the parameter-parameter space and is also present in the individual gradients. The dotted lines are to guide the eyes at the null values (no radial variation). The histograms show the number of galaxies within bins of a certain gradient range.

The number of data-points we have for Figure 4.7 is 17. Therefore it is difficult to make definite statements about possible correlations between the gradients. We can, however, make claims based on statistics. Figure 4.7 shows a positive correlation between the IMF and metallicity gradients. To determine whether there is an actual positive trend we calculate the Spearman ranked correlation coefficient (ρ) for these points. ρ assesses how well two variables can be described by a monotonic function. A ρ of unity (or minus unity) means there is a perfect monotonic increasing (or decreasing) trend which described the relation of the two variables. No relation returns $\rho = 0$.

The Spearman value in the [∇IMF, ∇[M/H]]-space is $\rho = 0.81 \pm 0.16$. This value means that the relation between the two parameters is likely to be monotonically rising. The correlation between the two parameters suggests a strong bond between the metallicity of a given region and the IMF slope in the same region. The fact that most galaxies are decreasing in both values tells us that the IMF slope tends to be steeper in a galaxy's centre and that a galaxy is most metal enriched in regions where the IMF slope is more bottom-heavy.

We look at the relation between these gradients and the possible merging histories of the galaxies, comparing our work to the work of K04. She reported that the initial metallicity-gradient in ETGs at $z > 3$ is in the range -1.5 – -1. These values are steeper than our observed gradients, but our galaxies have redshifts of $z \leq 0.03$ and are far past their initial star formation phase and underwent several mergers since their initial formation.

K04 determined that with larger mergers the gradient becomes shallower. In fact, typical gradients of post non-major mergers and post major mergers are -0.3 and -0.22 respectively. Drawing a hypothetical line at ∇[M/H] = -0.3 we see that 7 of our galaxies are below this value so these galaxies are most likely the product of non-major mergers. The fact that a steeper metallicity gradient coincides with steeper IMF-gradients shows that the IMF-gradient is equally dependent on the merging history of galaxies. Steeper metallicity gradients imply non-major mergers in which the star-formation ceases outside-in, meaning star formation is more prominent in the central regions of the galaxy. And since the metallicity in the central regions is high, and the IMF-metallicity relation holds, the IMF will steepen near the galactic centre and remain stable in the outer regions.

The opposite is true for galaxies above ∇[M/H] = -0.22, where major mergers destroy the metallicity gradients and, consequentially, the IMF gradients. In these events the effect of a merger is not limited to the outer regions of the galaxy but instead penetrates the complete galaxy, forcing metal-rich stars to migrate outwards, thereby steepening the IMF-slope in the outer regions (Kobayashi, 2004). This leads to a flattening in both gradients.

4.3.2 Other parameter gradients

Given the IMF-metallicity relation suggested by MN15, the fact that we find a relation in their respective gradients might not be too surprising. Therefore we shift our attention to the behaviour of the other gradients and see if these can help to further constrain the merging history of galaxies.

Comparing the IMF slope with the [α/Fe], age, and [Na/Fe] parameters does not show any clear behaviour in the parameter space (Figure 4.3, left half of Figure 4.8). The radial gradients, however, seem to show correlation for the individual galaxies in both the [Na/Fe] and age spaces. Figure 4.8 shows the relation between the stellar population parameters [α/Fe], [Na/Fe], and age versus IMF slope in both parameter (left) and gradient space (right).

The upper left (right) panels show the IMF slope (gradient) versus the [α/Fe] abundance (gradient). The [α/Fe] abundance is the parameter that depends least on the others: in both parameter and gradient spaces there is no correlation with the IMF values. Since both α-elements and Fe mainly originate from stellar nucleosynthesis (supernovae type II and type Ia respectively) these plots can be used to infer the occurrences of these events in the different systems. Based on the parameter plot [α/Fe] is independent of IMF slope. In the gradient plot we see similar behaviour. [α/Fe] is equally likely to rise or fall radially. This shows that there is no clear relation between [α/Fe] and IMF slope. Therefore, a direct sensitivity between [α/Fe] and the merging history based on these plots is not seen. Since [α/Fe] is used as a tracer for star-formation efficiency, the lack of relation between this parameter and the IMF is surprising. The [α/Fe] relations are discussed in more detail in Section 5.3. The Spearman coefficients are $\rho = 0.27 \pm 0.16$ for the gradients and $\rho = 0.16 \pm 0.08$ for the parameters.

Sodium is not part of the α-ladder and mainly originates from gas stripped from ~8-9 $M_\odot$ stars. Since NaD is both an IMF-sensitive index and the main contributor to the [Na/Fe] parameter, we expect a tighter relation in the IMF-[Na/Fe] plots than the one we find in the IMF-[α/Fe] plots. Based on Figure 4.8 there is no evident correlation between these parameters. The gradients of these two parameters, however do show a negative trend: a positive IMF gradient corresponds to a negative [Na/Fe] gradient and vice versa. This trend does not go through (0,0), meaning there is a transitional area where both gradients can be negative. Spiniello et al. (2014) reported that the inferred IMF slope is highly sensitive to the NaD line; the difference in the IMF slope calculated for the same spectrum including or excluding the NaD line can be as high as 0.3. [Na/Fe] has a big impact on the IMF slope as well. We conclude that the sodium abundance cannot be ignored when constraining the IMF slope from galaxy spectra.

A radially rising IMF gradient implies a radially declining sodium fraction. Since NaD itself correlates positively with IMF, the Fe abundance is causing this decline, meaning that with a raising IMF the iron abundance increases more rapidly than the sodium abundance. This behaviour can be expected in older stellar populations in which SNIa events have enough time to enrich the iron abundance in the population. The Spearman coefficient is $\rho = -0.80 \pm 0.16$ for the gradients and $\rho = -0.09 \pm 0.08$ for the parameters.

The IMF–log t plot (Figure 4.8, left lower panel) show a flat distribution with a slight preference for younger stellar populations in the steeper IMF bins. A slight inverse correlation seems to be present between these parameters. In the gradient space (bottom right panel) can be seen, like the [Na/Fe] parameter, a slight inverse correlation between the age and IMF slopes. Although the age gradients are positive for the majority of the galaxies in our sample there are three galaxies with steep negative gradients. These galaxies have had no star formation in their centres for several Gyr and are expected to be more or less quiescent during that time. The steepest positive age gradient correspond to the steepest negative IMF gradient. This shows that stellar populations which grow radially older will decline radially in dwarf-star fraction. This hints towards a two-phased IMF slope where the initial star-formation event is more metal-poor and thus more top-heavy, creating stars in the high-mass range which die quickly and inject the ISM with metals. Later star-forming events will then fill up the lower stellar-mass ranges due to the higher metallicities of the ISM creating a more bottom-heavy IMF (see also Section 5.5). K04 suggests that major mergers flatten the metallicity gradient and that non-major mergers cease the star formation outside in. We report here that steeper IMFs correspond to steeper age gradients (where the age of the population is older on the outside) which is the product of an outside-in cessation of star formation. Therefore we conclude that galaxies in the top-left quadrant in the IMF–log t gradient plot can be the product of non-major mergers. Major mergers, on the other hand, flatten the IMF gradients and this seems to coincide with the flattening of the age gradient. The Spearman coefficient is $\rho = -0.68 \pm 0.16$ for the gradients and $\rho = -0.41 \pm 0.08$ for the parameters.

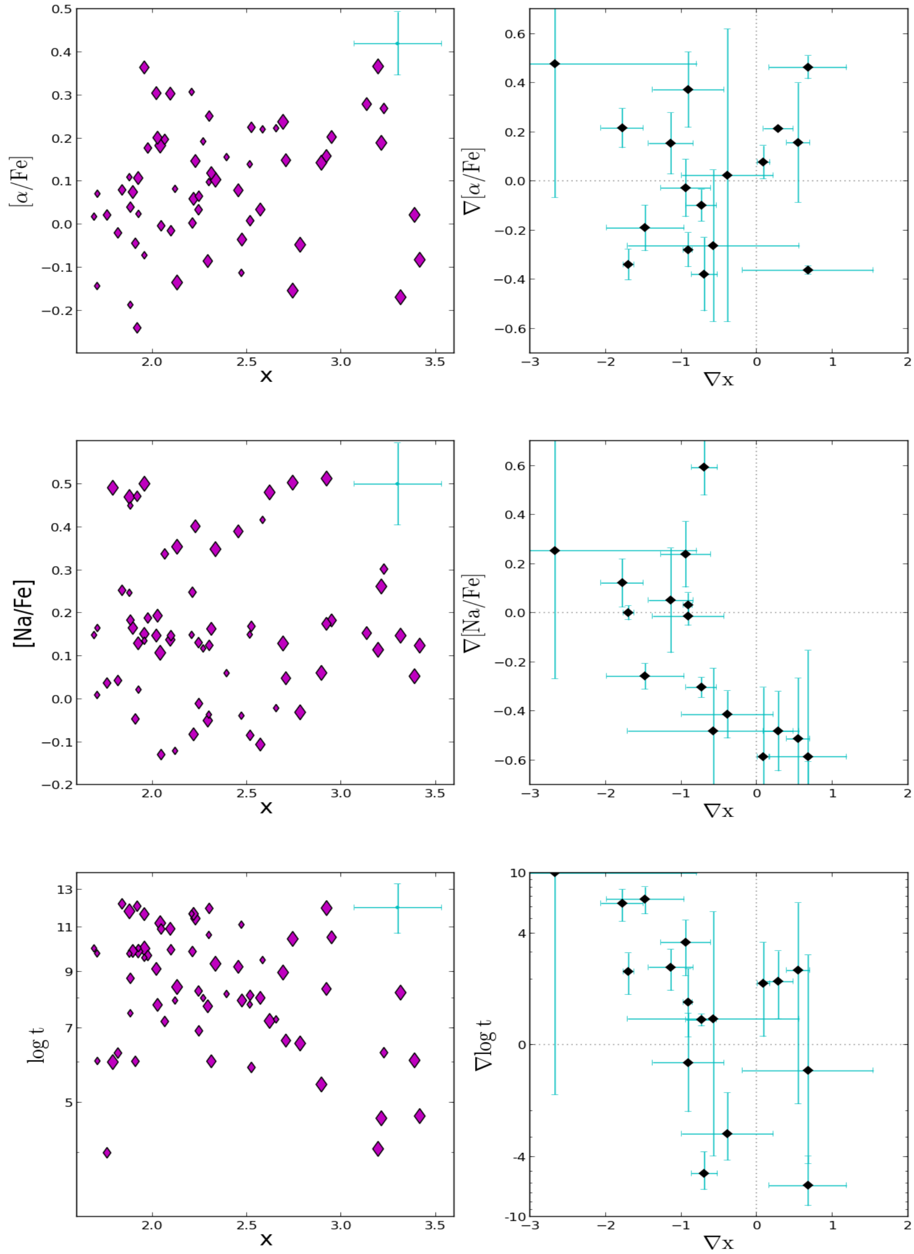

Figure 4.8: Plots of [IMF, [α/Fe]], [IMF, [Na/Fe]] and [IMF, log t] in both parameter (left) and gradient (right) space. The [α/Fe]-plots show no clear pattern in either of the plots and is therefore not assumed to be a major factor in the IMF shape. The middle two plots show the [IMF, [Na/Fe]] plots. These show no relation in paramter-space, but they seem to have a trend in gradient-space. The bottom two plots show the [IMF, log t] plots. As with [Na/Fe], there is no clear relation in the paramter space itself. In the gradient space a tentative negative correlation can be seen.

4.3.3 Mean radial trends in galaxies

Finally we compare these results with the results from Kuntschner et al. (2010), hereafter K10. They investigated radial trends in age, [M/H], and [α/Fe] in 48 different ETGs. We plot in Figure 9 a similar image as Figure 11 in K10, where the radial profiles of the galaxies are plotted, colour-coded by the age-value of the innermost bin. We add to this the median of the galaxies for every parameter value per radial bin to examine if there is, on a global scale, a general trend in the parameters.

The aim of K10 was to say something about both the individual radial trends as well as a median radial trend in ETGs. Their main results were (1) if the central part of the galaxy is old (> 9 Gyr) the age-gradients remain flat. (2) If the ETG is young in the centre, the age will increase towards the outer annuli. (3) Metallicities decline rather homogeneously with an average gradient of -0.28 dex. (4) Abundance ratios are typically flat or slightly rising with radius.

For all statements except (4) we find similar results: (1) age-gradients remain constant if the population is old in the centre, whereas (2) galaxies with younger SSPs in their centres show a radial aging in stellar population. (3) Metallicities decline (at least on average) with a constant radial gradient, where we find a mean gradient of -0.21 dex within the effective radius. Due to the scatter in our [α/Fe] parameter it is difficult to conclude something definitive like result (4). The median gradient is constant at $R_{\rm eff} \geq 0.25$ but in the inner bin the scatter in this parameter is high and contain several outliers. In Chapter 5.3 we discuss this further and speculate that we *do* find results consistent with argument (4).

K10 did not talk about the possible consequences that these gradients have on the IMF. Based on Figures 4.7 and 4.9 we see that the IMF shows similar patterns as the metallicity in both parameter and gradient space. We find a declining IMF profile with a slope steeper than Salpeter in the innermost bin which grows shallower in the outer regions. This is also consistent with the MN15 results. Furthermore, K04 reports that the metallicity-gradient depends on the merging history of galaxies. This means the IMF will vary radially within galaxies and between galaxies based on the different merging histories.

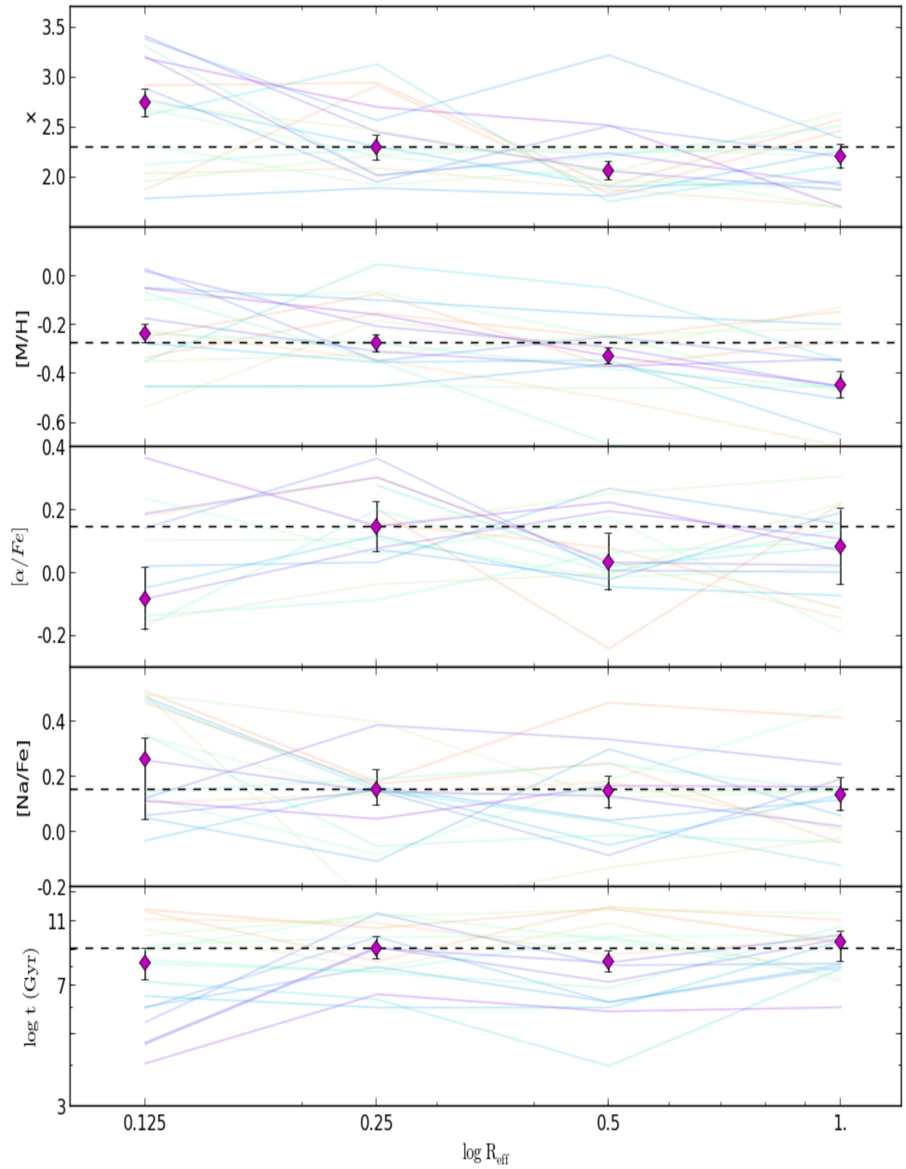

Figure 4.9: Figure showing the mean radial variation of the SSP paramters in the 17 galaxes. The purple diamonds represent the median value of the atmospheric parameter per fraction of the effective radius. The black dashed lines are to guide the eye to the level of the $R_{eff}/4$ value. The coloured, translucent lines are the individual galaxies, colour-coded based on the age of their inner annuli (with violet being young centres and red being old centres).

5

Discussion

We begin by discussing the main results. We then highlight some limitations of the data. We will quantify the uncertainties on the indices and the parameters, we will focus on model dependencies of results and we will describe some relations we found between the stellar population parameters that were not expected, nor reported in the literature. Finally, having these limitations in mind and understanding their implications on the results, we draw our final conclusions. Moreover, we analyse IMF and galaxy formation studies that have not yet been highlighted in the previous chapters and discuss possible future work and progress in the field.

5.1 Summary of the results

In this paragraph we summarize the main results of our research. We discuss the radial variation of the individual indices as well as the relation between the indices. We conclude that, with few exceptions, the radial trends are negative in both the indices and σ. We determine that the most IMF-sensitive indices are, in accord to the SSP models we use, NaD and TiO2, which are both correlating positively with the low-mass end slope of the IMF.

We find hints for a linear IMF-σ relation, similar to Spiniello et al. (2014), but we note that scatter is large and the trend could be artificial. In fact, Martín-Navarro et al. (2015a) reported that σ is not a main IMF driver, nor is this relation found in resolved spectra. We question the IMF-[Mg/Fe] relation, agreeing with La Barbera, Ferreras & Vazdekis (2015), although using a different set of SSP models and a different functional form of the IMF. We confirm the Martín-Navarro et al. (2015c) IMF-metallicity relation.

We look at the radial gradients of stellar population parameters within the individual galaxies. We determine that IMF and [M/H] show a correlation in both parameter and gradient space. We also use the work of Kobayashi (2004) to speculate about the merging history of galaxies based on these gradients, where we hypothesize that steeper gradients in IMF and metallicity are the result of non-major mergers, whereas flatter gradients are the results of major mergers. Based on the trends of the three other SSP parameters we show that [α/Fe] is independent of the other gradients and is unaffected by merging histories, and that the [Na/Fe] and age gradients show a negative correlation with both the IMF and metallicity gradients. When stellar ages are younger in the centre it means that star-formation in the outer regions is less efficient. We conclude this is due to non-major mergers. Shallower age-gradients are expected after major mergers. Our data shows a relative equal distribution between major and non-major merger galaxies: 7 out of 17 galaxies originate from non-major mergers based on their steep metallicity gradients.

Finally, we briefly compare our results with Kuntschner et al. (2010), who also studied radial gradients in several stellar population parameters. In three out of four key points regarding the age and metallicity gradients our results agree with their study. We confirm that (1) galaxies with old centres have a flat age gradient, (2) galaxies with young centres grow radially older and (3) metallicities radially decrease with a homogeneous average gradient, where Kuntschner reports a radial variation of -0.28 dex and we find -0.21 dex. Argument (4) is based on the [α/Fe] gradients and is an argument we cannot confirm. We elaborate on [α/Fe] in Chapter 5.3.

5.2 Uncertainties and contamination

The sources of uncertainties considered in this thesis are threefold: i) flux uncertainties from the CALIFA datacubes, ii) uncertainties of the line-index strength measurements computed by SPINDEX, and iii) uncertainties on stellar population parameters inferred via the χ^2 analysis.

First we look at the individual indices. In case of the elliptical bins, 25 lines (out of the 603 total) have a high uncertainty (> 2 times the median uncertainty of an index) after the smoothing procedure. This excludes the already discarded aTiO index (due to [OI] telluric contamination) and the CaH2 index (which has a blue pseudo-continuum that overlaps with an emission line at 7200 Å, possibly an OH line). Individually these lines will not affect conclusions drawn from the index parameters. The uncertainties, however, will be propagated into the parameter determination and from there propagate into the gradients.

In Appendix B we plot all of the indices in all of the elliptical bins, where the indices of the inter-galaxy bins are normalized and overplotted. From these plots it is evident that most of the indices that are extreme outliers are contaminated in their spectrum. This can be due to contamination from (telluric) emission lines (e.g. TiO2 and CaH1 in NGC6411), inadequate masking by GANDALF (e.g. Hβ in NGC6338) or due to bad-pixel regions in the CALIFA datacube which we masked inadequately. Discarded indices are written in cursive numbers.

All outliers, with the exception of 5 bTiO lines, can be explained with the three arguments above. The unexplained bTiO lines show relatively large uncertainties despite there not being an evident reason for it. For example, all bTiO lines in NGC5966 show large uncertainties, yet their spectra look normal as do their respective error-layers in the original data-cube. We note, however, that the measured bTiO values in this galaxy are negative. This is outside the bTiO range of the CvD12 SSP models, which do not go into the negative values for bTiO. This means that the bTiO values are unusual in these systems and this might explain the large uncertainties. Here the large uncertainties might work in our favour, since the SSP models will be fit on an index-by-index basis and a large uncertainty in values outside the parameter-range will give us smaller uncertainties in the best-fit SSP parameters as the error-bar will most likely fall into the parameter range. Small uncertainties, on the other hand, will force the SSP models to stay as near as possible to these bTiO values, thereby overcompensating in the other indices and creating larger uncertainties in the SSP parameter determination (see also Section 5.3).

Finally one note on the uncertainty in the age parameter, which depends solely on Hβ. Large uncertainties in this index will propagate directly through to the stellar ages. In general the uncertainties in the age-parameter are in the order of 1-2 Gyr. These values are large, but not unexpected given that other studies who use solely Hβ as a probe for stellar age find similar uncertainties (e.g. Kuntschner et al. 2010; Greene et al. 2015). In fact, Trager et al. (2000b) reported that contamination in Hβ by non-main sequence stars can cause small reductions of the inferred stellar age by at most 15% in the oldest stellar populations. Serra & Trager (2007) stated that a Balmer-line weighted age is biased towards the younger stellar populations and produce younger stellar ages than dervied from luminosity-weighted ages. Therefore, the SSP ages should not be interpreted as time passed since star formation but rather as an indication to the absolute age differences between different spectra. Greene et al. (2015) interpreted these uncertainties as a reason to take the results in ages with some restraint. We approach age in a similar way and do not use it to draw definite conclusions, but only as support to conclusions based on the other parameters.

5.3 Mg_b uncertainties

Our analysis revealed a systematic tendency of the [Na/Fe] parameter to cluster around [Na/Fe] = 0.15. The SSP models had trouble fitting this parameter and ended up pegging at this value (see top of Figure 5.1).The χ^2 values at [Na/Fe] = 0.3 are very high in these spectra and since the best-fit SSP model is determined by interpolation of the minimum χ^2 value in every parameter bin, the best-fit is set between [Na/Fe] = 0.1 - 0.2 due to the steep decline in χ^2 between 0.2 - 0.3.

The problem of the χ^2 determination in the [Na/Fe] = 0.15 spectra originates from the Mg_b index: specifically, the problem is in the extremely small χ^2 values resulting from the small uncertainties in this index. The uncertainties on the Mg_b index are much smaller (<0.5), than the ones on other indices. Consequently, Mg_b has a strong weight in our χ^2 analysis: the small errorbars force the SSP model to fit the Mg_b, overcompensating the fit on the other indices.

Therefore we redefine the Mg_b errors to give the models more freedom in fitting this index. To redefine the magnesium uncertainties we first determine the best-fit model while excluding the Mg_b line from the process. From this best-fit model we extract the Mg_b value and redefine the uncertainty in magnesium to be the standard deviation between the measured and best-fit Mg_b values. With this method, the uncertainties on the Mg_b index result to be a factor 2-5 higher, and the region around [Na/Fe] = 0.15 results less populated. In fact, a smoother transition between lower and higher values for the [Na/Fe] abundance are visible from the lower panel of Figure 5.1, where the correction have been applied to the data. We cannot say for certain that a preference for [Na/Fe] = 0.15 is completely gone, but as seen in Figure 5.1, it is not obvious anymore and the plot looks more natural. This adjustment does not significantly affect the other parameters.

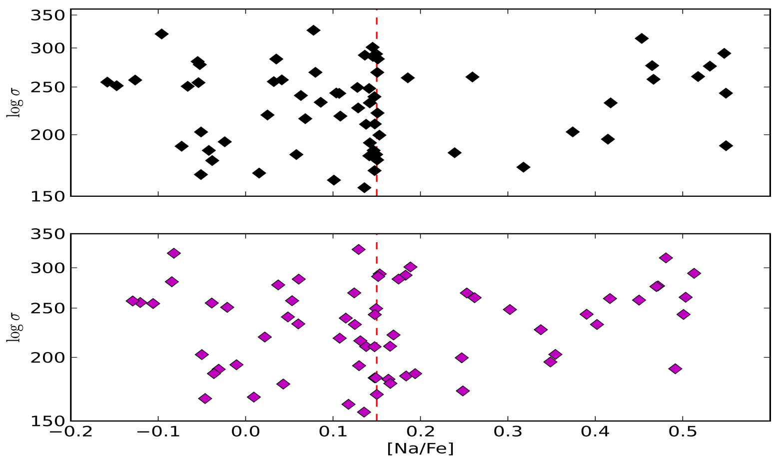

Figure 5.1: Inferred [Na/Fe] abundances before (up) and after (bottom) enhancement of the error in magnesium. In the top plot an artificial clustering around 0.15 can be seen. In the bottom plot the pegging is gone after the adjustment of the Mg_b uncertainties.

5.4 [α/Fe] versus other proposed IMF-parameters

Conroy & van Dokkum (2012b) reported a positive correlation between the IMF slope and stellar velocity dispersion (σ) as well as between the IMF slope and the [Mg/Fe] abundance ratio. We already touched on this topic in Section 4.2 where we showed that a direct IMF-σ relation is unlikely and that the IMF correlates much better with metallicity. The velocity dispersion σ is more likely to directly correlate with metallicity, causing the appearance of an IMF-σ correlation. Here we check the reported [Mg/Fe]-σ relation. Since magnesium is a tracer for α in general (Worthey, Faber & Gonzalez, 1992; Trager et al., 1998), we review the [α/Fe] relations with IMF and σ. In Section 4.3 we already reported a lack of relation between the [α/Fe] and other stellar population parameters. However, a relation might exist between the IMF (or σ) and one or more individual α-elements. To investigate this, we look at the IMF sensitivity of the absorption lines of α-sensitive features in our sample: O, Mg, Ca, Ti, and Fe. Moreover, we also study the general [α/Fe] atmospheric parameter as retrieved from the CvD12 SSP models.

Table 5.1: Correlation coefficient of α indices vs. IMF slope

Index	ρ	p-value
bTiO	-0.008	0.95
Mg_b	0.38	10^{-3}
$\langle Fe \rangle$	0.39	10^{-3}
[MgFe]	0.46	10^{-4}
TiO1	0.23	0.07
TiO2	0.65	10^{-9}
CaH1	0.35	10^{-2}

We report in Section 4.1 that, in the set of α-element-sensitive indices, TiO2 seems to be the best IMF tracer, while all the other elements are less or not correlated with IMF slope. Using a method similar to the one used to calculate gradients, we determine the Spearman correlation coefficient for these indices with respect to the best-fit IMF slope to see how consistent the sensitivity is. The results are shown in Table 5.1. In this table the p-value is the probability that the null-hypotheses (the assumption that two variables are not correlated) is true. Here we see that indeed TiO2 has the strongest correlation with the IMF-slope. It is surprising to note the lack of correlation the IMF-slope seems to have with the bTiO value, a generally accepted IMF-sensitive index. We note that this value does not mean the bTiO does not play a role in dwarf-star measurements, it means that the χ^2 fitting procedure prefers TiO2 as a stronger base for its model-fitting. The idea that an enhancement in α-elements correlates with a change in the IMF slope is not apparent based on the correlation between the IMF slope and the individual α-element sensitive indices. Comparing the [α/Fe] values with the IMF slope, there is also no correlation ($\rho = 0.16$).

The [α/Fe] parameter is expected to correlate with the velocity dispersion (e.g. Trager et al. 2000b; Arrigoni et al. 2010; Conroy & van Dokkum 2012b). In Figure 5.2 on the top panel we plot the [α/Fe]-σ relation together with the relation derived in Trager et al. (2000a). It is clear that our data does not follow this relation since our measured [α/Fe] is not sensitive to σ. In the individual α-sensitive indices there seems to be a positive correlation between σ and magnesium, iron, and the TiO1 indices. In the remaining α-sensitive indices there seems to be a lack of relation.

As expected, $Mg_b/\langle Fe \rangle$ shows similar invariance with σ thanks to their links with α (Figure 4.5). This result is inconsistent with Conroy & van Dokkum (2012b) but consistent with Martín-Navarro et al. (2015a).

In Figure 5.3 we compare our values to the values reported in Arrigoni et al. (2010). They presented the $\mathrm{Mg_b}/\langle\mathrm{Fe}\rangle$ fractions for systems in a broad range of galaxy mass. Despite the invariance [α/Fe] shows with σ, our values agree with the values of Arrigoni. In Figure 5.3 we show that on a larger range of σ our points (within the error bars) follow those of Arrigoni relatively well, even though our points seem invariant with σ when viewed on their own. Our points tend to be slightly higher and have a bit more scatter in the $\mathrm{Mg_b}/\langle\mathrm{Fe}\rangle$ values.

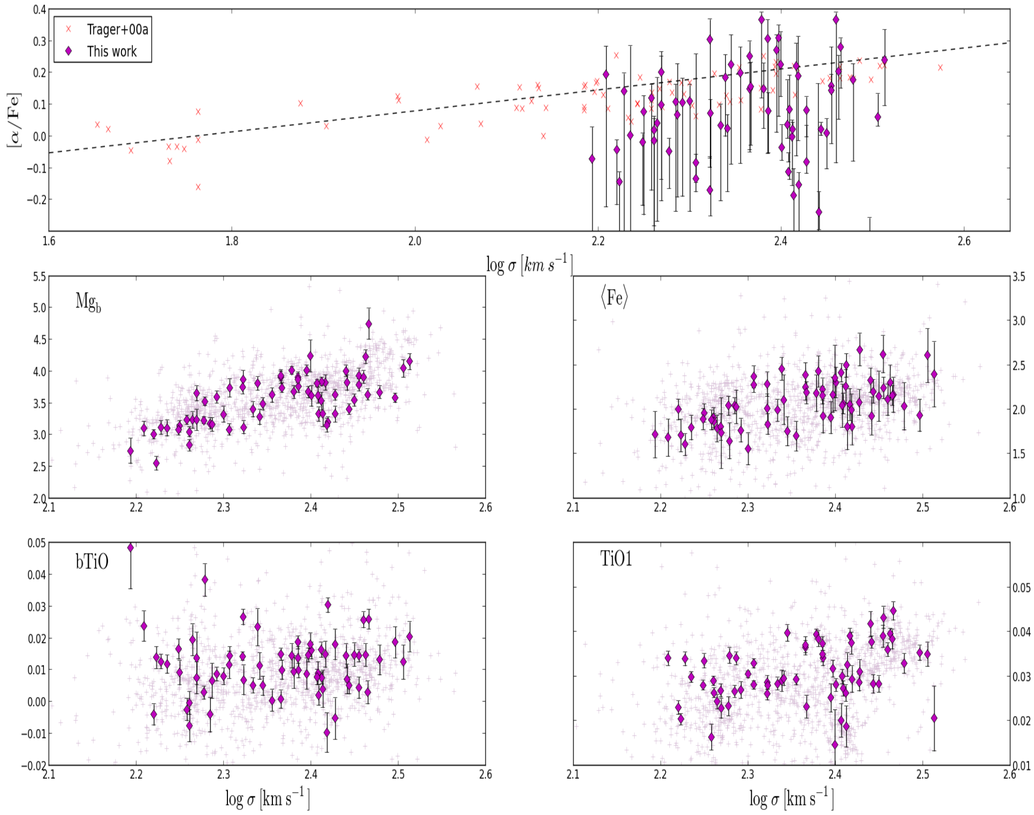

Figure 5.2: Upper panel: the [α/Fe]-σ relation. Lower panels: various α elements as function of the stellar velocity dispersion. The purple diamonds are the elliptical bins and the purple crosses are the Voronoi bins. The red crosses are results from Trager et al. (2000a). The dashed line is the [α/Fe]-σ relation from Trager et al. (2000a): [α/Fe] $= 0.33\log\sigma - 0.58$. In later work Arrigoni et al. (2010) reported that the Trager relation is too high by a factor of ~0.1-0.25 dex, a correction which makes the line fit out data better as well. The magensium, iron, and the TiO indices correlate positively with σ. Not plotted are [TiO2, σ], which shows similar behaviour as TiO1, and [CaH1, σ], which shows no relation.

The flat distribution we see in [α/Fe] and $\mathrm{Mg_b}/\langle\mathrm{Fe}\rangle$ is also present in our radial gradients where ∇ $\mathrm{Mg_b}/\langle Fe\rangle \sim 0$. This is consistent with key point (4) in the paper of Kuntschner et al. (2010) discussed above, who report that abundance ratios remain typically flat (or slightly rising) with radius. This behaviour is also reported in McConnell, Lu & Mann (2016), where they investigated two ETGs and discover no radial gradients in either [Mg/Fe] or [α/Fe]. In Figure 4.9 we also report a lack of radial gradient [α/Fe], and in Figure 4.8 we show that [α/Fe] in individual galaxies show no clear pattern.

The consistency with the Kuntschner et al. (2010) and McConnell, Lu & Mann (2016) gradients and the Arrigoni et al. (2010) values shows that our values are consistent with other findings. We cannot definitively explain why studies like Trager et al. (2000a) and Conroy & van Dokkum (2012b) find a clear [α/Fe]-σ relation and we do not. We suspect that, similar to Subsection 4.2.1 where the IMF-σ relation is reported in unresolved data and not found in resolved data (Martín-Navarro et al., 2015a,b), the [α/Fe]-σ relation is present in unresolved data and absent in resolved data. This would mean that general relations with velocity dispersions are less prominent in unresolved data.

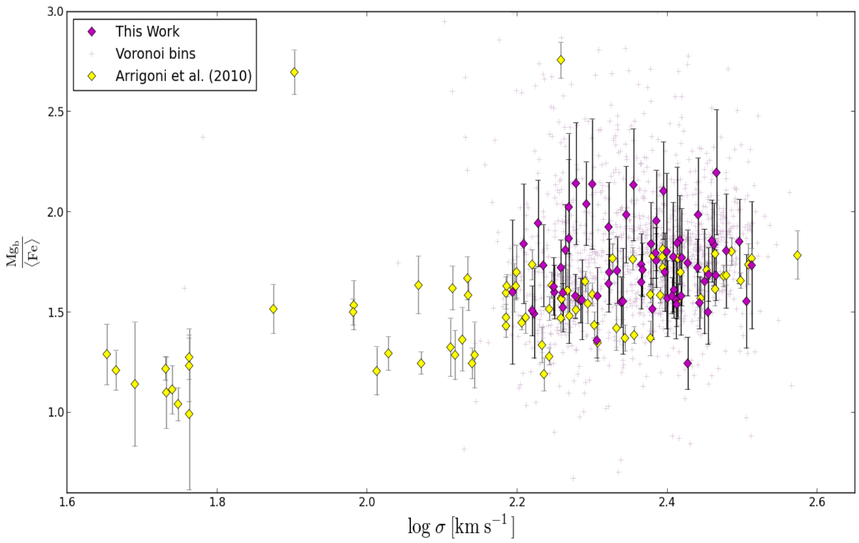

Figure 5.3: Figure showing a comaprison in the $Mg_b/\langle Fe \rangle$ space of our results (purple diamonds) versus those of Arrigoni et al. (2010) (yellow diamonds). Despite our lack of finding an [α/Fe]-σ relation, the values in $Mg_b/\langle Fe \rangle$ seem to follow the findings of Arrigoni et al..

5.5 Recent studies on the IMF slope

In this subsection we briefly discuss other recent work published in the field of the IMF slope that has not been discussed in previous sections. Recent studies on IMF variations and radial variation in stellar population parameters in ETGs are discussed.

Weidner et al. (2013a) (hereafter W13) compared different IMF studies and mentioned that there is no consistency reported in the shape of the IMF over a large range of stellar masses. They pointed out that, in ETGs, a Kroupa IMF produces too few low-mass stars and that a bottom-heavy IMF fails to explain the high metallicities in the systems. To circumvent these shortcomings, W13 proposed an evolving, two-phase IMF (not to be confused with the two-phase formation model of ETGs). They proposed that ETGs are formed with a short ($\leq$ 0.3 Gyr) initial star-burst with high star-formation efficiency, producing a top-heavy IMF. This first stage ensures that the ISM of the system is sufficiently metal-enriched. This process is followed by a second stage in which the bulk of the stellar mass is formed with a bottom-heavy IMF. This process creates the low-mass stars, which would agree with ETG observations. W13 defined a transition time-scale, Δt_{IMF}, which tracks the expected timescale necessary for a system to transform from a top-heavy to a bottom-heavy IMF; Δt_{IMF} is in the order of $\sim$ 1 Gyr. W13 underlined the necessity of a time-dependent IMF shape. This fits in our findings of the previous chapter, where we determine a steep initial IMF gradient in ETGs, in which the IMF is steepest in the center. Since we need high metallicities for steep IMF slopes, a short, highly efficient, starburst phase is the best possibility to achieve these values. Finally, also metallicity gradients are well explained in this scenario, because starbursts will take place in the innermost region and will not heavily influence the outskirts.

Greene et al. (2015) (hereafter G15) examined radial trends in the stellar population parameters of ~100 ETGs from the MASSIVE survey. They examined and compared stacked spectra of both the central regions (≤ 0.5 $R_{\rm eff}$) and the outskirt of the galaxies at up to 2.5 $R_{\rm eff}$. They focused on various abundance ratios ([Fe/H], [α/Fe], [C/Fe], [N/Fe], [Ca/Fe]) as well as stellar age. They analysed the results with the assumption that ETGs form hierarchically. In the central bins the strongest radial gradients were present in [Fe/H] and [C/Fe], which both decline with radius. All other abundance ratios remained flat. Galaxies with higher σ-values had older stellar ages and higher [α/Fe] and [C/Fe] ratios. At larger radii these trends with σ got weaker and over a wide range of σ (as well as galaxy mass) the abundance ratios were similar. G15 did not find significant gradients in either age or [α/Fe], and only gentle gradients in [Fe/H], which is a tracer of metallicity via [Z/H] = [Fe/H] + 0.94[α/Fe] (Trager et al., 2000b). In the central region age and [α/Fe] rose with increasing σ values, while in the outer radii the stellar population parameters were similar with values in lower mass galaxies. Since minor, wet mergers will accrete onto the primary galaxy and will not penetrate the inner regions, this result confirms the validity of the hierarchical formation model. Even though G15's measurements extend radially beyond our range, we can still compare similarities in radial variations. They find no significant gradients in the age parameter of their galaxies, with which we agree upon, based on our *average* age gradient (Figure 4.9). Individual galaxies, however, show strong age gradients, with the most extreme galaxies exceeding a gradient of 7 Gyrs. [α/Fe] in G15 does not seem to have a significant spatial gradient, but the overal values rise with increasing σ. We find similar results in the [α/Fe] gradients. However, it is puzzling that G15 finds an [α/Fe]-σ correlation in resolved spectra, whereas, as mentioned in previous sections, other studies based on resolved spectra do not.

La Barbera, Ferreras & Vazdekis (2015) fitted radial trends with the TiO lines in massive ETGs from the SPIDER sample. Their best-fit IMF model consisted of a bimodal slope whose IMF-slope above 0.5 $M_{\odot}$ declines from x = 3 in the centre to Salpeter (x = 2.35) at 0.5 $R_{\rm eff}$. Martín-Navarro et al. (2015b) measured IMF gradient in two high-mass galaxies and one low-mass galaxy. They fitted a bimodal IMF and found, within the high-mass galaxies, a Salpeter-like slope at 0.7 $R_{\rm eff}$ with an extreme slope up to x = 4 near the centre. The low-mass galaxy did not show radial variations. Both of these studies found an IMF slope steepening towards the centre. We find similar trends, where a bottom-heavy IMF in the center leads to radially shallower IMFs. But not all the galaxies require a bottom-heavy IMF in the centre; the IMF slope of galaxies with a shallow IMF in their centre tend to rise slightly or remain radially invariant.

A crucial difference that must be highlighted between these papers and our work is that, while they vary the high-mass end slope of the IMF, we vary the low-mass end. Our IMF slope *on average* radially declines from x ~ 2.75 at 1/8 $R_{\rm eff}$ to slightly sub-Salpeter at 1 $R_{\rm eff}$. So we do not find on average the extreme central values that Martín-Navarro et al. (2015b) measure (although individual galaxies can have IMF-slopes up to x ~ 3.5 in the centre), but we underline that the IMF shows radial flattening.

McConnell, Lu & Mann (2016) measured radial gradients and abundance ratios in 2 ETGs. Their dwarf sensitive features, NaI and the Wing-Ford band (FeH), seem to lead to contradictory results. Where [NaI/⟨Fe⟩] shows a a sharp rise towards the centre, FeH shows a decrease towards the centre. They explained this by noticing that although the peak cool-dwarf sensitivity in both NaI and FeH lies below 0.2 $M_{\odot}$, the cool-dwarf sensitivity of FeH declines twice as fast as that of NaI. Therefore a radial trend in NaI but not in FeH could expose an IMF that only gets bottom-heavy above 0.4 $M_{\odot}$.

5.6 Future work

This work shows that the IMF in ETGs can vary both with time and in space. Possible physical processes behind these variations include the merging history of galaxies as well as the contribution of stellar feedback through supernovae and stellar winds. The next step forward should be to move the question from 'is the IMF universal?' to 'are there universal processes which affect the IMF in a predictable way?' The goals are to 1) understand what drives the IMF variations (physical processes, both local and global) and 2) build up a consistent formation/evolution scenario able to explain all the observations on different scales and systems.

We need to determine on which physical parameters IMF is the most dependent. From this work metallicity is a prime candidate, but other parameters like kinematics and abundance ratios can not be completely excluded. If the statement that the merging history of galaxies influences [M/H] and thus IMF in a more or less predictable manner is true, one way to continue this search is to do simulations of galaxies with different merging histories with some predetermined set of SSP models and determine whether or not we are able to reproduce the parameters we measure. If such results are positive, we are able to shine some new light on the theories of galaxy formation.

More study should be done on the IMF of late-type galaxies (LTGs). In particular the possible similarities between the IMFs in LTGs, ETGs, and other stellar structures. LTGs generally consist of younger stellar populations and have not been subjected to past major mergers. If here we find similar IMF dependencies it could underline our understanding of the physical processes which drive the IMF. The IGIMF theory seems to have started this process of IMF unification (Weidner & Kroupa, 2005).

We could determine the early-phase IMFs by examining objects at high redshift. The advantage is that we can make a time-dependent picture of the IMF (as previously done by Davé, 2008) and confirm the idea of a time-varying IMF. The downside is that we are currently not able to resolve the galaxies at high redshift to determine actual radial variations and thus need to limit ourselves to integrated measurements of the IMF slope at these distances.

We can look at the various results provided by different SSP models, or extend on the current ones. We use MILES (Falcón-Barroso et al., 2011) and CvD12 (Conroy & van Dokkum, 2012a) models in this project, but other models based on stellar libraries like UVES-POP (Bagnulo et al., 2003) and XSL (Chen et al., 2014) provide good alternatives. As mentioned in Spiniello, Trager & Koopmans (2015), different models give different predictions on the amount of IMF variation, especially for different sets of indices. It is therefore necessary to test and fully understand the underlying assumptions and the different ingredients used by SSP models.

Finally, the assumption of a power-law IMF should be relaxed. A lot of possible IMF shapes have been proposed for a various amount of structures. IMF can be Salpeter, a Chabrier-like log-normal, a uni-, bi- or even tri-modal, the low-mass end can steepen or flatten, and the same goes for the high-mass end. In recent work Lyubenova et al. (2016) compared the dynamical mass-to-light ratio (Υ_{dyn}) with the stellar mass-to-light ratio (Υ_*). They fitted SSPs assuming both a unimodal IMF or a bimodal IMF with a varying high-mass end slope and compare the resulting mass-to-light ratios. Using the physical limit of $\Upsilon_{dyn} \geq \Upsilon_*$ they reported that the unimodal IMF breaks this limit for the majority of their sample whereas the bimodal IMF did not violate this constraint (within error-bar limits). From this they concluded that the unimodal slope for the IMF should be discarded, since it is unable to predict physically valid mass-to-light ratios. With research like this we can discard certain IMF theories and further constrain the IMF shapes.

6

Conclusion

The IMF function is a relation that describes the mass distribution of formed stars in a single star-forming phase. The general shape of the IMF is the subject of great debate and it is still unclear what the general processes that set the IMF slope are. Studies on the IMF are dominated by two approaches: the dynamical approach in which the IMF is inferred via stellar kinematics and gravitational lensing (e.g. Auger et al. 2010; Treu et al. 2010; Cappellari et al. 2012), and the spectroscopic approach in which the IMF is inferred via absorption lines and abundance ratios (e.g. Conroy & van Dokkum 2012b; Spiniello et al. 2014; Martín-Navarro et al. 2015a).

In this thesis we approached the IMF in a spectroscopic way. We presented resolved stellar population studies of 17 ETGs taken from the CALIFA data sample (Sánchez et al., 2012). The galaxies were rebinned in four elliptical apertures, from 1/8 R_{eff} up to 1 R_{eff}, with the goal of determining atmospheric parameter variations at different radial distances. We used pPXF (Cappellari & Emsellem, 2004) to determine the stellar kinematics of the spectra and we used GANDALF (Sarzi et al., 2006) to clear the spectra from emission line contamination. We then extracted Lick/IDS indices, as well as newly defined indices, using SPINDEX (Trager, Faber & Dressler, 2008) comparing them with the ones measured in a set of CvD12 SSP models (Conroy & van Dokkum, 2012a) in order to extract the different stellar population parameters of the spectra based on the best-fit models. The parameters extracted are IMF slope (x) , metallicity (Z or [M/H]), α-abundance ratio [α/Fe], sodium-abundance ratio [Na/Fe], and stellar age (t). We compared our extracted values and relations between the parameters with previously reported ones in order to validate our findings. The IMF-σ (e.g. Spiniello et al. 2014), IMF-[M/H] (Martín-Navarro et al., 2015c), [α/Fe]-σ (e.g. Trager et al. 2000a) relations, and the NaD influence on the IMF slope (Spiniello, Trager & Koopmans, 2015) have been discussed.

We then focused our attention on radial gradients within the ETGs. Gradients in metallicity (and thus in the IMF-slope) are reported to be affected by the formation history of the galaxy. There are two things to keep in mind. First, to explain the IMF in ETGs it is proposed that the initial star-formation produces a top-heavy IMF. These giant stars will die quickly, injecting the ISM with metals needed to explain the bottom-heavy IMFs we see today (Weidner et al., 2013a; Ferreras et al., 2015). Second, the metallicity gradient is heavily influenced by the formation history of the galaxies. Monolithic collapse predicts steep metallicity gradients with metal-rich centres where hierarchical formation models predict shallower gradients. Secondary star-formation via mergers will again change the metallicity gradients. Non-major mergers will cease star-formation in the outer regions, thereby steepening the metallicity gradients. Major mergers, however, will force metal-rich stars to migrate towards the outer regions, thereby flattening the gradient (Kobayashi, 2004). Thus looking at the metallicity gradient and IMF-slope gradients will allow us to infer merging histories of galaxies.

We recap the main results of our analysis below:

- In our set of Lick/IDS indices the IMF, as inferred from CvD12, is most correlated with the TiO2 and NaD indices. Surprisingly, the bTiO index is uncorrelated despite being previously considered an IMF-sensitive index (Spiniello et al., 2014). Furthermore, we find similar trends in TiO2 and NaD with the velocity dispersion (σ) and metallicity, which indicates that there is a relation between these two parameters and the IMF.

- The IMF-σ relation is very loose in our sample. Multiple studies have reported the existence of this relation (e.g. La Barbera et al. 2013; Spiniello et al. 2014) and some studies have reported the absence of this relation (Martín-Navarro et al., 2015a). It appears that studies that confirm the IMF-σ relation are all reported in unresolved stellar populations, whereas both Martín-Navarro et al. (2015a) and this study, who do not find a clear IMF-σ relation, use resolved stellar populations. Most likely the reported IMF-σ relation is due to an interplay between the IMF-[M/H] relation and the [M/H]-σ relation.

- We report an IMF-[M/H] relation and confirm the linear relation derived in Martín-Navarro et al. (2015c) (MN15). The main difference between these studies is that MN15 varies the high-mass end of the IMF, where we vary the low-mass end. The combined results of MN15 and this work tells us that the fraction of low-mass stars to high-mass stars grows with increasing metallicity regardless of which portion of the IMF you vary. Since metallicity is regulated through stellar nucleosynthesis, it depends heavily on the IMF and the star-formation history (SFH). The SFH depends on the formation history of galaxies which, on its turn, affects the metallicity gradient (Kobayashi, 2004). These relations make it possible to determine the merging history of galaxies based on gradients (∇) in stellar population parameters.

- We determine the averages of the stellar stellar population parameters for every elliptical radial bin to investigate mean radial trends of our sample. On average the radial IMF slope flattens from x ~ 2.75 to slightly sub-Salpeter (x <2.35) at 1 R_{eff}. Similar trends are shown in metallicity, where the difference between inner and outer bin are on average -0.21 dex. On average the stellar age remains flat over radius, but in the individual galaxies there are differences. ETGs that are old in the centre tend to remain old over radius whereas ETGs that have young centres age radially with differences up to 7 Gyr. ETGs with younger centres have steep IMF-slopes in the inner regions as well, as expected of galaxies that underwent non-major mergers.

- A tight relation between the IMF gradient and the metallicity gradient is shown. Steep (negative) metallicity gradient coincide with steep (negative) IMF slope gradients. This is in accord with our previous point, where higher metallicities relate to steeper IMF slopes. Kobayashi (2004) reports that the merging history of galaxies can be inferred from the radial gradients in metallicity and, thus, from the IMF-slope. Galaxies that underwent non-major mergers have a steeper negative metallicity than galaxies that underwent a major merger, where the turn-off between these two is between ∇[M/H] = -0.3 – -0.22. Non-major mergers cease star-formation outside-in, leading to enhanced metallicities, a steeper IMF slope, and younger stellar populations in the inner radii. In our sample seven galaxies have ∇[M/H] < -0.3, implying a non-major merger history.

- In the other atmospheric parameter gradients there is an inverse correlation between ∇t and ∇x, as is in accord with the idea that non-major mergers have both steeper IMF-slopes in the centre as well as continuous star-formation causing a younger population. A similar trend is seen in ∇[Na/Fe] vs. ∇x, which supports the suspision of Spiniello, Trager & Koopmans (2015) that the NaD index and sodium fraction have a huge impact on the inferred IMF-slope.

In conclusion, multiple studies on the IMF in ETGs point towards a two-phased IMF shape. The original star-forming phase originates from one massive gas cloud, creating a stellar mass distribution with a top-heavy IMF. After 1 – 2 Gyr most of the stars in the high-mass bins will have died and injected the ISM with metals, creating the high metallicity that is measured in bottom-heavy IMF regions. In the monolithic collapse scenario the story ends here, where the giant stars mainly populate the centres, thereby mainly enhancing metallicity in the inner regions causing a steep radial gradient.

In the hierarchical formation model the ETGs grow with multiple mergers. Mergers are classed as major, minor, wet, and/or dry. The high velocity dispersions in our ETG sample implies that both wet and dry mergers are present. The major and minor mergers both have their unique effect on the galaxy's star formation. Major mergers will perturb the galaxy to small radii, forcing metal-rich stars to migrate outward, thereby flattening the metallicity gradient. Minor mergers will accrete more quiescent on the parent galaxy, thereby heating the ISM in the outer regions and ceasing star formation. It is even possible for the gas of the infalling galaxy to fall inward and induce star formation in the inner regions. Minor mergers will, therefore, steepen the metallicity and IMF gradient.

The proposed relation of Martín-Navarro et al. (2015c) between IMF and metallicity, a relation we find as well, could be a gateway to a new method of probing the IMF. Determining the IMF by measuring the metallicity could be more straightforward than measuring the IMF through the conventional methods of gravitational lensing and absorption line spectroscopy. This, however, will heavily depend on the tightness of the IMF-metallicity relation and will be worth investigating in future works.

Acknowledgements

I started this project with the idea it would take me around 18-20 months. Yes, I was adorable back then. In the end the project took me over three years to complete. Three years in which there were ups and downs, both mentally and physically, but also three years which in retrospect have been necessary to let me make mistakes I would've otherwise made later in life. Of course, three years is way too long and there are no excuses for that, but this I cannot change now and in the end I am content with the stuff I wrote above. Beneath I will thank and give credits to the people who most deserve it.

First and foremost there is **Scott**. You gave me a project which was challenging and interesting and (especially in the first year) I enjoyed the work on the project a lot. And despite my own scrappy periods during the project, our working relationship never seemed to be influenced by that and remained good. Besides that you showed incredible patience with me by just letting me mess around with random ideas, only to call me back when I was really going off-track or took too much time with minor distractions. I understand you had some pressure from higher-up to get me to finish something already and I cannot thank you enough for keeping that behind my back. I cannot predict how I would've reacted to that half a year ago. Thank you for everything.

And then there is **Chiara**. Your seemingly endless jar of enthusiasm really helped me through the project. Even if the results (or my writing) were not that great, you still made me feel fired-up and positive about everything I did. The random espresso's in the afternoon to talk about science and/or life are also still fresh in my memory and are things I definitely missed once you left the institute. But even from a distance you were very helpful, always ready to respond to e-mail, and even being prepared to Skype on short notices. I think you were as near as I got to the social aspect of astronomy. So... thanks :).

To finish the thanks related to the research I will need to thank CALIFA, my data provider. This study, as mentioned throughout the thesis, uses data provided by the Calar Alto Legacy Integral Field Area (CALIFA) survey (`http://califa.caha.es/`). Based on observations collected at the Centro Astronómico Hispano Alemán (CAHA) at Calar Alto, operated jointly by the Max-Planck-Institut für Astronomie and the Instituto de Astrofísica de Andalucía (CSIC). On a personal note I need to thank **Mariya** for being helpful when it came to technical details regarding CALIFA as well as being able to explain to me the awkward programming language that is IDL.

The other people of the stellar evolution group (does the group have an official name?) also need a mention. Over the past few years I have seen multiple people come and go and here I am going to list everyone I can remember: **Wouter, Matthijs, Anke, Shoko, Annais, Sofia, Yan-Ping, Gergö, Judith**. If I forgot people... well, it is unlikely they will read this anyway :). All the people above: thanks for the discussions and the interesting group meetings throughout the years. Also thanks to **Casper** and **Marten** for making the office a little more lifelike while working there.

On a personal level I would like to thank my roommates. **Douwe** for being the original glue of a house in which I loved living for the past few years as well as sharing interests in complex board games and fantasy novels. **Mikael** for sharing my thesis-struggles for several years and for the mutual fondness of whisky. **Daan**, for being the Diddy to my Donkey Kong. **Niels**, because he wanted to be mentioned.

Finally an eternal thanks goes out to my parents **Henk** and **Caroline**. Jullie hebben mij al die jaren gewoon mijn ding laten doen. In voor en tegenspoed zijn jullie mij blijven steunen en hebben jullie mij voorzien van ouderlijk advies (en soms wat financiële steun). Zonder die dingen had ik het misschien halverwege wel opgegeven. Echter, het schrijven van dit stuk betekent dat ik het alsnog gehaald heb. Woorden zullen mijn volledige dankbaarheid niet kunnen bescrhijven, dus hier zullen jullie het vooralsnog mee moeten doen. Ik ben net zo benieuwd als jullie op wat er nu gaat gebeuren.

Bibliography

Arrigoni M., et al., 2010, MNRAS, 402, 173

Auger M. W., et al., 2010, ApJL, 721, L163

Bagnulo S., et al., 2003, The Messenger, 114, 10

Barnes J. E., 1992, ApJ, 393, 484

Bastian N., Covey K. R., Meyer M. R., 2010, ARAA, 48, 339

Bender R., Burstein D., Faber S. M., 1992, ApJ, 399, 462

Bender R., Burstein D., Faber S. M., 1993, ApJ, 411, 153

Bernardi M., et al., 2003, AJ, 125, 1866

Bernardi M., et al., 2005, AJ, 129, 61

Blumenthal G. R., et al., 1984, Nature, 311, 517

Burkert A., Naab T., 2003, in Galaxies and Chaos Vol. 626 of Lecture Notes in Physics, Berlin Springer Verlag, Major Mergers and the Origin of Elliptical Galaxies. pp 327–339

Burstein D., et al., 1984, ApJ, 287, 586

Cappellari M., Copin Y., 2003, MNRAS, 342, 345

Cappellari M., Emsellem E., 2004, PASP, 116, 138

Cappellari M., et al., 2012, Nature, 484, 485

Cappellari M., et al., 2013, MNRAS, 432, 1862

Carlberg R. G., 1984, ApJ, 286, 403

Chabrier G., 2003, PASP, 115, 763

Chabrier G., 2005, in Corbelli E., Palla F., Zinnecker H., eds, The Initial Mass Function 50 Years Later Vol. 327 of Astrophysics and Space Science Library, The Initial Mass Function: from Salpeter 1955 to 2005. p. 41

Chen Y.-P., et al., 2014, The Messenger, 158, 30

Ciotti L., Bertin G., 1999, AaP, 352, 447

Clemens M. S., et al., 2006, MNRAS, 370, 702

Conroy C., et al., 2013, ApJL, 776, L26

Conroy C., van Dokkum P. G., 2012a, ApJ, 747, 69

Conroy C., van Dokkum P. G., 2012b, ApJ, 760, 71

Cushing M. C., Rayner J. T., Vacca W. D., 2005, ApJ, 623, 1115

Daddi E., et al., 2005, ApJ, 626, 680

Davé R., 2008, MNRAS, 385, 147

de Vaucouleurs G., 1948, Annales d'Astrophysique, 11, 247

Djorgovski S., Davis M., 1987, ApJ, 313, 59

Dressler A., Lynden-Bell D., Burstein D., et al., 1987, ApJ, 313, 42

Eggen O. J., Lynden-Bell D., Sandage A. R., 1962, ApJ, 136, 748

Emsellem E., et al., 2007, MNRAS, 379, 401

Faber S. M., Jackson R. E., 1976, ApJ, 204, 668

Falcón-Barroso J., et al., 2011, AaP, 532, A95

Fardal M. A., et al., 2007, MNRAS, 379, 985

Ferreras I., et al., 2015, MNRAS, 448, L82

Fontanot F., et al., 2016, ArXiv e-prints

Gallazzi A., et al., 2008, MNRAS, 383, 1439

García-Benito R., et al., 2015, AaP, 576, A135

Gerhard O. E., 1993, in Danziger I. J., Zeilinger W. W., Kjär K., eds, European Southern Observatory Conference and Workshop Proceedings Vol. 45, New Dynamical Models for Elliptical Galaxies: Line-Of-Sight Velocity Profiles, Anisotropy and Mass Distribution. p. 311

González J. J., 1993, PhD thesis, Thesis (PH.D.)–UNIVERSITY OF CALIFORNIA, SANTA CRUZ, 1993.Source: Dissertation Abstracts International, Volume: 54-05, Section: B, page: 2551.

Gott III J. R., 1975, ApJ, 201, 296

Greene J. E., et al., 2015, ApJ, 807, 11

Gunawardhana M. L. P., et al., 2011, MNRAS, 415, 1647

Hopkins P. F., 2013, MNRAS, 433, 170

Hoversten E. A., Glazebrook K., 2008, ApJ, 675, 163

Hubble E. P., 1936, The Realm of the Nebulae. Dover Publications, Inc.

Husemann B., et al., 2013, AAp, 549, A87

Kelz A., et al., 2006, PASP, 118, 129

Kobayashi C., 2004, MNRAS, 347, 740

Kobayashi C., Arimoto N., 1999, ApJ, 527, 573

Kroupa P., 2002, Science, 295, 82

Kuntschner H., et al., 2010, MNRAS, 408, 97

La Barbera F., et al., 2013, MNRAS, 433, 3017

La Barbera F., Ferreras I., Vazdekis A., 2015, MNRAS, 449, L137

Leitherer C., Robert C., Drissen L., 1992, ApJ, 401, 596

Li H., Cui W., Zhang B., 2013, ApJ, 775, 12

Loeb A., Peebles P. J. E., 2003, ApJ, 589, 29

Lyubenova M., et al., 2016, ArXiv e-prints

Martín-Navarro I., et al., 2015a, ApJL, 798, L4

Martín-Navarro I., et al., 2015b, MNRAS, 447, 1033

Martín-Navarro I., et al., 2015c, ApJL, 806, L31

McConnell N. J., Lu J. R., Mann A. W., 2016, ApJ, 821, 39

Miller G. E., Scalo J. M., 1979, ApJS, 41, 513

Naab T., et al., 2014, MNRAS, 444, 3357

Naab T., Jesseit R., Burkert A., 2006, MNRAS, 372, 839

Naab T., Johansson P. H., Ostriker J. P., 2009, ApJL, 699, L178

Nelan J. E., et al., 2005, ApJ, 632, 137

Offner S. S. R., et al., 2014, Protostars and Planets VI, pp 53–75

Oke J. B., 1990, AJ, 99, 1621

Padmanabhan N., et al., 2008, ApJ, 674, 1217

Pahre M. A., Djorgovski S. G., de Carvalho R. R., 1998, AJ, 116, 1591

Prugniel P., Simien F., 1996, AaP, 309, 749

Recchi S., Kroupa P., Ploeckinger S., 2015, MNRAS, 450, 2367

Salpeter E. E., 1955, ApJ, 121, 161

Sánchez S. F., et al., 2012, AAp, 538, A8

Sánchez S. F., et al., 2016, ArXiv e-prints

Sánchez-Blázquez P., et al., 2006, MNRAS, 371, 703

Sargent W. L. W., et al., 1977, ApJ, 212, 326

Sarzi M., et al., 2006, MNRAS, 366, 1151

Serra P., Trager S. C., 2007, MNRAS, 374, 769

Sérsic J. L., 1963, Boletin de la Asociacion Argentina de Astronomia La Plata Argentina, 6, 41

Shepard D., 1968, in Proceedings of the 1968 23rd ACM National Conference ACM '68, A two-dimensional interpolation function for irregularly-spaced data. ACM, New York, NY, USA, pp 517–524

Smith R. J., 2014, MNRAS, 443, L69

Spiniello C., et al., 2011, MNRAS, 417, 3000

Spiniello C., et al., 2012, ApJL, 753, L32

Spiniello C., et al., 2014, MNRAS, 438, 1483

Spiniello C., Trager S. C., Koopmans L. V. E., 2015, ApJ, 803, 87

Strateva I., et al., 2001, AJ, 122, 1861

Tinsley B. M., 1972, ApJ, 178, 319

Toomre A., Toomre J., 1972, ApJ, 178, 623

Trager S. C., et al., 1998, ApJS, 116, 1

Trager S. C., et al., 2000a, AJ, 120, 165

Trager S. C., et al., 2000b, AJ, 119, 1645

Trager S. C., Faber S. M., Dressler A., 2008, MNRAS, 386, 715

Trager S. C., Somerville R. S., 2009, MNRAS, 395, 608

Tremonti C. A., et al., 2004, ApJ, 613, 898

Treu T., et al., 2010, ApJ, 709, 1195

Trujillo I., Burkert A., Bell E. F., 2004, ApJL, 600, L39

van de Sande J., et al., 2013, ApJ, 771, 85

van der Marel R. P., Franx M., 1993, ApJ, 407, 525

van Dokkum P. G., Conroy C., 2010, Nature, 468, 940

Vazdekis A., et al., 2012, MNRAS, 424, 157

Vincenzo F., et al., 2015, MNRAS, 449, 1327

Walcher C. J., et al., 2014, AaP, 569, A1

Weidner C., et al., 2013a, MNRAS, 435, 2274

Weidner C., et al., 2013b, MNRAS, 436, 3309

Weidner C., Kroupa P., 2005, ApJ, 625, 754

White S. D. M., Rees M. J., 1978, MNRAS, 183

Worthey G., 1994, ApJS, 95, 107

Worthey G., et al., 1994, ApJS, 94, 687

Worthey G., Faber S. M., Gonzalez J. J., 1992, ApJ, 398, 69

Worthey G., Ottaviani D. L., 1997, ApJS, 111, 377

York D. G., et al., 2000, AJ, 120, 1579

Appendix A

Appendix A contains 3 tables. Table AI presents the measured SPINDEX values of Lick/IDS indices bTiO, Hβ, Mg_b, Fe5270, Fe5335, and [MgFe]. Table AII presents the measured SPINDEX values of Lick/IDS indices NaD, TiO1, TiO2, and CaH1. Table AIII presents the best-fit SSP parameters dervied through χ^2 statistics. Cursive numbers and 'N/A' values are outliers and are discussed in Section 5.2.

Table AI

		bTiO [10^{-2}]	Hβ	Mg_b	Fe5270	Fe5335	[MgFe]
NGC0499	$R_{eff}/8$	2.60±0.31	1.14±0.19	4.75±0.24	2.21±0.24	2.12±0.14	3.20±0.12
	$R_{eff}/4$	1.47±0.35	1.34±0.14	4.23±0.11	2.52±0.24	2.08±0.14	3.12±0.10
	$R_{eff}/2$	0.71±0.46	1.33±0.12	3.82±0.12	2.16±0.26	1.69±0.16	2.71±0.11
	R_{eff}	1.48±0.41	1.39±0.19	3.82±0.12	2.29±0.22	1.82±0.13	2.80±0.09
NGC1349	$R_{eff}/8$	2.34±0.58	1.68±0.19	3.81±0.11	2.91±0.14	2.00±0.12	3.06±0.06
	$R_{eff}/4$	2.66±0.25	1.61±0.16	3.87±0.14	2.72±0.12	1.30±0.19	2.79±0.09
	$R_{eff}/2$	1.94±0.49	1.97±0.16	3.23±0.13	2.21±0.10	1.36±0.18	2.40±0.08
	R_{eff}	1.39±0.35	*2.55±0.45*	2.55±0.11	1.98±0.13	1.44±0.23	2.09±0.09
NGC5966	$R_{eff}/8$	0.86±0.22	1.61±0.09	3.60±0.10	2.09±0.14	1.43±0.13	2.52±0.07
	$R_{eff}/4$	*-0.41±0.55*	1.73±0.10	3.18±0.09	2.29±0.08	1.78±0.09	2.54±0.05
	$R_{eff}/2$	*-0.04±0.37*	1.70±0.05	3.04±0.08	2.18±0.09	1.64±0.12	2.41±0.05
	R_{eff}	*-0.76±0.50*	1.66±0.06	2.83±0.09	2.04±0.10	1.69±0.08	2.30±0.05
NGC6020	$R_{eff}/8$	1.43±0.13	1.59±0.11	3.75±0.11	2.63±0.15	1.94±0.12	2.93±0.07
	$R_{eff}/4$	0.75±0.50	1.84±0.13	3.65±0.12	1.94±0.18	1.67±0.12	2.57±0.08
	$R_{eff}/2$	1.18±0.29	1.73±0.07	3.10±0.13	2.09±0.15	1.50±0.13	2.36±0.07
	R_{eff}	1.26±0.23	1.88±0.07	3.11±0.11	1.81±0.14	1.40±0.10	2.23±0.07
NGC6125	$R_{eff}/8$	*-0.53±0.65*	1.74±0.04	3.32±0.12	2.84±0.21	2.50±0.14	2.98±0.08
	$R_{eff}/4$	0.98±0.22	1.54±0.08	3.76±0.10	2.06±0.23	1.79±0.16	2.69±0.10
	$R_{eff}/2$	0.04±0.34	1.65±0.11	3.62±0.12	1.90±0.19	1.50±0.15	2.48±0.09
	R_{eff}	0.80±0.26	1.40±0.13	3.32±0.12	1.84±0.17	1.27±0.19	2.27±0.10
NGC6146	$R_{eff}/8$	*1.87±0.49*	1.92±0.29	3.58±0.07	2.43±0.16	1.44±0.20	2.63±0.09
	$R_{eff}/4$	0.29±0.36	1.91±0.15	3.63±0.09	2.51±0.10	1.80±0.12	2.80±0.06
	$R_{eff}/2$	0.50±0.26	1.71±0.08	3.40±0.08	2.53±0.12	1.87±0.14	2.74±0.06
	R_{eff}	0.20±0.32	1.72±0.10	3.32±0.11	2.41±0.09	1.71±0.13	2.62±0.06
NGC6150	$R_{eff}/8$	1.38±0.36	1.56±0.11	3.90±0.08	2.57±0.14	1.88±0.10	2.95±0.06
	$R_{eff}/4$	1.49±0.19	1.52±0.08	3.90±0.10	2.58±0.15	1.91±0.13	2.96±0.07
	$R_{eff}/2$	*0.07±0.28*	1.69±0.16	3.93±0.09	2.80±0.12	1.97±0.16	3.06±0.07
	R_{eff}	1.47±0.22	1.71±0.12	3.67±0.09	2.56±0.13	1.76±0.25	2.82±0.09
NGC6173	$R_{eff}/8$	3.04±0.24	*0.93±0.22*	3.20±0.07	2.49±0.15	1.13±0.25	2.40±0.10
	$R_{eff}/4$	1.61±0.26	1.84±0.09	3.61±0.17	2.79±0.09	1.81±0.22	2.88±0.09
	$R_{eff}/2$	1.63±0.23	1.64±0.10	3.53±0.14	2.60±0.11	1.92±0.25	2.82±0.09
	R_{eff}	1.79±0.37	*4.90±0.86*	4.24±0.25	2.47±0.32	2.23±0.41	3.16±0.19

		bTiO [10^{-2}]	Hβ	Mg$_b$	Fe5270	Fe5335	[MgFe]
NGC6338	R$_{eff}$/8	2.04±0.47	*0.60±0.23*	4.15±0.13	2.71±0.25	2.08±0.46	3.15±0.17
	R$_{eff}$/4	1.25±0.54	1.24±0.17	4.05±0.14	3.03±0.17	2.18±0.39	3.25±0.14
	R$_{eff}$/2	1.31±0.47	1.65±0.12	3.67±0.10	2.50±0.15	1.57±0.35	2.73±0.13
	R$_{eff}$	0.40±0.58	1.86±0.17	3.33±0.20	2.18±0.32	1.43±0.19	2.45±0.14
NGC6411	R$_{eff}$/8	0.28±0.21	1.70±0.07	3.22±0.06	2.35±0.11	1.73±0.10	2.56±0.05
	R$_{eff}$/4	-0.25±0.35	1.89±0.04	3.24±0.07	2.32±0.11	1.44±0.11	2.47±0.05
	R$_{eff}$/2	-0.41±0.34	1.87±0.06	3.01±0.07	2.32±0.11	1.67±0.12	2.45±0.06
	R$_{eff}$	4.84±1.29	1.77±0.06	2.75±0.20	2.04±0.17	1.39±0.33	2.17±0.13
NGC6515	R$_{eff}$/8	*3.82±0.51*	2.23±0.12	3.52±0.07	2.06±0.21	1.23±0.20	2.41±0.11
	R$_{eff}$/4	0.91±0.38	1.59±0.08	3.13±0.09	2.22±0.10	1.70±0.11	2.48±0.05
	R$_{eff}$/2	1.66±0.32	1.71±0.14	3.08±0.08	2.43±0.08	1.36±0.15	2.41±0.06
	R$_{eff}$	2.38±0.47	1.95±0.11	3.10±0.12	2.26±0.18	1.10±0.24	2.28±0.11
NGC7194	R$_{eff}$/8	1.44±0.38	1.65±0.11	4.00±0.09	2.72±0.11	1.93±0.16	3.05±0.07
	R$_{eff}$/4	1.44±0.19	1.59±0.09	3.78±0.09	2.81±0.10	1.67±0.14	2.91±0.06
	R$_{eff}$/2	1.80±0.48	1.41±0.10	3.62±0.08	2.53±0.11	1.63±0.18	2.74±0.07
	R$_{eff}$	0.90±0.37	1.39±0.07	3.62±0.13	2.83±0.14	1.25±0.31	2.72±0.12
NGC7562	R$_{eff}$/8	0.75±0.20	1.67±0.05	3.83±0.07	2.87±0.16	2.12±0.10	3.09±0.06
	R$_{eff}$/4	0.77±0.24	1.60±0.06	3.81±0.06	2.81±0.08	2.01±0.12	3.03±0.05
	R$_{eff}$/2	0.87±0.49	1.76±0.10	4.01±0.08	2.40±0.17	1.41±0.19	2.77±0.10
	R$_{eff}$	0.99±0.30	1.61±0.11	3.74±0.08	2.56±0.13	1.82±0.12	2.86±0.06
UGC05771	R$_{eff}$/8	1.44±0.38	2.15±0.39	4.01±0.06	2.55±0.19	1.81±0.22	2.96±0.10
	R$_{eff}$/4	0.94±0.52	1.90±0.25	3.67±0.10	2.64±0.12	2.21±0.22	2.99±0.08
	R$_{eff}$/2	0.50±0.31	1.83±0.15	3.48±0.10	2.28±0.12	1.23±0.20	2.47±0.09
	R$_{eff}$	0.68±0.47	1.91±0.20	3.11±0.10	2.19±0.08	1.48±0.14	2.39±0.06
UGC10693	R$_{eff}$/8	*-0.97±0.63*	1.89±0.16	3.15±0.11	2.79±0.13	1.19±0.21	2.50±0.09
	R$_{eff}$/4	1.87±0.20	1.53±0.11	3.87±0.10	2.30±0.10	2.01±0.10	2.89±0.05
	R$_{eff}$/2	0.51±0.24	1.70±0.06	3.40±0.12	2.37±0.05	1.61±0.17	2.60±0.07
	R$_{eff}$	1.12±0.42	1.62±0.08	3.28±0.12	2.52±0.11	1.69±0.38	2.63±0.13
UGC10695	R$_{eff}$/8	1.43±0.31	1.38±0.26	3.73±0.14	2.61±0.10	2.12±0.14	2.97±0.07
	R$_{eff}$/4	1.16±0.43	1.64±0.16	3.08±0.09	2.66±0.06	1.88±0.09	2.64±0.04
	R$_{eff}$/2	0.66±0.55	1.83±0.08	3.16±0.11	2.41±0.11	1.64±0.24	2.53±0.09
	R$_{eff}$	1.36±0.82	1.58±0.13	3.23±0.17	2.37±0.17	1.09±0.53	2.37±0.20
UGC12127	R$_{eff}$/8	0.44±0.34	1.77±0.13	3.93±0.11	2.85±0.12	*2.39±0.27*	*3.21±0.10*
	R$_{eff}$/4	2.57±0.25	1.58±0.11	3.91±0.10	2.11±0.15	2.10±0.20	2.87±0.09
	R$_{eff}$/2	1.48±0.36	1.76±0.09	3.54±0.10	2.53±0.12	1.76±0.38	2.76±0.13

Table AII

		NaD	TiO1 [10^{-2}]	TiO2 [10^{-2}]	CaH1 [10^{-2}]
NGC0499	$R_{eff}/8$	4.85±0.11	4.46±0.21	9.15±0.29	-0.68±0.27
	$R_{eff}/4$	4.37±0.03	3.95±0.12	8.96±0.24	-0.74±0.22
	$R_{eff}/2$	4.01±0.07	3.77±0.14	8.00±0.35	-1.01±0.27
	R_{eff}	3.58±0.11	3.91±0.16	7.73±0.23	-0.66±0.24
NGC1349	$R_{eff}/8$	3.61±0.12	2.89±0.23	7.77±0.20	*0.50±0.53*
	$R_{eff}/4$	3.13±0.11	2.86±0.16	7.40±0.18	-0.84±0.37
	$R_{eff}/2$	2.68±0.19	2.42±0.16	6.55±0.17	-0.50±0.53
	R_{eff}	2.07±0.21	2.03±0.12	5.56±0.18	-0.97±0.58
NGC5966	$R_{eff}/8$	3.12±0.07	2.69±0.18	7.38±0.14	-0.57±0.13
	$R_{eff}/4$	2.69±0.15	2.66±0.14	6.96±0.15	-1.01±0.20
	$R_{eff}/2$	2.52±0.13	2.89±0.10	6.78±0.16	-0.23±0.17
	R_{eff}	2.34±0.14	2.62±0.11	6.14±0.14	-1.17±0.17
NGC6020	$R_{eff}/8$	3.83±0.02	2.61±0.14	8.51±0.22	-0.27±0.20
	$R_{eff}/4$	3.03±0.07	2.68±0.15	7.10±0.23	-0.36±0.28
	$R_{eff}/2$	2.81±0.15	2.98±0.12	6.95±0.21	-0.15±0.26
	R_{eff}	2.46±0.11	3.39±0.16	*5.31±0.44*	-0.66±0.20
NGC6125	$R_{eff}/8$	4.32±0.03	3.10±0.27	8.19±0.24	-0.61±0.34
	$R_{eff}/4$	3.67±0.07	3.40±0.17	7.41±0.18	-0.12±0.22
	$R_{eff}/2$	3.14±0.07	2.93±0.12	6.82±0.14	-0.84±0.32
	R_{eff}	2.75±0.07	3.04±0.07	6.69±0.16	-0.81±0.28
NGC6146	$R_{eff}/8$	4.02±0.03	3.52±0.17	7.48±0.17	*-1.57±0.35*
	$R_{eff}/4$	3.62±0.03	3.83±0.22	7.07±0.13	-1.15±0.17
	$R_{eff}/2$	3.18±0.03	2.83±0.21	7.08±0.15	-1.46±0.11
	R_{eff}	2.64±0.06	2.73±0.17	7.12±0.18	-1.37±0.31
NGC6150	$R_{eff}/8$	4.13±0.05	3.74±0.15	7.49±0.12	-1.14±0.18
	$R_{eff}/4$	3.99±0.04	3.64±0.16	7.66±0.18	-1.47±0.31
	$R_{eff}/2$	3.69±0.06	3.71±0.19	8.16±0.18	-1.49±0.29
	R_{eff}	3.50±0.05	3.17±0.19	7.75±0.14	-1.12±0.06
NGC6173	$R_{eff}/8$	3.70±0.07	2.93±0.30	7.98±0.35	-1.05±0.25
	$R_{eff}/4$	3.00±0.07	2.80±0.14	7.53±0.18	-1.11±0.26
	$R_{eff}/2$	2.66±0.09	2.62±0.18	7.46±0.17	-1.10±0.26
	R_{eff}	2.95±0.12	*1.45±0.80*	8.47±1.18	*1.07±0.54*
NGC6338	$R_{eff}/8$	4.03±0.19	*2.05±0.73*	8.22±0.38	*-3.62±1.12*
	$R_{eff}/4$	3.78±0.07	3.49±0.27	8.22±0.31	-2.00±0.47
	$R_{eff}/2$	3.50±0.05	3.29±0.22	7.22±0.24	-1.20±0.31
	R_{eff}	3.36±0.15	3.26±0.26	6.32±0.30	-1.50±0.48
NGC6411	$R_{eff}/8$	2.91±0.10	2.33±0.21	7.41±0.29	-0.24±0.16
	$R_{eff}/4$	2.90±0.07	1.63±0.29	7.57±0.25	-0.62±0.22
	$R_{eff}/2$	2.51±0.09	2.30±0.15	6.38±0.23	-0.37±0.19
	R_{eff}	2.46±0.10	-0.35±0.79	-16.5±3.85	-5.82±6.84
NGC6515	$R_{eff}/8$	3.59±0.10	3.47±0.17	6.57±0.17	-0.54±0.38
	$R_{eff}/4$	2.82±0.08	3.35±0.16	6.52±0.14	-0.71±0.30
	$R_{eff}/2$	2.48±0.09	2.80±0.10	5.97±0.17	-0.93±0.34
	R_{eff}	2.31±0.13	3.40±0.16	6.81±0.18	-0.64±0.44

		NaD	TiO1 [10^{-2}]	TiO2 [10^{-2}]	CaH1 [10^{-2}]
NGC7194	$R_{eff}/8$	4.17±0.05	4.17±0.28	8.23±0.25	-1.84±0.51
	$R_{eff}/4$	3.93±0.04	4.32±0.25	7.66±0.19	-0.93±0.36
	$R_{eff}/2$	3.72±0.04	2.86±0.19	7.62±0.20	-1.50±0.30
	R_{eff}	3.57±0.09	2.99±0.16	8.14±0.30	*-2.83±0.58*
NGC7562	$R_{eff}/8$	3.98±0.08	1.87±0.46	9.29±0.35	-0.59±0.26
	$R_{eff}/4$	3.69±0.08	2.01±0.38	8.84±0.32	-0.47±0.21
	$R_{eff}/2$	3.60±0.09	2.51±0.32	8.48±0.33	-0.05±0.28
	R_{eff}	3.43±0.08	2.31±0.26	7.70±0.33	0.01±0.29
UGC05771	$R_{eff}/8$	3.68±0.05	3.95±0.11	7.58±0.16	-0.86±0.19
	$R_{eff}/4$	3.47±0.11	3.84±0.17	7.17±0.18	-0.58±0.13
	$R_{eff}/2$	3.04±0.08	3.97±0.18	7.15±0.22	-0.88±0.27
	R_{eff}	2.64±0.11	2.80±0.08	6.08±0.14	-0.49±0.22
UGC10693	$R_{eff}/8$	4.05±0.08	3.74±0.25	7.82±0.25	-0.62±0.33
	$R_{eff}/4$	3.16±0.07	3.50±0.17	6.86±0.16	-0.87±0.17
	$R_{eff}/2$	2.84±0.07	2.83±0.14	7.20±0.16	-0.81±0.17
	R_{eff}	2.77±0.09	2.95±0.17	7.42±0.41	-1.38±0.30
UGC10695	$R_{eff}/8$	4.25±0.03	3.29±0.11	7.01±0.14	-0.85±0.31
	$R_{eff}/4$	3.00±0.08	2.81±0.10	6.79±0.14	-0.65±0.25
	$R_{eff}/2$	2.34±0.14	3.40±0.14	6.69±0.20	-1.02±0.28
	R_{eff}	2.29±0.20	*2.27±0.22*	7.81±0.42	*-1.57±0.39*
UGC12127	$R_{eff}/8$	3.94±0.08	3.90±0.24	7.70±0.26	-1.10±0.32
	$R_{eff}/4$	3.05±0.07	3.59±0.15	7.38±0.23	-1.40±0.44
	$R_{eff}/2$	2.90±0.05	2.82±0.18	7.49±0.20	*-1.91±0.22*

Table AIII

		x	[M/H]	[α/Fe]	[Na/Fe]	t (Gyr)
NGC0499	$R_{eff}/8$	2.92±0.12	-0.25±0.04	N/A	0.51±0.22	11.97±1.13
	$R_{eff}/4$	2.95±0.31	0.07±0.16	0.20±0.10	0.18±0.24	10.50±1.61
	$R_{eff}/2$	1.92±0.25	-0.37±0.06	-0.24±0.07	0.47±0.07	12.07±0.97
	R_{eff}	2.58±0.49	-0.27±0.12	0.22±0.11	0.42±0.19	9.49±2.06
NGC1349	$R_{eff}/8$	2.04±0.55	-0.22±0.09	0.18±0.10	0.11±0.14	11.19±2.73
	$R_{eff}/4$	2.09±0.26	-0.34±0.04	0.30±0.08	0.14±0.05	10.91±1.53
	$R_{eff}/2$	1.88±0.15	-0.50±0.08	0.04±0.19	0.18±0.13	8.74±2.07
	R_{eff}	1.71±0.17	-0.70±0.21	-0.14±0.05	0.01±0.10	9.77±1.82
NGC5966	$R_{eff}/8$	2.33±0.21	-0.36±0.12	-0.10±0.79	0.35±0.04	9.33±1.44
	$R_{eff}/4$	1.92±0.15	-0.45±0.04	0.11±0.05	0.13±0.07	9.86±0.78
	$R_{eff}/2$	2.10±0.14	-0.46±0.04	-0.02±0.05	0.15±0.05	9.93±0.73
	R_{eff}	1.69±0.16	N/A	0.02±0.05	0.15±0.04	9.99±0.69
NGC6020	$R_{eff}/8$	3.31±0.51	-0.07±0.10	-0.17±0.07	0.15±0.04	8.20±1.19
	$R_{eff}/4$	2.03±0.29	-0.35±0.04	0.20±0.07	0.19±0.11	7.76±1.55
	$R_{eff}/2$	2.21±0.20	-0.69±0.20	0.01±0.24	0.25±0.05	9.86±0.81
	R_{eff}	2.51±0.23	-0.82±0.29	0.14±0.06	0.15±0.04	7.77±1.15
NGC6125	$R_{eff}/8$	3.41±0.13	0.02±0.13	-0.08±0.07	0.12±0.12	4.72±1.51
	$R_{eff}/4$	2.45±0.37	-0.20±0.08	0.08±0.06	0.36±0.08	9.20±1.80
	$R_{eff}/2$	2.06±0.30	-0.29±0.08	0.20±0.12	0.34±0.05	7.20±1.98
	R_{eff}	1.88±0.13	-0.45±0.04	0.11±0.05	0.25±0.04	9.76±1.03
NGC6146	$R_{eff}/8$	2.62±0.32	-0.35±0.04	-0.52±0.26	0.48±0.10	7.22±1.71
	$R_{eff}/4$	3.13±0.08	0.05±0.04	0.28±0.03	0.15±0.04	N/A
	$R_{eff}/2$	1.76±0.13	-0.05±0.04	0.02±0.02	0.04±0.09	4.00±0.68
	R_{eff}	2.12±0.42	-0.35±0.10	0.08±0.10	-0.12±0.11	7.91±1.93
NGC6150	$R_{eff}/8$	1.96±0.14	-0.35±0.03	N/A	0.50±0.07	9.99±0.71
	$R_{eff}/4$	2.23±0.38	-0.32±0.12	0.15±0.19	0.40±0.08	11.43±1.54
	$R_{eff}/2$	2.30±0.19	-0.24±0.04	0.25±0.05	0.13±0.07	11.95±1.29
	R_{eff}	2.21±0.49	-0.21±0.11	0.31±0.11	0.15±0.03	11.67±2.22
NGC6173	$R_{eff}/8$	2.74±0.34	-0.54±0.09	-0.15±0.05	0.50±0.07	10.43±1.36
	$R_{eff}/4$	2.47±0.52	-0.18±0.09	-0.04±0.07	-0.29±0.23	7.91±2.43
	$R_{eff}/2$	2.05±0.30	-0.31±0.07	0.00±0.06	-0.13±0.10	10.90±1.67
	R_{eff}	2.65±0.58	-0.13±0.17	0.22±0.10	-0.02±0.20	7.27±3.60
NGC6338	$R_{eff}/8$	2.69±0.50	-0.10±0.11	0.24±0.12	0.13±0.25	8.97±3.15
	$R_{eff}/4$	2.22±0.32	-0.06±0.09	0.06±0.06	-0.08±0.12	11.66±1.55
	$R_{eff}/2$	1.98±0.32	-0.25±0.04	0.18±0.06	0.19±0.14	9.68±1.31
	R_{eff}	1.88±0.21	-0.47±0.07	-0.19±0.07	0.45±0.10	7.47±2.16
NGC6411	$R_{eff}/8$	2.78±0.26	-0.27±0.06	-0.05±0.04	-0.03±0.08	6.53±1.36
	$R_{eff}/4$	2.31±0.26	-0.35±0.04	0.12±0.06	0.16±0.06	6.03±0.70
	$R_{eff}/2$	1.91±0.21	-0.34±0.04	-0.04±0.04	-0.05±0.05	6.03±0.70
	R_{eff}	1.96±0.23	-0.65±0.19	-0.07±0.09	0.14±0.07	9.58±1.60
NGC6515	$R_{eff}/8$	1.79±0.12	-0.45±0.03	N/A	0.46±0.08	6.01±0.68
	$R_{eff}/4$	1.90±0.13	-0.45±0.04	0.08±0.05	0.17±0.10	9.89±0.76
	$R_{eff}/2$	1.82±0.12	-0.36±0.04	-0.02±0.02	0.04±0.08	6.25±1.72
	R_{eff}	2.27±0.22	-0.50±0.07	0.16±0.10	0.12±0.07	8.00±2.03

		x	[M/H]	[α/Fe]	[Na/Fe]	t (Gyr)
NGC7194	$R_{eff}/8$	1.88±0.49	-0.33±0.16	N/A	0.47±0.08	11.80±3.30
	$R_{eff}/4$	2.92±0.38	-0.15±0.04	0.16±0.04	0.18±0.12	8.33±1.22
	$R_{eff}/2$	1.84±0.13	-0.25±0.04	0.08±0.04	0.25±0.07	12.20±0.88
	R_{eff}	2.47±0.39	-0.14±0.07	-0.11±0.07	-0.04±0.12	11.12±3.13
NGC7562	$R_{eff}/8$	3.39±0.09	-0.05±0.04	-0.02±0.02	0.05±0.09	6.05±0.72
	$R_{eff}/4$	2.57±0.64	-0.10±0.11	0.03±0.10	-0.11±0.08	8.01±3.18
	$R_{eff}/2$	3.23±0.21	-0.16±0.04	0.27±0.05	0.30±0.13	6.26±1.34
	R_{eff}	2.39±0.52	-0.20±0.07	0.16±0.10	0.06±0.11	8.15±2.11
UGC05771	$R_{eff}/8$	3.19±0.09	-0.05±0.05	0.37±0.05	0.12±0.08	4.07±0.92
	$R_{eff}/4$	2.71±0.37	-0.16±0.10	0.15±0.09	0.05±0.13	6.61±1.82
	$R_{eff}/2$	2.52±0.44	-0.33±0.07	0.23±0.08	0.17±0.14	5.86±1.61
	R_{eff}	1.71±0.16	-0.45±0.04	0.07±0.05	0.16±0.06	6.04±0.70
UGC10693	$R_{eff}/8$	3.21±0.31	-0.17±0.10	0.19±0.14	0.26±0.16	4.67±2.83
	$R_{eff}/4$	2.02±0.30	-0.31±0.07	0.31±0.12	0.15±0.04	9.12±1.68
	$R_{eff}/2$	2.24±0.16	-0.37±0.06	0.03±0.05	0.13±0.07	8.26±1.25
	R_{eff}	1.93±0.28	-0.34±0.06	0.02±0.05	0.02±0.10	10.01±1.15
UGC10695	$R_{eff}/8$	2.13±0.38	-0.24±0.07	-0.14±0.24	0.35±0.05	8.41±2.15
	$R_{eff}/4$	2.29±0.34	-0.27±0.07	-0.09±0.04	-0.05±0.11	7.71±1.81
	$R_{eff}/2$	2.25±0.28	-0.38±0.07	0.07±0.11	-0.01±0.11	6.91±1.76
	R_{eff}	2.30±0.45	-0.46±0.09	0.10±0.15	-0.04±0.15	10.61±2.34
UGC12127	$R_{eff}/8$	2.89±0.63	0.03±0.12	0.14±0.10	0.06±0.12	5.43±2.97
	$R_{eff}/4$	1.96±0.34	-0.35±0.04	0.37±0.04	0.15±0.04	11.65±1.47
	$R_{eff}/2$	2.52±0.50	-0.27±0.09	0.01±0.06	-0.08±0.22	8.10±1.99

Appendix B

In this Appendix we present the spectra of the galaxies at every used Lick/IDS wavelength interval. Every image includes a table with the measured values of the indices. Every plot consists of four lines normalized over their respective intervals. The $R_{eff}/8$, $R_{eff}/4$, $R_{eff}/2$, and R_{eff} are plotted with a solid, dashed, dashed-dotted, and dotted line respectively. The red vertical dotted lines represents the index band that defined the Lick/IDS index. Cursive numbers in the table are outliers and are discussed in Section 5.2. The order of the figures is as follows:

I NGC0499

II NGC1349

III NGC5966

IV NGC6020

V NGC6125

VI NGC6146

VII NGC6150

VIII NGC6173

IX NGC6338

X NGC6411

XI NGC6515

XII NGC7194

XIII NGC7562

XIV UGC05771

XV UGC10693

XVI UGC10695

XVII UGC12127

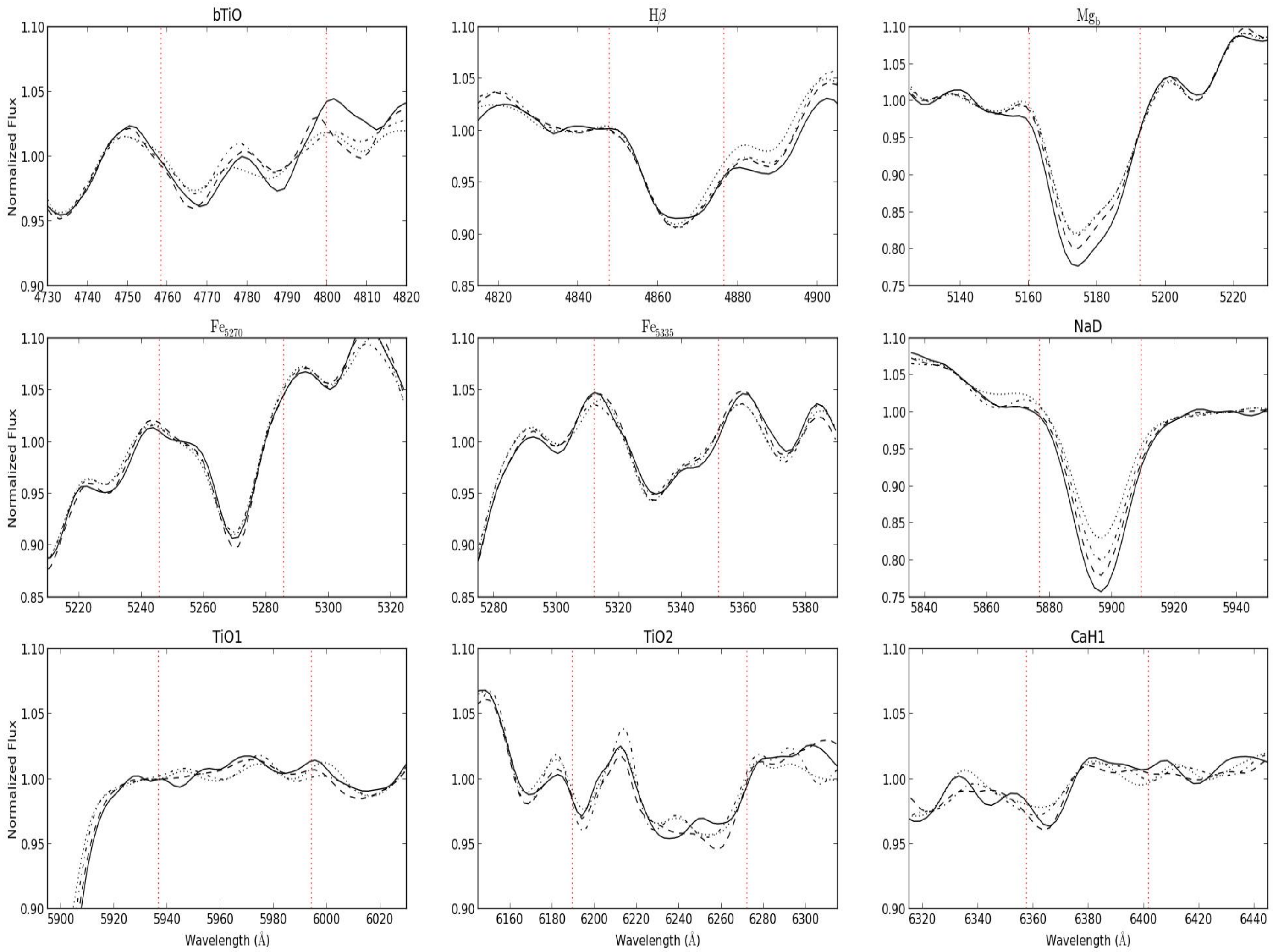

Figure B.I: NGC0499

	bTiO	$H\beta$	Mg_b	Fe_{5270}	Fe_{5335}	NaD	TiO1	TiO2	CaH1
$R_{eff}/8$	2.5994e-02	1.1425e+00	4.7453e+00	2.2049e+00	2.1145e+00	4.8510e+00	4.4630e-02	9.1510e-02	-6.8136e-03
$R_{eff}/4$	1.4667e-02	1.3388e+00	4.2252e+00	2.5214e+00	2.0792e+00	4.3703e+00	3.9530e-02	8.9637e-02	-7.3996e-03
$R_{eff}/2$	7.1048e-03	1.3330e+00	3.8181e+00	2.1629e+00	1.6865e+00	4.0079e+00	3.7690e-02	8.0019e-02	-1.0128e-02
R_{eff}	1.4818e-02	1.3861e+00	3.8216e+00	2.2937e+00	1.8146e+00	3.5792e+00	3.9085e-02	7.7274e-02	-6.5705e-03

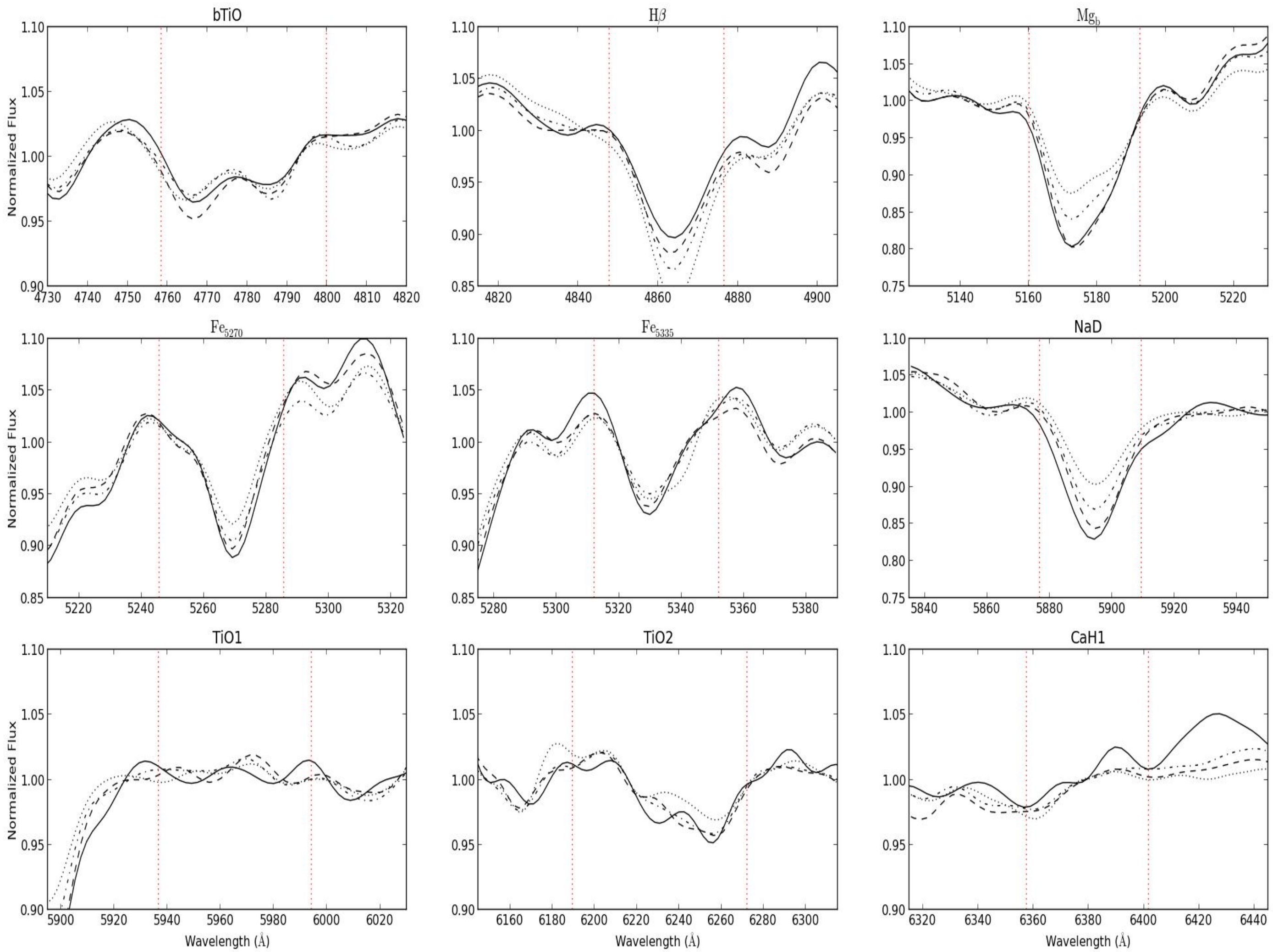

Figure B.II: NGC1349

	bTiO	Hβ	Mg$_b$	Fe$_{5270}$	Fe$_{5335}$	NaD	TiO1	TiO2	CaH1
R$_{eff}$/8	2.3418e-02	1.6751e+00	3.8057e+00	2.9114e+00	2.0002e+00	3.6144e+00	2.8962e-02	7.7734e-02	*5.0163e-03*
R$_{eff}$/4	2.6592e-02	1.6068e+00	3.8695e+00	2.7211e+00	1.3027e+00	3.1305e+00	2.8634e-02	7.4019e-02	-8.3479e-03
R$_{eff}$/2	1.9421e-02	1.9712e+00	3.2297e+00	2.2072e+00	1.3590e+00	2.6762e+00	2.4242e-02	6.5478e-02	-4.9700e-03
R$_{eff}$	1.3905e-02	*2.5465e+00*	2.5491e+00	1.9800e+00	1.4350e+00	2.0740e+00	2.0325e-02	5.5597e-02	-9.6804e-03

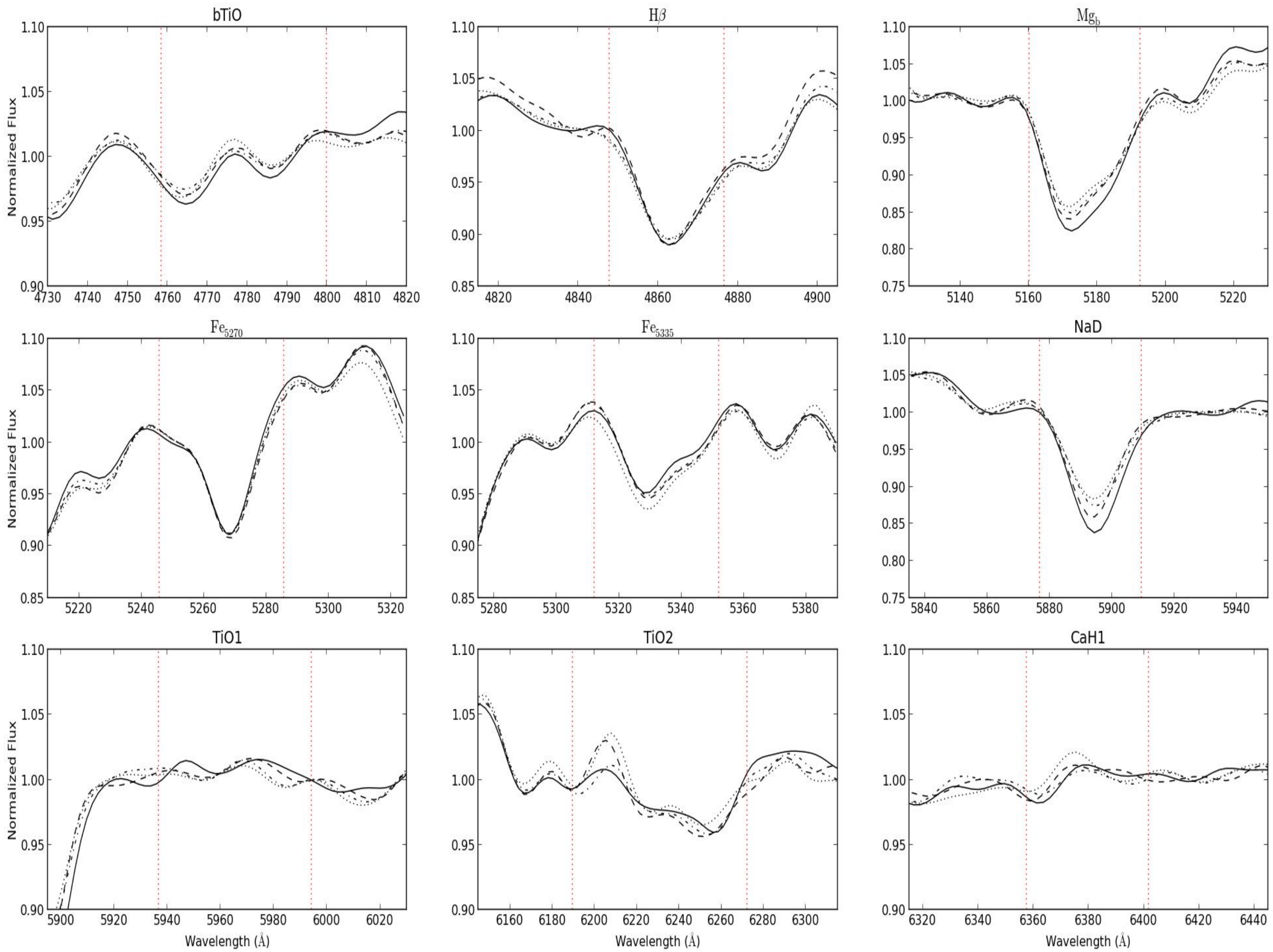

Figure B.III: NGC5966

	bTiO	Hβ	Mg$_b$	Fe$_{5270}$	Fe$_{5335}$	NaD	TiO1	TiO2	CaH1
R$_{eff}$/8	8.6405e-03	1.6096e+00	3.5946e+00	2.0936e+00	1.4304e+00	3.1168e+00	2.6926e-02	7.3770e-02	-5.7297e-03
R$_{eff}$/4	*-4.1292e-03*	1.7333e+00	3.1754e+00	2.2943e+00	1.7830e+00	2.6920e+00	2.6627e-02	6.9601e-02	-1.0079e-02
R$_{eff}$/2	*-3.8136e-04*	1.6998e+00	3.0433e+00	2.1766e+00	1.6394e+00	2.5197e+00	2.8906e-02	6.7779e-02	-2.2898e-03
R$_{eff}$	*-7.5905e-03*	1.6602e+00	2.8330e+00	2.0363e+00	1.6887e+00	2.3388e+00	2.6263e-02	6.1408e-02	-1.1725e-02

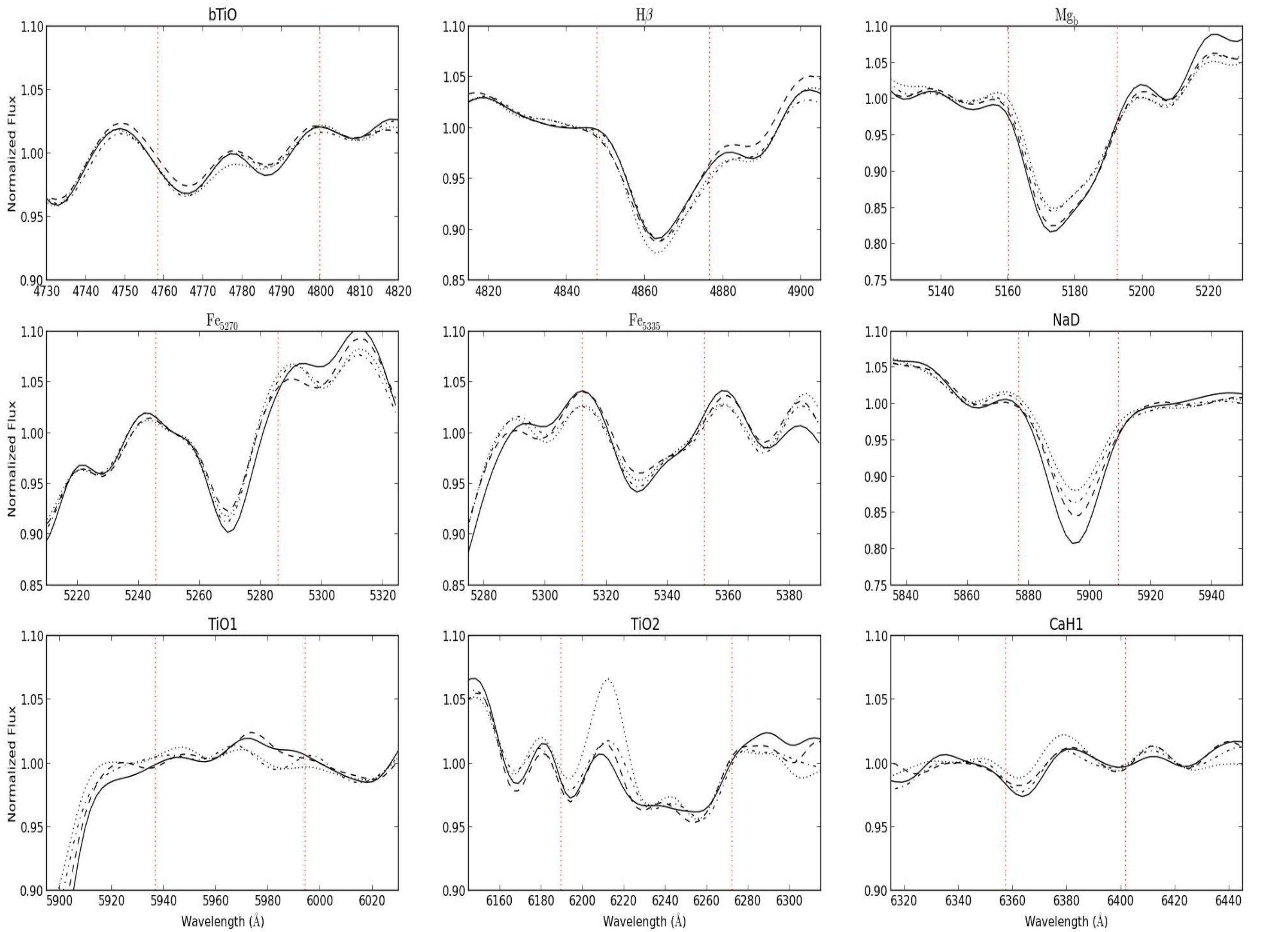

Figure B.IV: NGC6020

	bTiO	Hβ	Mg$_b$	Fe$_{5270}$	Fe$_{5335}$	NaD	TiO1	TiO2	CaH1
R$_{eff}$/8	1.4282e-02	1.5899e+00	3.7495e+00	2.6258e+00	1.9394e+00	3.8291e+00	2.6081e-02	8.5094e-02	-2.6774e-03
R$_{eff}$/4	7.4568e-03	1.8388e+00	3.6503e+00	1.9352e+00	1.6693e+00	3.0272e+00	2.6798e-02	7.0946e-02	-3.6308e-03
R$_{eff}$/2	1.1780e-02	1.7261e+00	3.1025e+00	2.0871e+00	1.4968e+00	2.8054e+00	2.9804e-02	6.9536e-02	-1.5036e-03
R$_{eff}$	1.2610e-02	1.8804e+00	3.1122e+00	1.8098e+00	1.3959e+00	2.4545e+00	3.3876e-02	*5.3142e-02*	-6.6229e-03

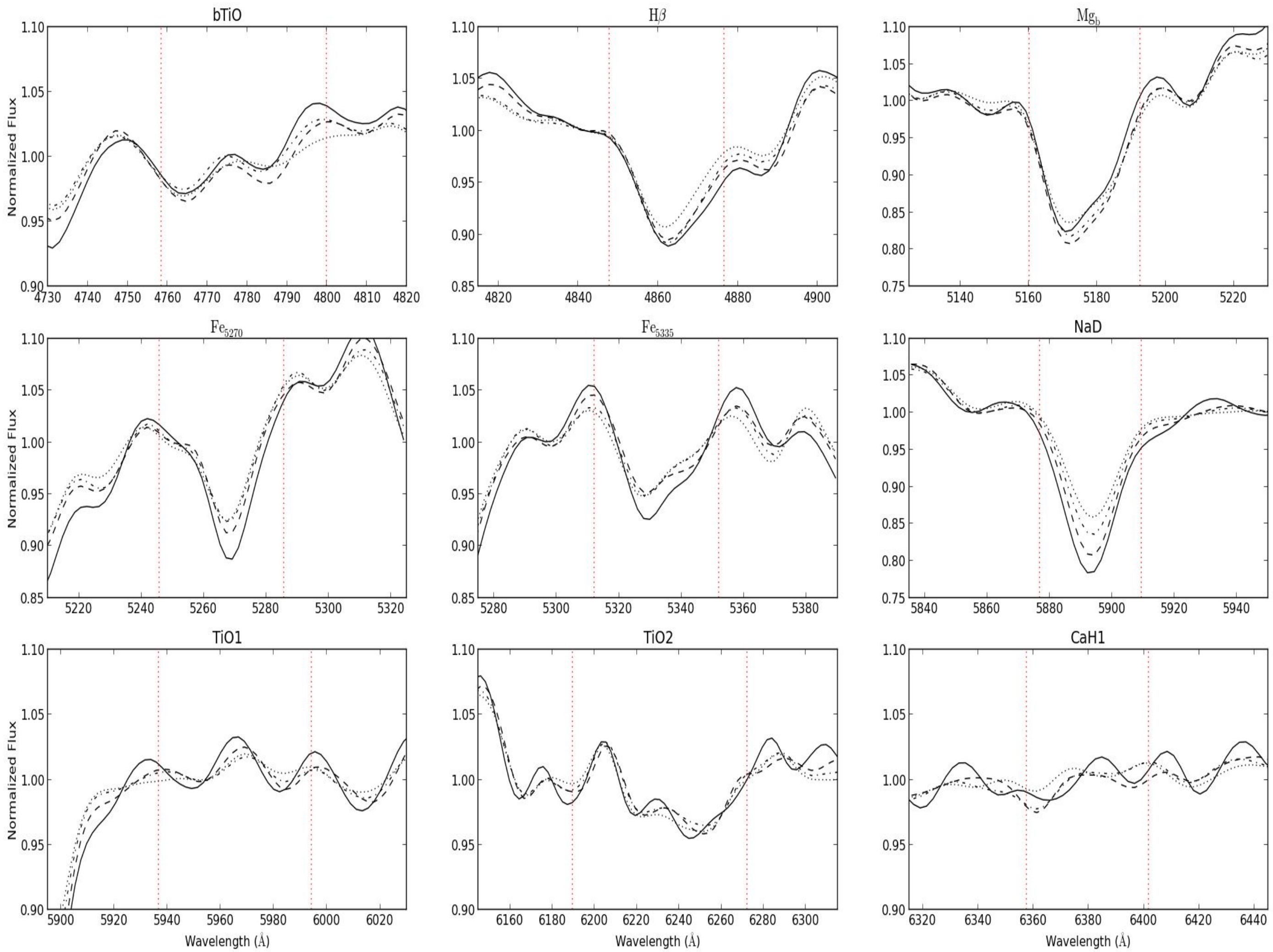

Figure B.V: NGC6125

	bTiO	Hβ	Mg$_b$	Fe$_{5270}$	Fe$_{5335}$	NaD	TiO1	TiO2	CaH1
R$_{eff}$/8	*-5.3273e-03*	1.7442e+00	3.3227e+00	2.8390e+00	2.5011e+00	4.3218e+00	3.0994e-02	8.1867e-02	-6.1339e-03
R$_{eff}$/4	9.7901e-03	1.5355e+00	3.7635e+00	2.0618e+00	1.7869e+00	3.6710e+00	3.4019e-02	7.4137e-02	-1.2176e-03
R$_{eff}$/2	3.9749e-04	1.6541e+00	3.6227e+00	1.8986e+00	1.4949e+00	3.1431e+00	2.9259e-02	6.8238e-02	-8.3768e-03
R$_{eff}$	8.0018e-03	1.4036e+00	3.3195e+00	1.8372e+00	1.2697e+00	2.7517e+00	3.0416e-02	6.6895e-02	-8.0488e-03

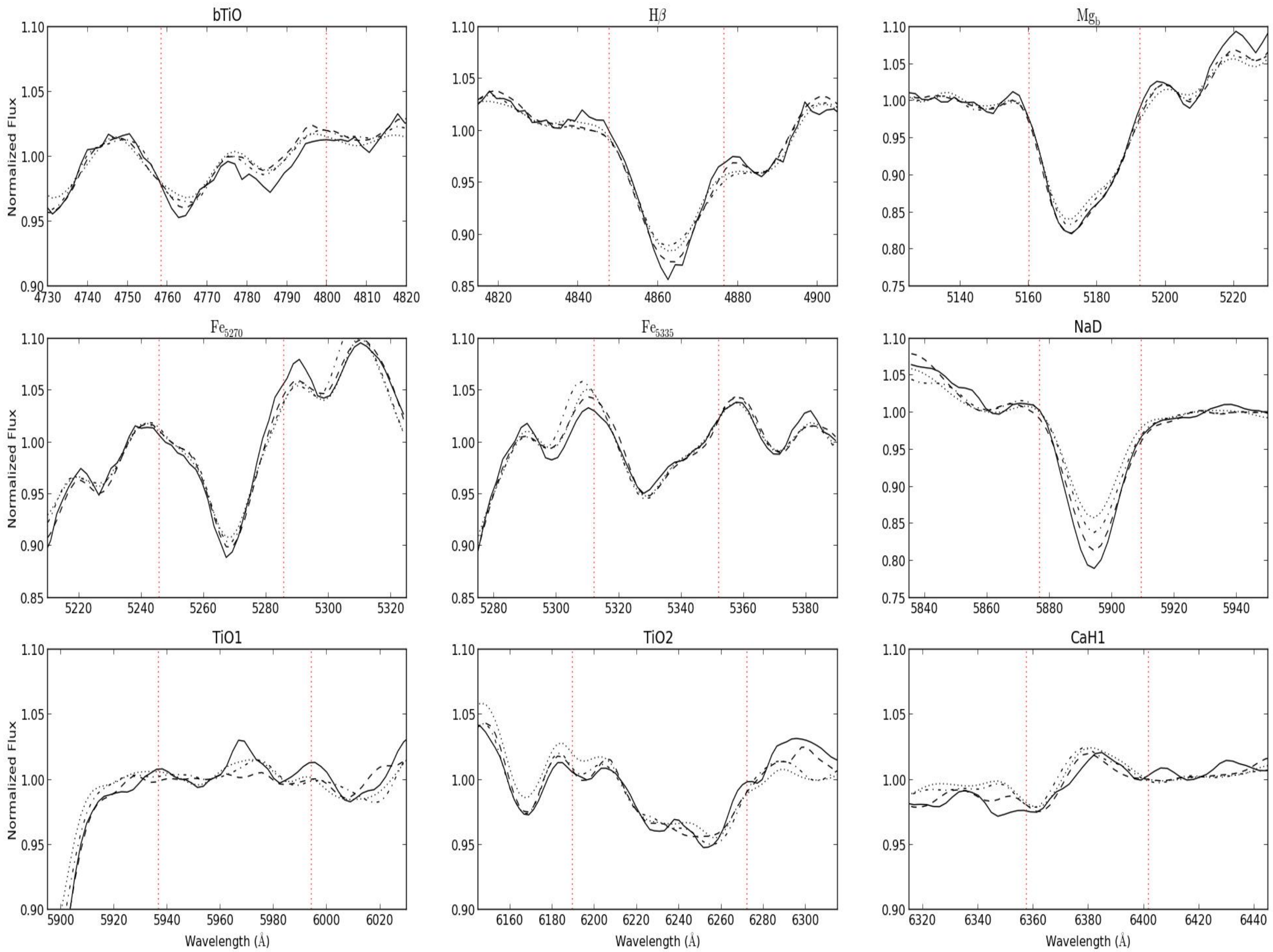

Figure B.VI: NGC6146

	bTiO	Hβ	Mg$_b$	Fe$_{5270}$	Fe$_{5335}$	NaD	TiO1	TiO2	CaH1
R$_{eff}$/8	*1.8666e-02*	1.9188e+00	3.5753e+00	2.4261e+00	1.4352e+00	4.0146e+00	3.5232e-02	7.4819e-02	*-1.5669e-02*
R$_{eff}$/4	2.8629e-03	1.9108e+00	3.6332e+00	2.5141e+00	1.7995e+00	3.6149e+00	3.8266e-02	7.0714e-02	-1.1450e-02
R$_{eff}$/2	5.0417e-03	1.7115e+00	3.4047e+00	2.5280e+00	1.8723e+00	3.1759e+00	2.8277e-02	7.0782e-02	-1.4624e-02
R$_{eff}$	2.0163e-03	1.7232e+00	3.3226e+00	2.4137e+00	1.7127e+00	2.6381e+00	2.7258e-02	7.1179e-02	-1.3698e-02

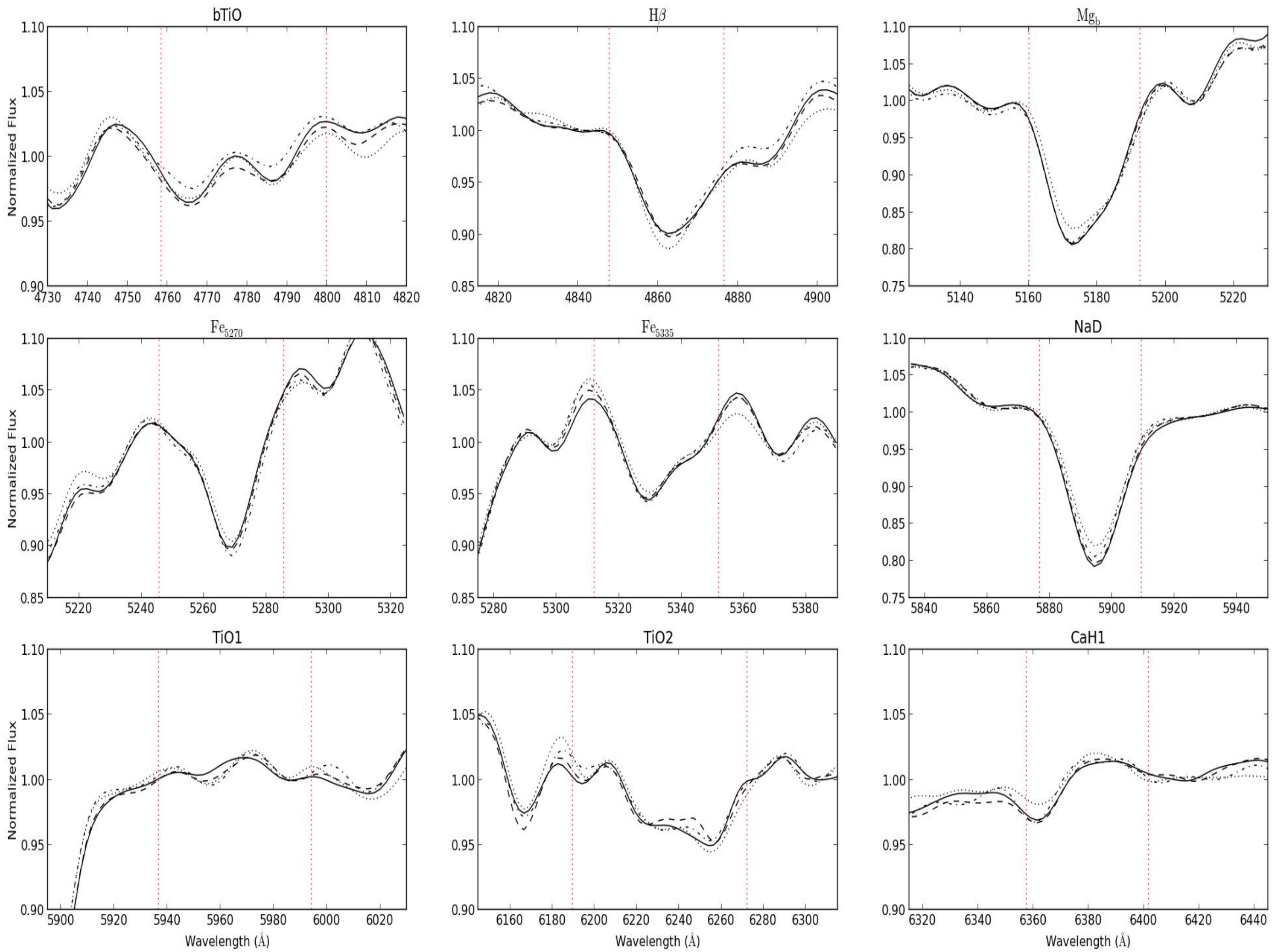

Figure B.VII: NGC6150

	bTiO	Hβ	Mg_b	Fe_{5270}	Fe_{5335}	NaD	TiO1	TiO2	CaH1
$R_{eff}/8$	1.3753e-02	1.5605e+00	3.9022e+00	2.5701e+00	1.8772e+00	4.1317e+00	3.7373e-02	7.4889e-02	-1.1432e-02
$R_{eff}/4$	1.4895e-02	1.5148e+00	3.9003e+00	2.5792e+00	1.9118e+00	3.9935e+00	3.6407e-02	7.6634e-02	-1.4659e-02
$R_{eff}/2$	*7.3347e-04*	1.6869e+00	3.9323e+00	2.7968e+00	1.9688e+00	3.6911e+00	3.7053e-02	8.1553e-02	-1.4919e-02
R_{eff}	1.4683e-02	1.7114e+00	3.6703e+00	2.5599e+00	1.7612e+00	3.5002e+00	3.1692e-02	7.7528e-02	-1.1199e-02

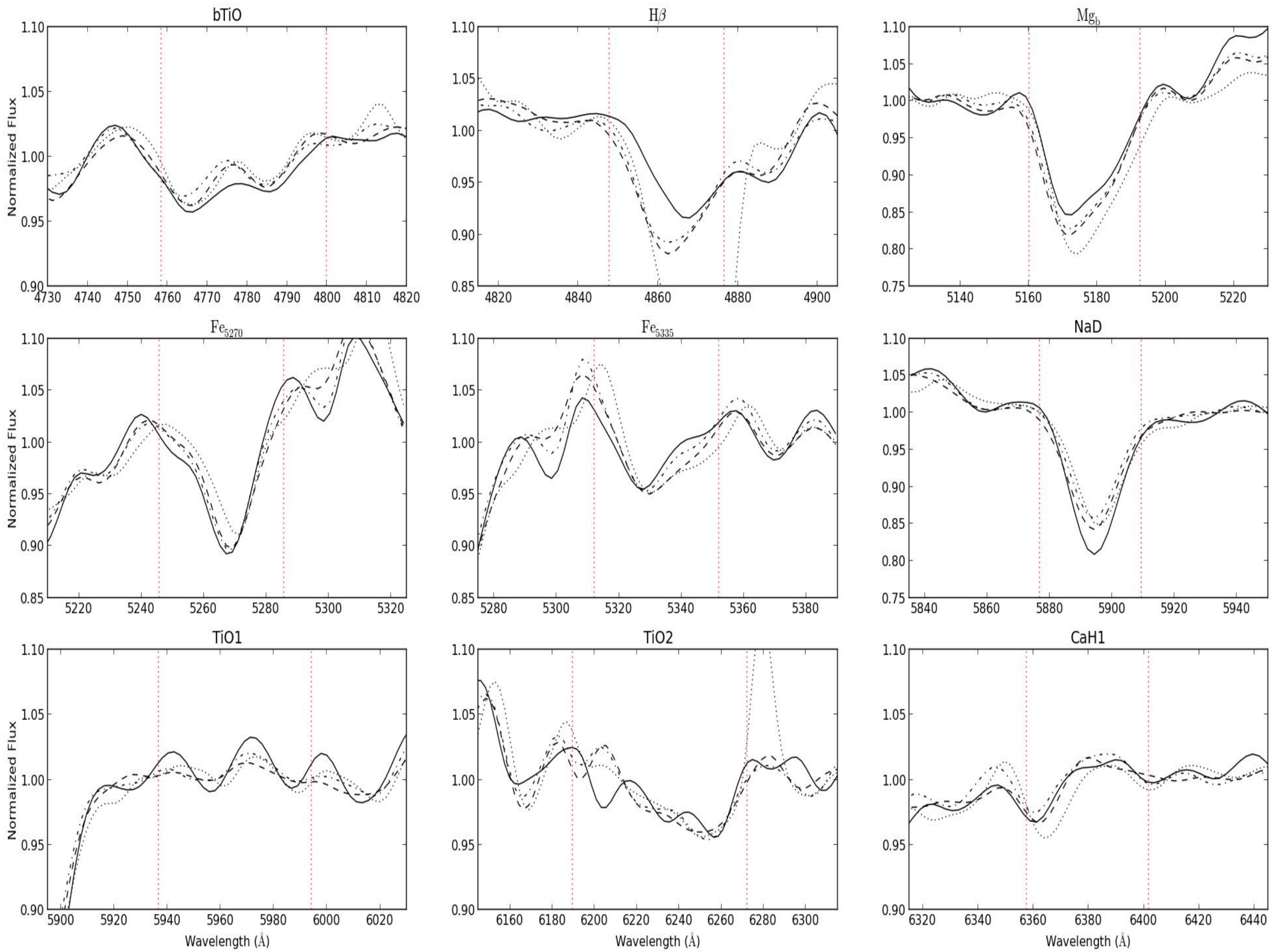

Figure B.VIII: NGC6173

	bTiO	Hβ	Mg$_b$	Fe$_{5270}$	Fe$_{5335}$	NaD	TiO1	TiO2	CaH1
R$_{eff}$/8	3.0363e-02	*9.3277e-01*	3.2022e+00	2.4853e+00	1.1265e+00	3.6949e+00	2.9328e-02	7.9813e-02	-1.0458e-02
R$_{eff}$/4	1.6056e-02	1.8364e+00	3.6100e+00	2.7920e+00	1.8130e+00	2.9978e+00	2.8024e-02	7.5322e-02	-1.1111e-02
R$_{eff}$/2	1.6326e-02	1.6428e+00	3.5261e+00	2.6008e+00	1.9147e+00	2.6630e+00	2.6187e-02	7.4641e-02	-1.1034e-02
R$_{eff}$	1.7894e-02	*4.8960e+00*	4.2393e+00	2.4723e+00	2.2284e+00	2.9526e+00	*1.4539e-02*	8.4654e-02	*1.0726e-02*

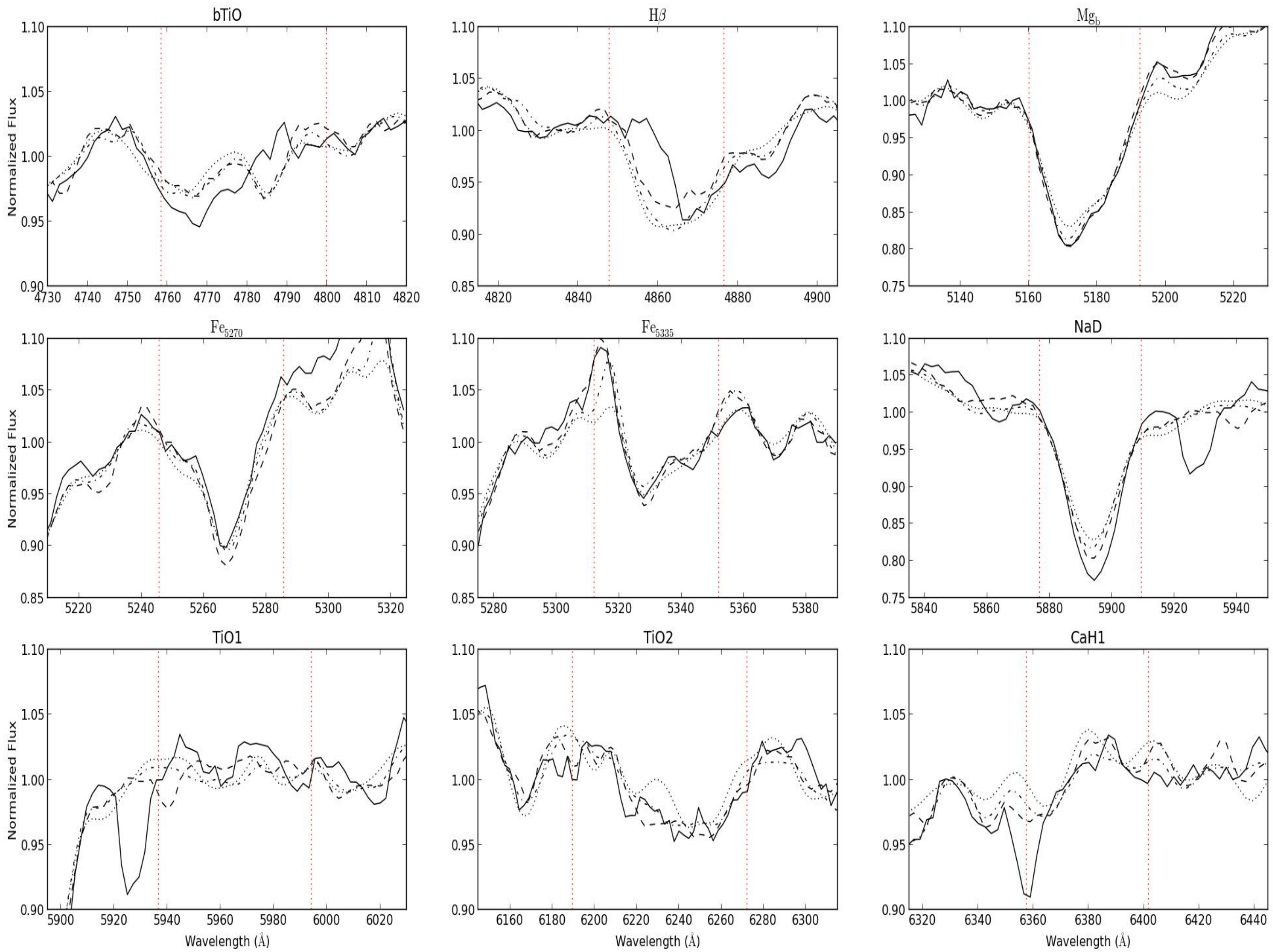

Figure B.IX: NGC6338

	bTiO	Hβ	Mg$_b$	Fe$_{5270}$	Fe$_{5335}$	NaD	TiO1	TiO2	CaH1
R$_{eff}$/8	2.0415e-02	*5.9845e-01*	4.1484e+00	2.7056e+00	2.0788e+00	4.0275e+00	*2.0491e-02*	8.2277e-02	*-3.6221e-02*
R$_{eff}$/4	1.2462e-02	1.2353e+00	4.0450e+00	3.0312e+00	2.1764e+00	3.7769e+00	3.4895e-02	8.2222e-02	-1.9988e-02
R$_{eff}$/2	1.3110e-02	1.6445e+00	3.6686e+00	2.4966e+00	1.5677e+00	3.5035e+00	3.2882e-02	7.2193e-02	-1.2031e-02
R$_{eff}$	3.9835e-03	1.8611e+00	3.3299e+00	2.1787e+00	1.4329e+00	3.3636e+00	3.2595e-02	6.3173e-02	-1.4966e-02

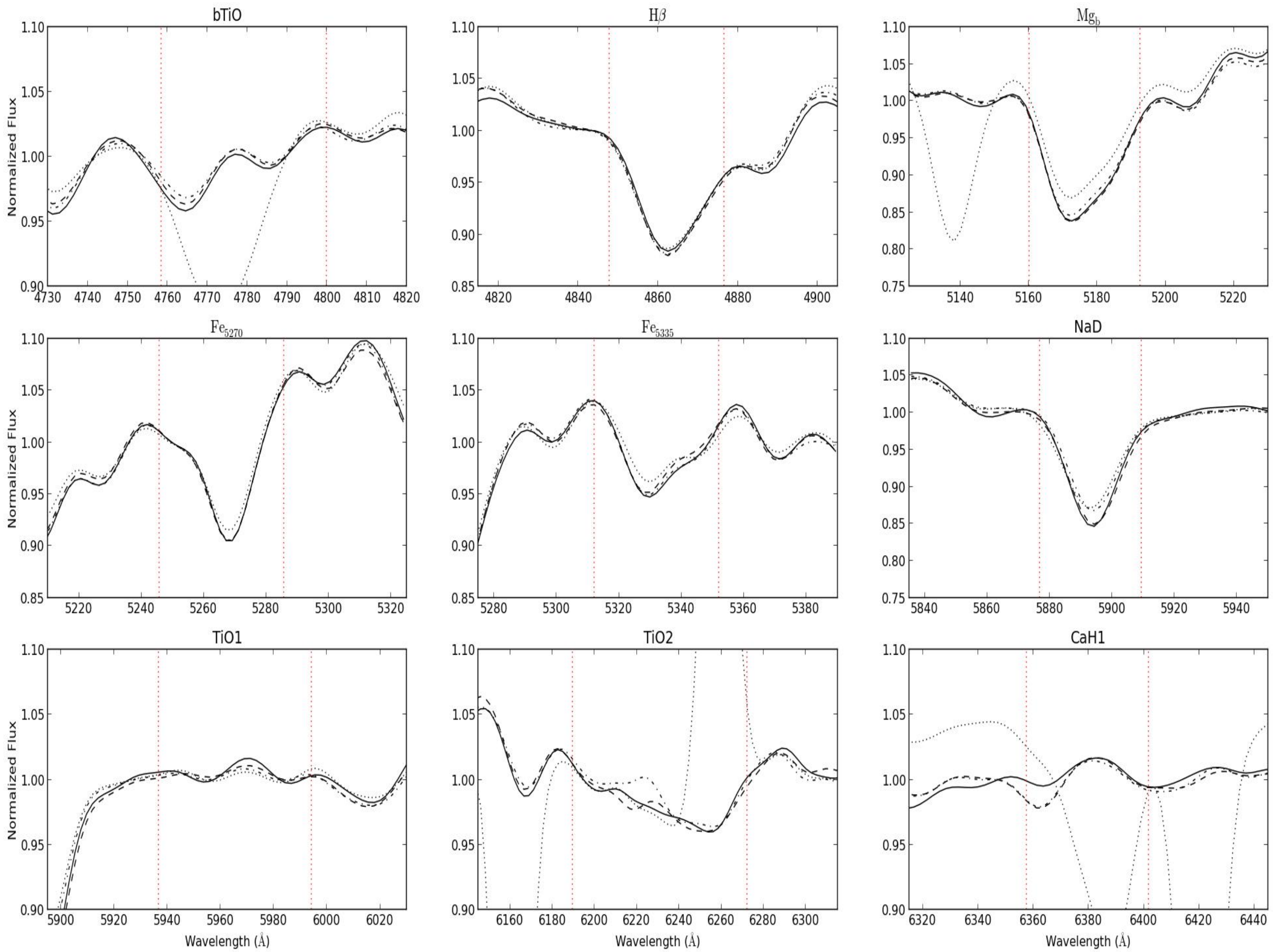

Figure B.X: NGC6411

	bTiO	Hβ	Mg$_b$	Fe$_{5270}$	Fe$_{5335}$	NaD	TiO1	TiO2	CaH1
R$_{eff}$/8	2.8141e-03	1.7010e+00	3.2221e+00	2.3512e+00	1.7279e+00	2.9049e+00	2.3256e-02	7.4140e-02	-2.3474e-03
R$_{eff}$/4	-2.5038e-03	1.8864e+00	3.2350e+00	2.3216e+00	1.4382e+00	2.8946e+00	1.6292e-02	7.5656e-02	-6.2286e-03
R$_{eff}$/2	-4.1212e-03	1.8680e+00	3.0067e+00	2.3203e+00	1.6730e+00	2.5119e+00	2.2961e-02	6.3767e-02	-3.6917e-03
R$_{eff}$	4.8416e-02	1.7685e+00	2.7445e+00	2.0423e+00	1.3893e+00	2.4570e+00	-3.4553e-03	-1.6536e-01	-5.8238e-02

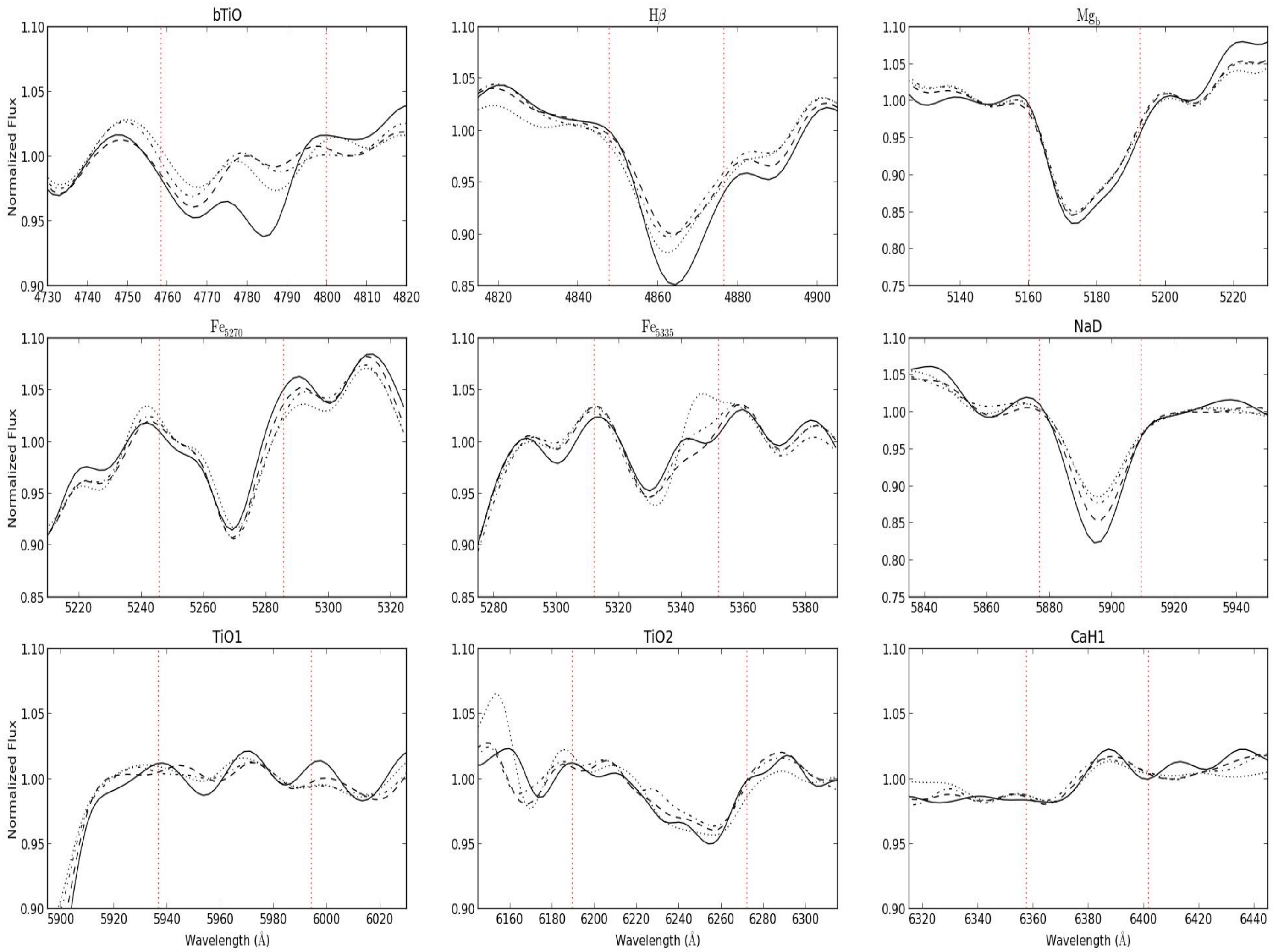

Figure B.XI: NGC6515

	bTiO	$H\beta$	Mg_b	Fe_{5270}	Fe_{5335}	NaD	TiO1	TiO2	CaH1
$R_{eff}/8$	*3.8243e-02*	2.2326e+00	3.5208e+00	2.0590e+00	1.2294e+00	3.5928e+00	3.4657e-02	6.5646e-02	-5.3679e-03
$R_{eff}/4$	9.0692e-03	1.5845e+00	3.1317e+00	2.2191e+00	1.6961e+00	2.8179e+00	3.3460e-02	6.5242e-02	-7.0941e-03
$R_{eff}/2$	1.6592e-02	1.7072e+00	3.0776e+00	2.4265e+00	1.3552e+00	2.4832e+00	2.7994e-02	5.9732e-02	-9.2611e-03
R_{eff}	2.3785e-02	1.9490e+00	3.0960e+00	2.2635e+00	1.1008e+00	2.3117e+00	3.4029e-02	6.8140e-02	-6.4246e-03

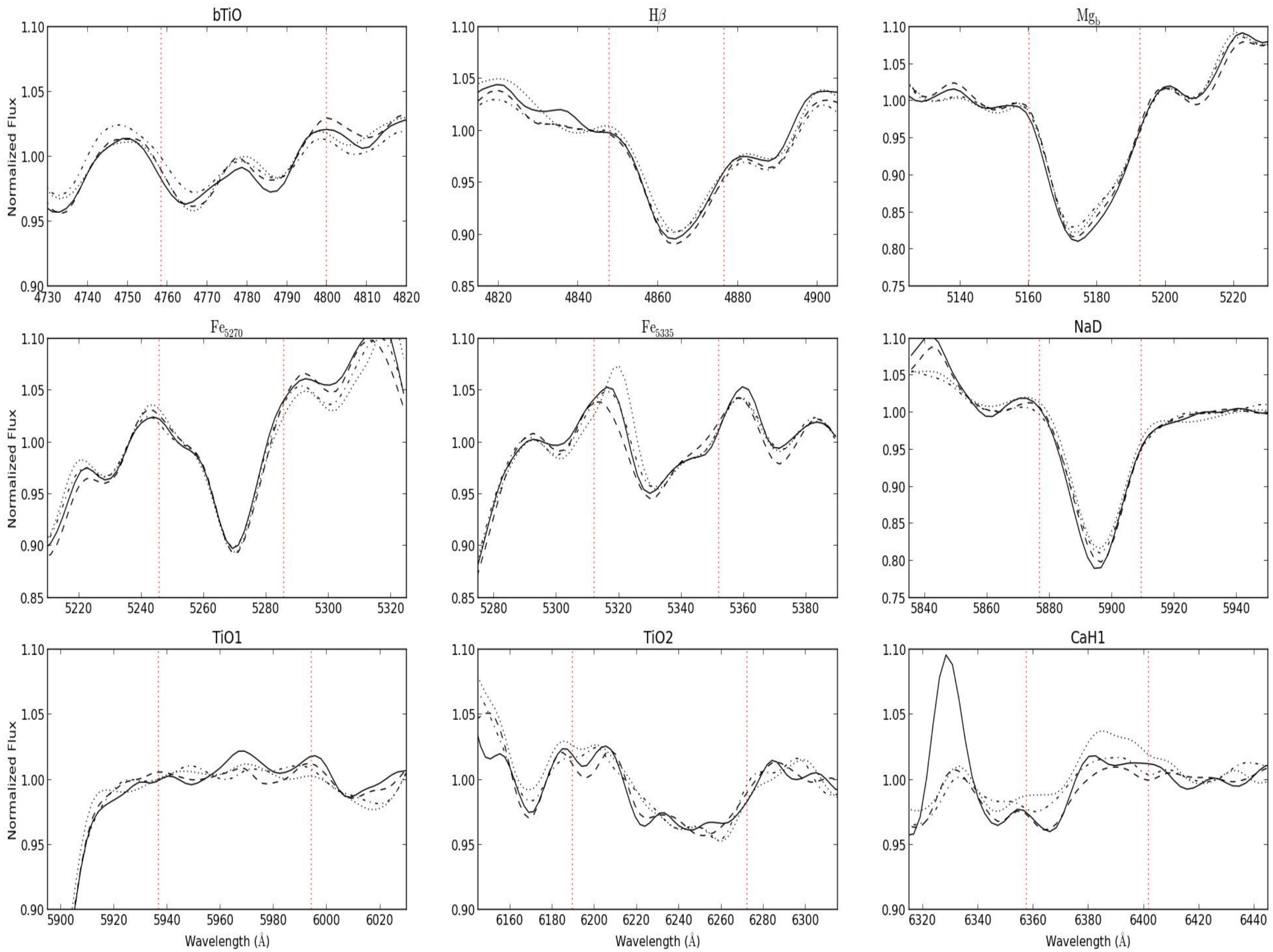

Figure B.XII: NGC7194

	bTiO	Hβ	Mg$_\mathrm{b}$	Fe$_{5270}$	Fe$_{5335}$	NaD	TiO1	TiO2	CaH1
R$_\mathrm{eff}$/8	1.4353e-02	1.6504e+00	4.0034e+00	2.7183e+00	1.9314e+00	4.1731e+00	4.1720e-02	8.2326e-02	-1.8410e-02
R$_\mathrm{eff}$/4	1.4348e-02	1.5910e+00	3.7798e+00	2.8108e+00	1.6703e+00	3.9340e+00	4.3145e-02	7.6619e-02	-9.3372e-03
R$_\mathrm{eff}$/2	1.7958e-02	1.4114e+00	3.6230e+00	2.5281e+00	1.6250e+00	3.7237e+00	2.8553e-02	7.6148e-02	-1.5032e-02
R$_\mathrm{eff}$	8.9532e-03	1.3917e+00	3.6188e+00	2.8306e+00	1.2505e+00	3.5657e+00	2.9920e-02	8.1386e-02	*-2.8280e-02*

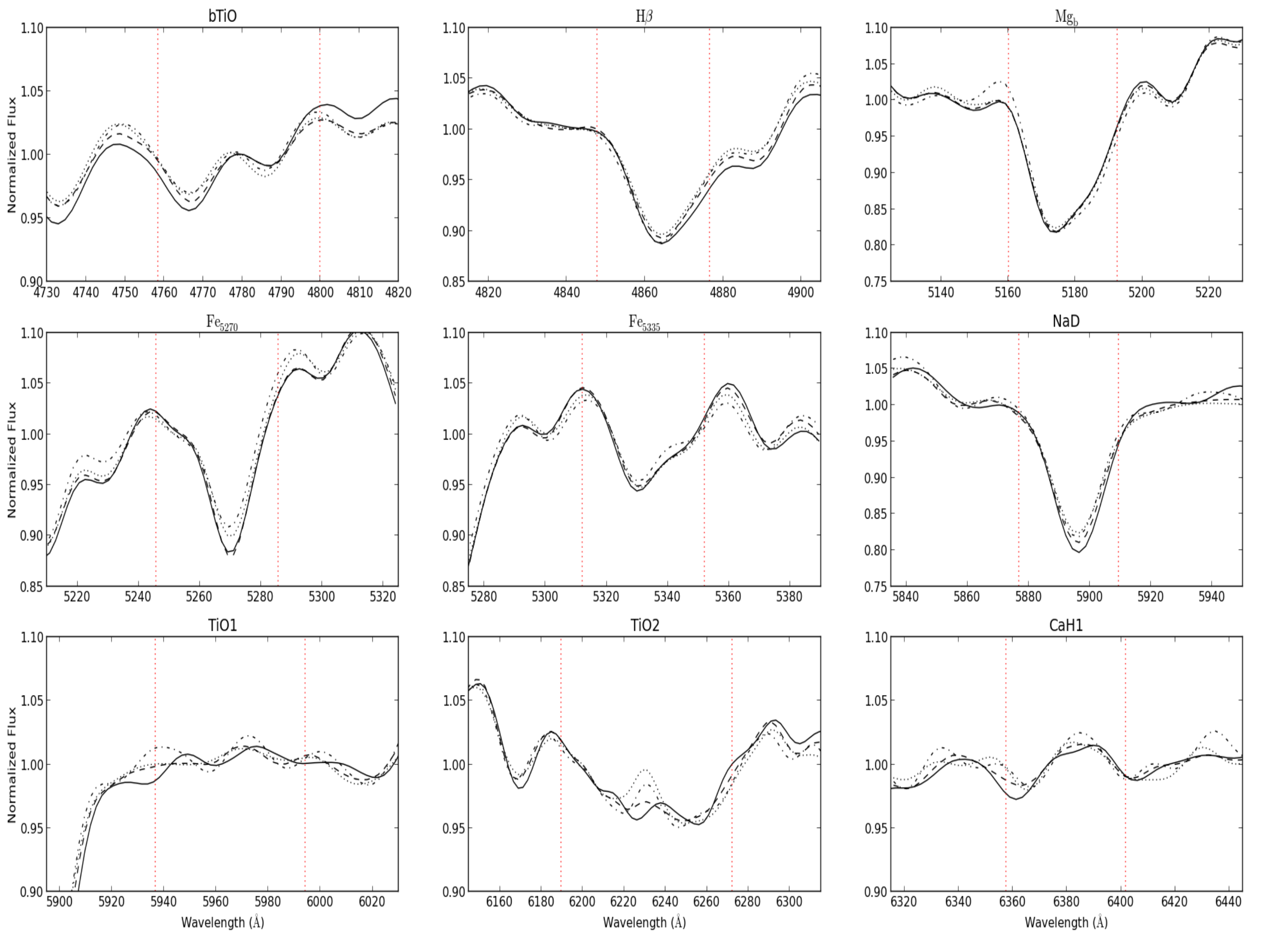

Figure B.XIII: NGC7562

	bTiO	Hβ	Mg_b	Fe_{5270}	Fe_{5335}	NaD	TiO1	TiO2	CaH1
$R_{eff}/8$	7.4583e-03	1.6653e+00	3.8332e+00	2.8703e+00	2.1194e+00	3.9810e+00	1.8687e-02	9.2885e-02	-5.9396e-03
$R_{eff}/4$	7.6906e-03	1.5980e+00	3.8109e+00	2.8109e+00	2.0120e+00	3.6903e+00	2.0084e-02	8.8441e-02	-4.6846e-03
$R_{eff}/2$	8.7272e-03	1.7571e+00	4.0133e+00	2.4006e+00	1.4114e+00	3.5965e+00	2.5105e-02	8.4767e-02	-4.4942e-04
R_{eff}	9.9179e-03	1.6143e+00	3.7396e+00	2.5560e+00	1.8158e+00	3.4247e+00	2.3094e-02	7.6956e-02	1.0847e-04

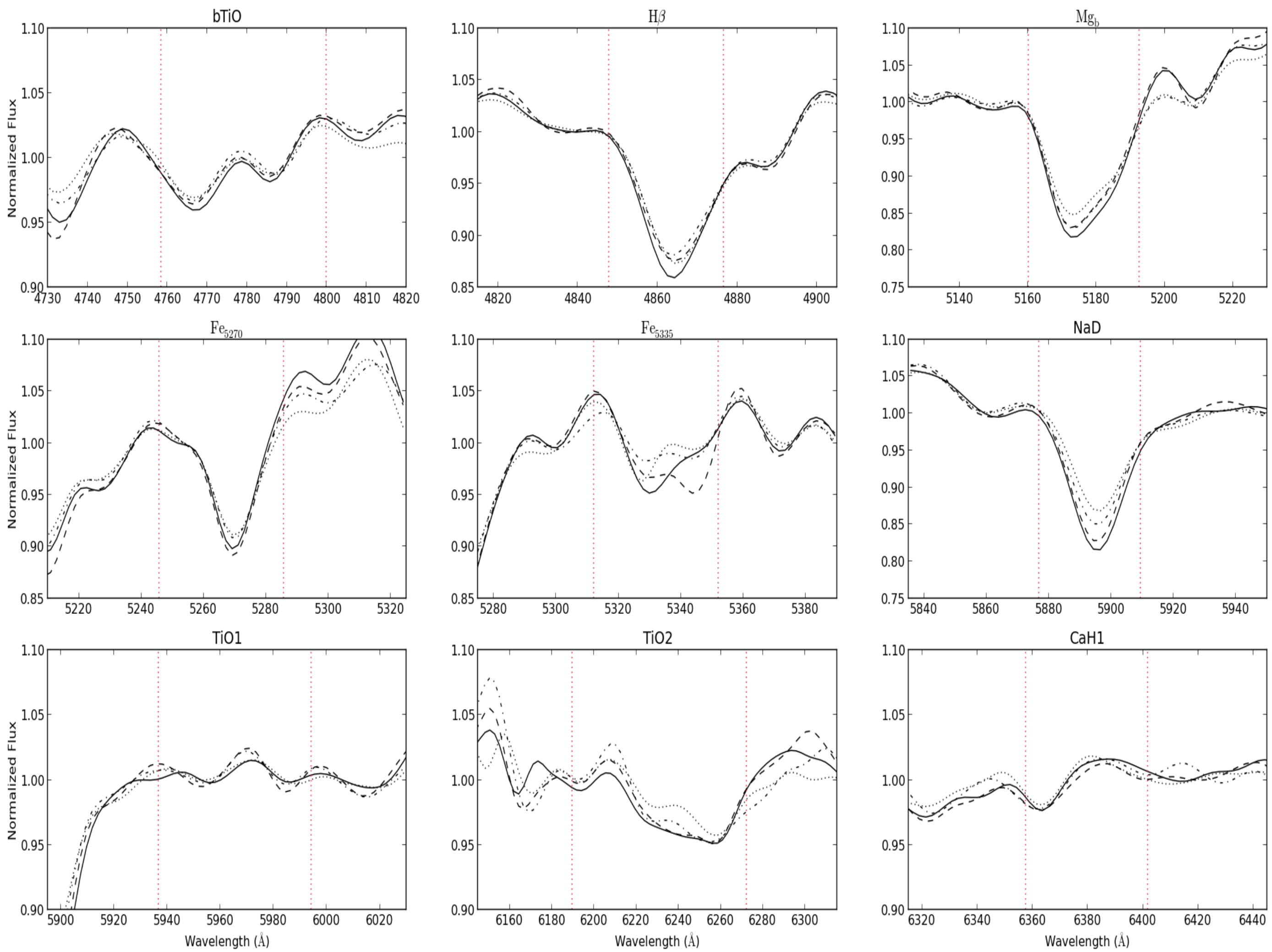

Figure B.XIV: UGC05771

	bTiO	Hβ	Mg$_b$	Fe$_{5270}$	Fe$_{5335}$	NaD	TiO1	TiO2	CaH1
R$_{eff}$/8	1.4431e-02	2.1462e+00	4.0111e+00	2.5469e+00	1.8108e+00	3.6753e+00	3.9457e-02	7.5815e-02	-8.5522e-03
R$_{eff}$/4	9.3513e-03	1.9027e+00	3.6732e+00	2.6418e+00	2.2084e+00	3.4713e+00	3.8415e-02	7.1714e-02	-5.8195e-03
R$_{eff}$/2	4.9649e-03	1.8340e+00	3.4813e+00	2.2807e+00	1.2246e+00	3.0405e+00	3.9718e-02	7.1538e-02	-8.8167e-03
R$_{eff}$	6.7693e-03	1.9086e+00	3.1135e+00	2.1861e+00	1.4757e+00	2.6398e+00	2.7960e-02	6.0828e-02	-4.8513e-03

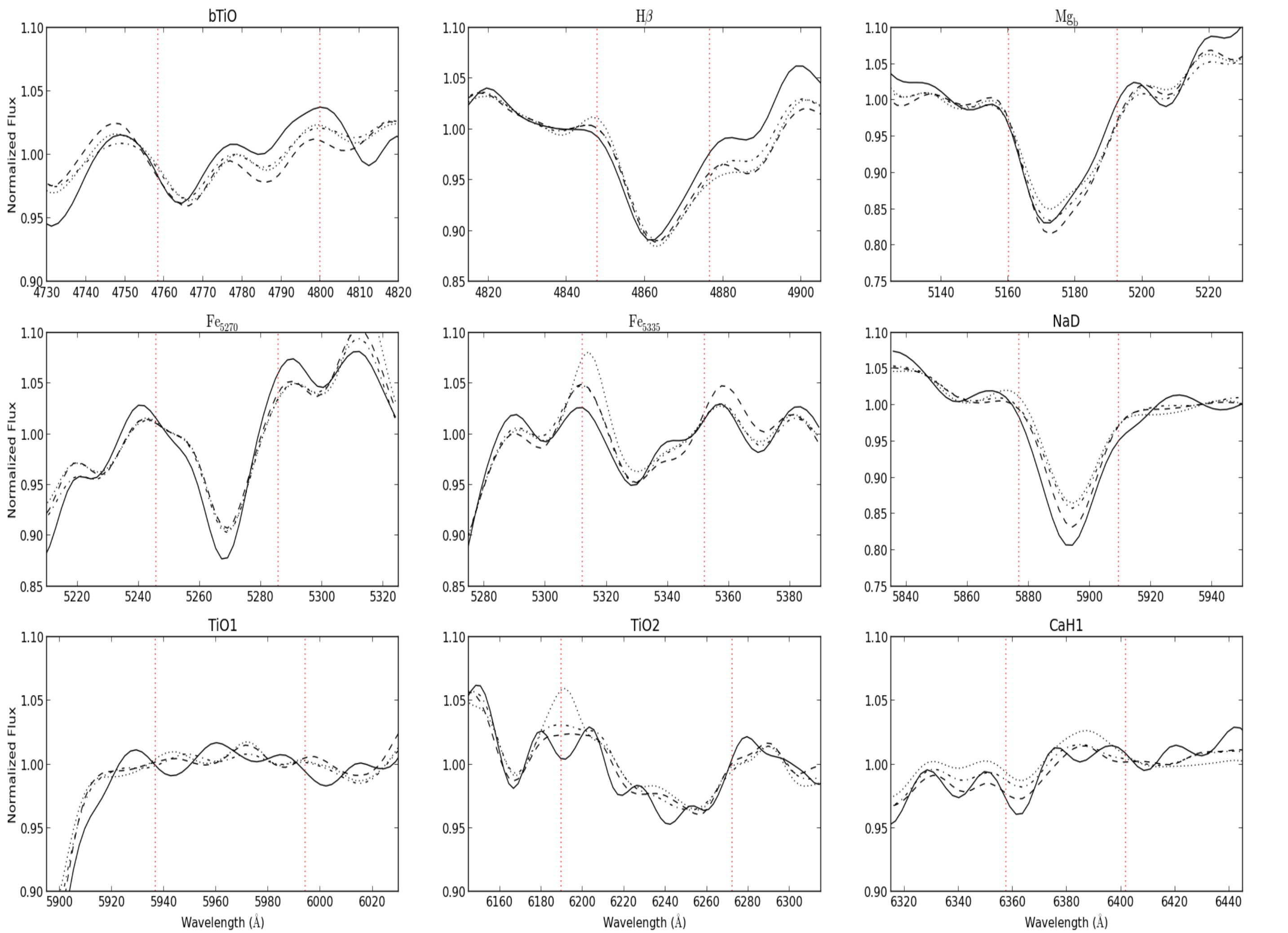

Figure B.XV: UGC10693

	bTiO	$H\beta$	Mg_b	Fe_{5270}	Fe_{5335}	NaD	TiO1	TiO2	CaH1
$R_{eff}/8$	*-9.7305e-03*	1.8915e+00	3.1471e+00	2.7936e+00	1.1904e+00	4.0467e+00	3.7429e-02	7.8237e-02	-6.1750e-03
$R_{eff}/4$	1.8715e-02	1.5339e+00	3.8708e+00	2.3030e+00	2.0098e+00	3.1605e+00	3.4949e-02	6.8604e-02	-8.7433e-03
$R_{eff}/2$	5.0655e-03	1.7001e+00	3.3965e+00	2.3702e+00	1.6066e+00	2.8389e+00	2.8325e-02	7.1946e-02	-8.0973e-03
R_{eff}	1.1208e-02	1.6182e+00	3.2752e+00	2.5198e+00	1.6932e+00	2.7674e+00	2.9483e-02	7.4156e-02	-1.3758e-02

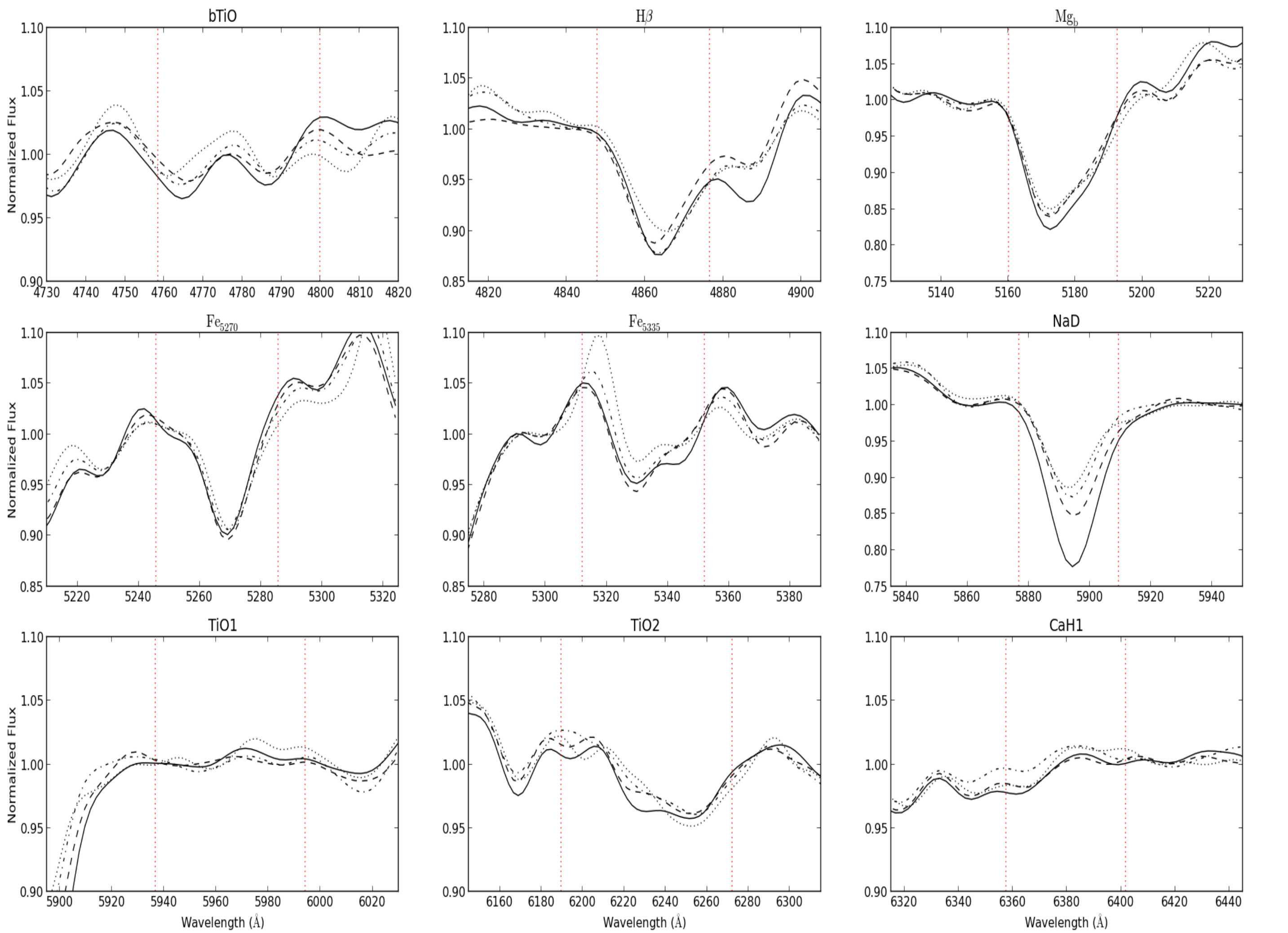

Figure B.XVI: UGC10695

	bTiO	Hβ	Mg$_b$	Fe$_{5270}$	Fe$_{5335}$	NaD	TiO1	TiO2	CaH1
R$_{eff}$/8	1.4309e-02	1.3808e+00	3.7333e+00	2.6100e+00	2.1181e+00	4.2526e+00	3.2852e-02	7.0061e-02	-8.5032e-03
R$_{eff}$/4	1.1639e-02	1.6390e+00	3.0823e+00	2.6571e+00	1.8816e+00	3.0015e+00	2.8073e-02	6.7878e-02	-6.4504e-03
R$_{eff}$/2	6.5582e-03	1.8304e+00	3.1634e+00	2.4137e+00	1.6393e+00	2.3426e+00	3.4019e-02	6.6860e-02	-1.0192e-02
R$_{eff}$	1.3605e-02	1.5757e+00	3.2338e+00	2.3744e+00	1.0912e+00	2.2850e+00	*2.2712e-02*	7.8089e-02	*-1.5739e-02*

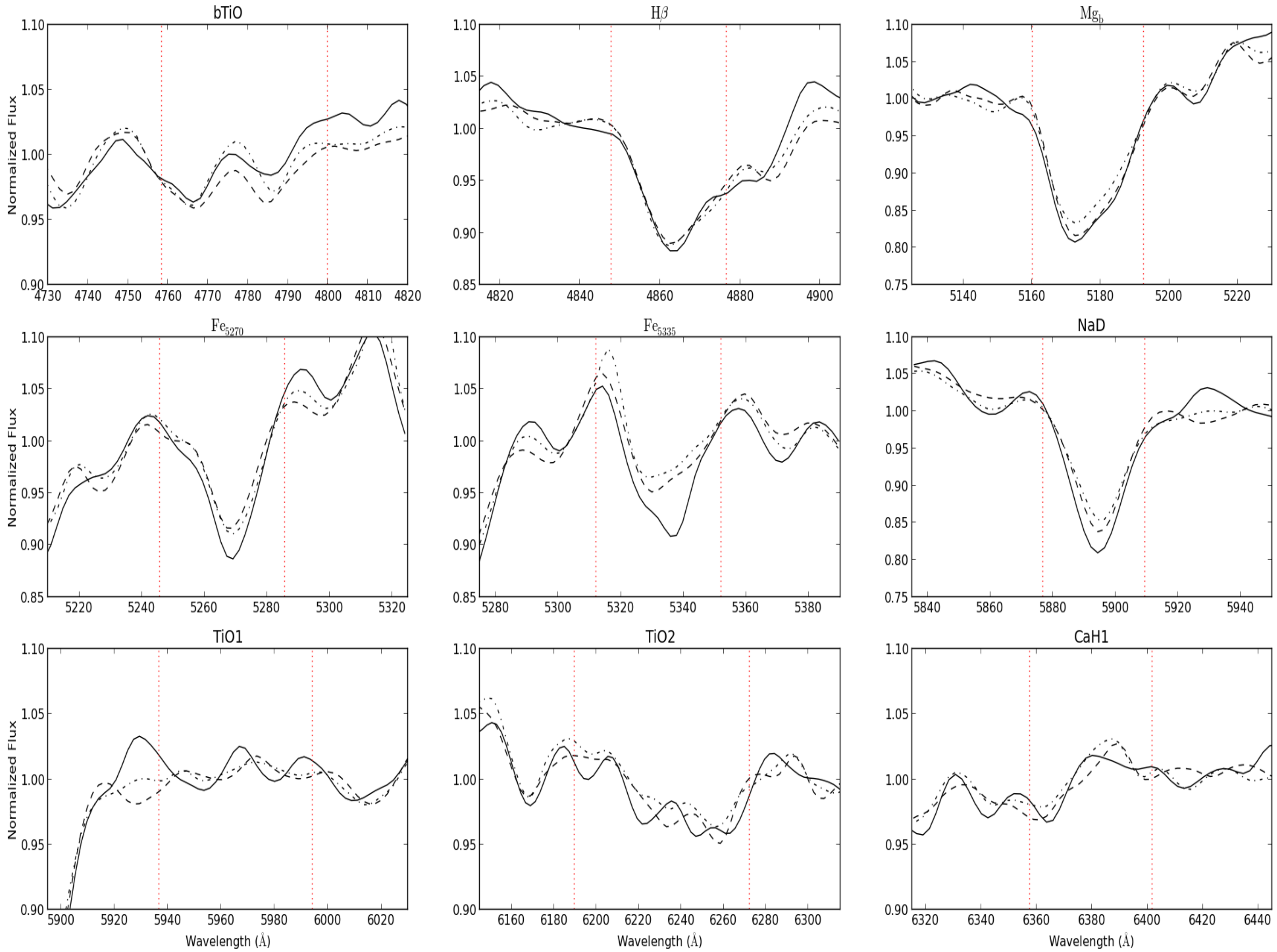

Figure B.XVII: UGC12127

	bTiO	Hβ	Mg$_b$	Fe$_{5270}$	Fe$_{5335}$	NaD	TiO1	TiO2	CaH1
R$_{eff}$/8	4.3754e-03	1.7658e+00	3.9307e+00	2.8455e+00	*2.3924e+00*	3.9377e+00	3.8955e-02	7.7043e-02	-1.1001e-02
R$_{eff}$/4	2.5725e-02	1.5749e+00	3.9067e+00	2.1139e+00	2.1007e+00	3.0460e+00	3.5934e-02	7.3824e-02	-1.4044e-02
R$_{eff}$/2	1.4772e-02	1.7597e+00	3.5443e+00	2.5255e+00	1.7637e+00	2.9039e+00	2.8242e-02	7.4897e-02	*-1.9078e-02*